Title
Single-cell quantification of dynamic cytoskeletal proteins with microscale electrophoretic separations

Author
Hansen, Louise Lyth

Publication Date
2022

Peer reviewed|Thesis/dissertation

SINGLE-CELL QUANTIFICATION OF DYNAMIC CYTOSKELETAL PROTEINS WITH MICROSCALE ELECTROPHORETIC SEPARATIONS

by

Louise Lyth Hansen

A dissertation submitted in partial satisfaction of the

requirements for the degree of

Joint Doctor of Philosophy
With the University of California, San Francisco

In

Bioengineering

In the

Graduate Division

of the

University of California, Berkeley

Committee in charge:

Professor Amy E. Herr, Chair
Professor Sanjay Kumar
Professor Tejal Desai

Fall 2022

SINGLE-CELL QUANTIFICATION OF DYNAMIC CYTOSKELETAL PROTEINS WITH MICROSCALE ELECTROPHORETIC SEPARATIONS

By

Louise L Hansen

Abstract

SINGLE-CELL QUANTIFICATION OF DYNAMIC CYTOSKELETAL PROTEINS WITH MICROSCALE ELECTROPHORETIC SEPARATIONS

By

Louise Lyth Hansen

Joint Doctor of Philosophy in Bioengineering

with University of California, San Francisco
University of California, Berkeley

Dissertation Chair:
Professor Amy E. Herr

Biological processes are often dynamic. On a macro-level, the transformation of a biological system from one state to another drive cell differentiation, migration, and basic functions. On a micro-level, the active arrangement of biological material is necessary for the generation of cellular machinery, critical signaling and binding events, and proteomic production. Across all levels, disruptions in these dynamic response processes underpin disease states and drug resistance. Advances in single-cell protein measurement tools are necessary to define functional heterogeneity in varying cell types, elucidate complex biological processes, and uncover new molecular targets for treatments and therapies

This doctoral research reports on the design and development of new bioanalytical techniques for the targeted interrogation of dynamic biological processes with single-cell resolution. On the micro-scale, we measure the dynamic arrangement of protein complexes in the cytoskeleton. On the macro-scale, we couple mechanical stimulus with multiplexed proteomic evaluation on a single-cell level. Both microfluidic platforms leverage protein electrophoresis to increase the molecular specificity of the measurement and report on structural and cytoskeletal proteins.

First, “Single-cell protein Interaction Fractionation Through Electrophoresis and immunoassay Readout” (SIFTER) combines differential detergent fractionation, bi-directional electrophoresis, and immunoassay steps into an arrayed microdevice for the simultaneous detection of multimeric cytoskeletal protein complexes and their respective monomers in 100s of individual cells. To improve upon the molecular specificity of antibody-based detection, we physically fractionate protein complexes and monomers by size-exclusion electrophoresis in a polyacrylamide gel. During fractionation, the depolymerization of complexes is minimized by stabilizing lysis buffer, delivered by gel lid fluidics. We apply SIFTER to evaluate the distribution of monomers and

complexes within a heterogeneous population of cells, and the change in distribution of cytoskeletal complexes upon cellular stimuli. Co-detection of actin filaments, microtubules, and intermediate filaments expands SIFTER to global cytoskeletal evaluation.

Next, to clarify the link between extracellular stiffness and resultant proteomic state of a cell, we report on ECM-PAGE, an assay that combines the molecular specificity of single-cell polyacrylamide gel electrophoresis (PAGE) with a tunable substrate for extracellular matrix (ECM) recapitulation. Two distinct functional layers permit optimization of the ECM layer without affecting the analytical layer, and vice versa. The ECM layer, made up of PDMS, is compatible with existing material formulations to generate material stiffnesses across several orders of magnitude and for stamp-off microcontact patterning of ECM proteins onto the surface. By using PAGE for size-based protein separation and immobilization, we report on the quantitative protein abundance of 8 proteins, ranging from actin (42 kDa) to Vinculin (117 kDa) within a 1 mm separation lane. Informed by separation resolution, we design antibody combinations (Actin/actinin and vimentin/paxillin) for the quantification of four proteins with only two fluorescent reporter molecules. Further optimization of the ECM-PAGE system is necessary to evaluate protein expression for a greater sample number, as a fluid layer between the two components causes cross-contamination between single-cell reservoirs with greater array occupancy. We anticipate that with further system characterization, the ECM-PAGE system could report on single-cell multidimensional data (stiffness, cell morphology, and proteomic expression) and elucidate the heterogeneous single-cell responses that drive cancerous tumor behavior.

Given the molecular specificity necessary to report on protein complexes, we investigated means mitigation injection dispersion to improve separation performance. Furthermore, the miniaturization of these technologies to achieve high-throughput, single-cell quantification requires advancements in device materials and geometries. We consider the generation of large-surface polyacrylamide-polymer devices as a direction for new microscale device geometries.

By leveraging microscale technologies, these new measurement methods can report on context-dependent processes with single-cell resolution.

to my family.

til min familie.

Table of Contents

List of Figures

Chapter 1: Introduction

Chapter 2: Measuring expression heterogeneity of single-cell cytoskeletal protein complexes

Appendices

List of Tables

Acknowledgements

The work presented in this dissertation would not have been possible without the wealth of support I received during my PhD studies. I feel incredibly privileged to have had abundant administrative, technical, financial, and emotional support,

First and foremost, I would like to thank my PhD advisor, Prof. Amy Herr. It has been a privilege to work with Amy during my PhD. I am thankful for her tireless work to ensure that her lab has an abundance of financial resources, academic connections, and intellectual opportunities. During my time in her lab, I had many great opportunities that have exceeded my pre-graduate expectations. From presenting at a conference in Hong Kong to completing an industry internship, Amy has encouraged excellence and enabled learning opportunities both in- and out-side of lab. Her commitment to our field, research excellence, and the lab is unrivaled. Whenever I felt as if I was running at 100% and had little more to give, I often found solace in knowing that Amy was working 150% behind the scenes to make it all possible.

Amy fosters a supportive and intellectual research group. I want to thank past and present members of the Herr Lab for being fantastic lab mates, colleagues, and friends. I have appreciated the time that my colleagues have dedicated to attending practice talks, asking thoughtful questions, and providing feedback. Specifically, I want to acknowledge Dr. Julea Vlassakis for "actin' up" with me during our collaborative project. Outside the Herr lab, the work included here has benefitted tremendously from interactions with brilliant people across the UC campus, including Paul Lum (BNC), Mary West (CTAF), and Dr. Ryo Higuchi-Sanabria (formerly Dillin group, MCB).

I would also like to thank previous mentors including Prof. Paul Yager (University of Washington, Seattle) and Dr. Beverly Torok-Storb (Fred Hutchinson Cancer Research Center, Seattle). Without their encouragement, my academic path would likely not have included graduate school. In addition, I would like to thank the members of my dissertation committee: Prof. Sanjay Kumar and Prof. Tejal Desai. Both have provided invaluable research feedback and career guidance. I am thankful for my extended circle of mentors that have contributed to this work in a range of ways. I am grateful for the helpful guidance and feedback on my research from my qualifying exam committee members: Prof. Dorian Liepmann, Prof. Sophie Dumont, Prof. Aaron Streets and Prof. Eva Nogales.

The research presented within this dissertation was furthermore made possible by administrative and funding support. I would like to thank Mike Bentley and the rest of the Stanley Hall Shipping and Receiving Department. Also, thanks go out to Kris and the rest of the QB3 office. Lastly, funding sources include the Bioengineering Lloyd fellowship, NIH, and Chan Zuckerberg Biohub.

Cheers to the friends I made along the way! Thank you to Kristine Tan for the company during late nights in lab and for tasteful treats. To Gabi Lomeli for the trips to the beach and our other adventures. Gabi has often had the tough job of reminding me to maintain a "water off a duck's back" attitude, when I have been inclined to take a more cormorant-style approach by "keep diving until your wings are waterlogged and you need to dry on the beach". Thank you for being

the best lab partner I could have asked for during my PhD. To Jessie Liu, for the cross-bay solidarity as we navigated graduate school. I feel incredibly fortunate to have had such an elite group of people in my life during this time. The last couple of years of graduate school would not have been the same without the phenomenal crew in the house on Walnut Street. To Alison, Miranda, Ana, and Molly: Thank you for the kitchen laughs, TV nights, good gossip, and endless emotional support. To Cat, for continuing to be one of the best cheerleaders I have had.

Lastly, none of this would have been possible without my family. My parents continue to be my greatest sources of inspiration and strength. I have lived an incredibly fortunate life, made possible because of their hard work. Thank you for being here for me on the days where I struggled, and on the days where I celebrated. I want to acknowledge my two grandmothers, Elva and Aase Marie. I treasured our chats and catch-ups on my walking commute to lab. They remind me that the Lyth&Hansen family is resilient. Finally, I can only start to describe my gratitude to my sister, Ida Marie. Her generosity, loyalty, and fierceness continue to inspire me. I am certain that I would not have made it through graduate school without her support, wise words, silly memes, and long phone calls. Ida taught me that we must be silly every day, or our brains will grow mold.

Chapter 1: Introduction

Summaries of existing single-cell proteomic techniques are reproduced with permissions from:

Hansen, L.L., Lomeli, G., Vlassakis, J., Herr, A.E. (2022). Single-Cell Resolution Immunoblotting. In: Sweedler, J.V., Eberwine, J., Fraser, S.E. (eds) Single Cell 'Omics of Neuronal Cells. Neuromethods, vol 184. Humana, New York, NY. https://doi.org/10.1007/978-1-0716-2525-5_7.

1.1: The importance of single-cell, proteomic analysis

For both inter- and intra-cellular communication, proteins act as dynamic functional components and signaling molecules. The expression level and state (e.g. unmodified, modified, or interacting, etc.) of protein species are the fundamental underpinnings of cellular phenotype and function. Thus, irregular protein function and concentrations often underpin disease states. While the central dogma suggests we can predict protein expression form RNA or DNA levels, recent work has shown poor correlation between some gene products and protein expression the single-cell level [1]–[4]. The discrepancy between mRNA expression and protein abundance is partially attributable to variable protein translation and degradation rates [5]. In addition, by evaluating the state of a cell at a point in the central dogma upstream of the proteome, genomic and transcriptomic measurements lack information on proteoforms. Proteoforms are variable versions of a protein that arise from alternative splicing or post-translational modification (**Figure 1.1**). Proteoforms have distinct biological function and relevance while being highly similar in their structure. The high complexity and diversity within the protein population adds to the complexity of measuring proteins directly, and correlating DNA or RNA to protein abundance, as a variety of proteoforms can arise from a limited number of genes [6], [7]. For example, only 12% of the proteins in human cells is directly encoded by the genome [8].

Direct measurement of protein target levels is essential to understand the role of specific biomolecules in cell biology as well as the protein expression changes that drive behavior in healthy and aberrant cells. Heterogeneity is inherent in cellular processes. To evaluate important biological phenomena such as aging, cancer development, and metastasis, proteomic measurement must be made at the single-cell level. Cellular heterogeneity within a collection of cells drives drug resistance and paves the way for metastatic colonies [9]–[12] . For example, cancerous subpopulations of cells must undergo endothelial-to-mesenchymal transition to gain cancerous cellular behavior such as metastatic potential. Single-cell resolution permits the quantification and characterization of such heterogeneous sample pools and provide proteomic insight into the molecular machines that drive the gain-of-function transition [13]. In comparison, bulk measurements mask cell-to-cell variability as they analyze cellular responses as blended average parameters. Deeper understanding of the composition and dynamics of the proteome at the single-cell level will further our understanding of the inner workings of cells.

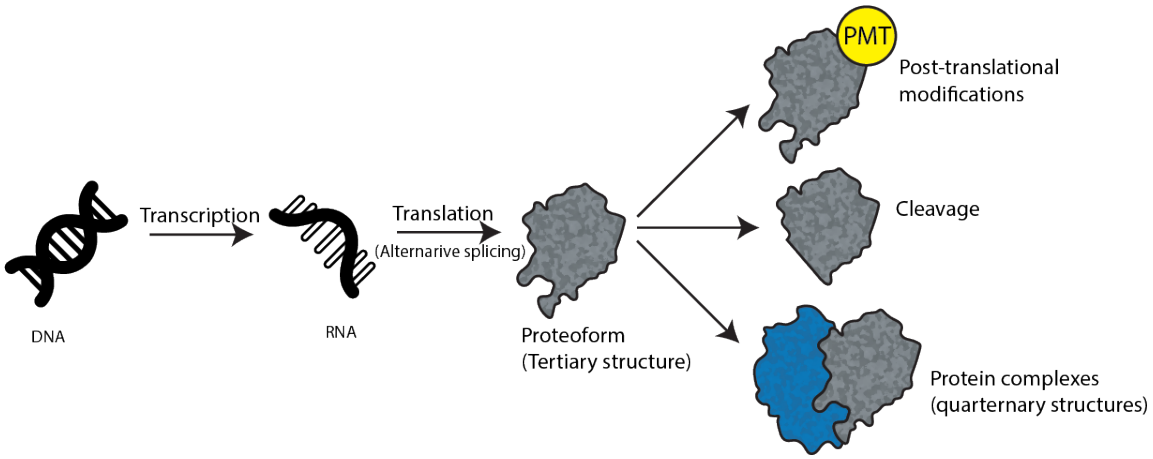

Figure 1.1 – The central dogma and generation of protein isoforms. DNA is converted into transitory mRNA molecules during transcription. Translation converts RNA to proteins. During translation, alternative splicing might generate different versions of proteins from the same RNA source. After translation, proteins are further subject to chemical modifications such as post-translational modifications, cleavage events, and the formation of protein complexes and machinery. Protein tertiary structure refers to the folded configuration of a protein subunit in three-dimensional space. Quaternary structure refers to the relationship and formation of complexes between different protein subunits.

1.2: Highly specific, highly sensitive measurements of protein

Precision tools designed to selectively measure protein abundance, form, and state in single cells are needed. Technology for the quantification of protein from must be: 1) Highly sensitive for single-cell sample detection, and 2) Highly specific for detection of the proteoforms. Highly specific measurements permit the quantification of not just important proteins, but their respective proteoforms or quaternary structure. Protein cytometry tools are designed to detect specific proteoforms in each individual cell, with sufficient throughput to capture intrapopulation variation. For a given protein species, these tools then report on differences in chemical modification, molecular mass, interactions, conformation, and a myriad of other physicochemical parameters among the population of expressed members of that species.

Currently, single-cell proteomic platforms are primarily based on mass spectrometry and immunoassays, such as immunofluorescence, proximity ligation assays (PLA), immunocytochemistry (ICC), and mass and flow cytometry.

Mass spectrometry measures the mass-to-charge ratio of ionized components, and is the result of steps including sample handling, ionization, mass analysis and ion detection. With bottom-up mass spectrometry, proteins in a complex mixture are digested into small peptide fragments prior to detection by mass spectrometry. Bottom-up mass spectrometry identifies thousands of different proteins and post-translational modifications in a single sample. However, the protein-to-peptide digestion makes it difficult to map back modifications to the intact proteins and

predict the molecular stoichiometry for a quantifiable assessment of isoform abundance [14], [15]. Alternatively, top-down mass spectrometry analyzes intact proteins to detect proteoform expression levels (thus reporting molecular stoichiometry). Yet, top-down mass spectrometry offers detection sensitivity and throughput insufficient for single-cell analyses [16]–[18].

Immunoassays are the *de facto* standard for measuring protein targets at the single-cell level. Immunoassays detect a-priori identified targets by using an antibody probe designed to recognize and bind to the target epitope. After probing with fluorescently labeled immunoaffinity reagents (antibody probes), cells are evaluated by a fluorescence-readout technique such as microscopy. ICC maintains single-cell information and can assess cell-to-cell heterogeneity. However, the use of antibody probes predisposes ICC to cross-reactivity effects, high background, and limited multiplexing capabilities [19]–[21]. Flow cytometry improves upon the throughput of ICC, with the tradeoff of requiring large number of cells for analysis. While powerful, the selectivity of immunoassays is fundamentally limited by the availability and specificity of antibody probes, as well as by fixation artifacts [22]. In considering the vast constellation of proteoforms known to exist, the development and application of an antibody probe specific to each proteoform serves as a major limiting factor.

To enhance the specificity of immunoassays, a first stage – typically an electrophoretic separation – is prepended to a second-stage immunoassay. This type of two-stage assay is called an immunoblot. Instead of simply reporting reactivity of protein target with antibody probes (as in an immunoassay), the immunoblot reports two characteristics: the physicochemical characteristic measured by the separation and the reactivity. The capacity to report not one, but two characteristics of each protein target increases assay specificity. A widely used type of immunoblot, known as a western blot, concatenates protein sizing using electrophoresis with immunoprobing. The size-based separation physically resolves proteins of different sizes, then reports reactivity with antibody probes, even when using a pan-specific antibody probe. In this case, the molecular specificity of the antibody is combined with separation science to yield a high-fidelity measurement. While the bulk western blot technique is one of the most widely used analytical tools, the single-cell western blot (scWB) miniaturizes the workflow for single-cell analysis.

Microfluidic assays like the scWB precisely control mass and fluid handling for efficient, reproducible, and timely analysis of biological targets, all while maintaining high local analyte concentrations. For electrophoresis, miniaturization enhances performance. scWB-based modalities eliminate the need to pool cells to achieve detectable protein concentration, allowing single-cell resolution for the detection of intrapopulation protein expression variations. Cell handling losses and target dilution are mitigated by microfluidic features designed to match the reaction volume of an intact cell to maintain intracellular concentration levels even after cell lysis [29]. Minimizing cell lysis and electrophoresis times decreases the dilutive effects of diffusion, facilitating the detection of low-abundance molecules from single cells. The scWB method is suitable for analysis of proteins in the 15 to 90 kDa range within an 8%T gel, and has an estimated limit of detection at 27,000 molecules using purified EGFP (equivalent to 45 zmol),

both features that make the device appropriate for detecting a range of protein targets [1], [23], [24].

1.3: Electrophoretic cytometry at the microscale

Polyacrylamide gel electrophoresis

Electrophoresis is the migration of charged particles in an applied electric field. Proteins generally have a negative protein charge due to the relatively basic pKa of most amino acids. In free solution, particles migrate with a velocity (U_{EP}) proportional to their zeta potential:

$$U_{EP} = \mu_{EP} * \bar{E} \quad \text{Eq. 1}$$

Where μ_{EP} is the electrophoretic mobility of the species in a unidirectional and uniform electric field E. A linear relationship exists between electrophoretic mobility and field strength.

The analysis of proteins or nucleic acid within a sieving matrix is a conventional lab approach to identification and quantification of specific biomolecular targets. Polyacrylamide gel electrophoresis (PAGE) is a separation technique where biomolecules are sieved within a porous polyacrylamide hydrogel matrix during electrophoresis. In PAGE, species with different electrophoretic mobilities are separated spatially within the polyacrylamide matrix [25], [26].

During electrophoresis, directional migration of a molecule is the product of the balance of the Stokes drag (F_{drag}) and the total electrical force (F_{EP}). The drag force and electric force are summarized by Eq. 2 and 3, respectively:

$$F_{drag} = 6\pi\eta r\, \vec{U} \quad \text{Eq. 2}$$

$$F_{EP} = q * \vec{E} \quad \text{Eq. 3}$$

Where η is the fluid kinematic viscosity of the separation medium, r is the hydrodynamic radius of the particle, U_{EP} is the particle migration velocity in relation to the medium, and q is the net charge of the particle. Equating the Stokes drag to the electrical force, the velocity of the particle within an electric field can be described as:

$$U_{EP} = \frac{qE}{6\pi\eta r} \quad \text{Eq. 4}$$

From there, we obtain electrophoretic mobility (μ_{EP}) as:

$$\mu_{EP} = \frac{q}{6\pi\eta r} \quad \text{Eq. 5}$$

Thus, electrophoretic mobility is proportional to the particle net charge and is inversely proportional to the particle size. In PAGE, proteins or other particles migrate within the sieving

matrix based on molecular weight and charge, with small and largely charged moving achieving a greater velocity than those of large and uncharged particles.

By electrophoresing proteins through a high viscosity sieving matrix such as polyacrylamide, electroosmotic flow is suppressed, and particle mobility is decreased. For polyacrylamide, the viscosity of the material is related to the pore size of the polymer network, making it well suited for resolving protein targets that often have matching characteristic dimension. Polyacrylamide is polymerized through free-radical reaction of acrylamide monomer and crosslinker, such that the pore size is directly proportional to the concentration of the monomers [27], [28]. In a gel, the Ferguson relationship describes the empirical correlation between protein size and migration velocity within a sieving matrix [29]:

$$\log(\mu_{EP,gel}) = \log(\mu_{EP}) - K_r * T \quad \text{Eq. 6}$$

Where $\mu_{EP,gel}$ is the electrophoretic mobility of the particle through the gel, μ_{EP} is the electrophoretic mobility in free solution, K_R is the empirically-determined retardation coefficient and T is the percent (w/v) of the total polyacrylamide monomer in solution (bis and acrylamide). For proteins, PAGE is often completed in one of two conditions: Native or denaturing. In the former, proteins are kept in the tertiary and quaternary state, if possible [30], [31]. In this case, electromigration is proportional to the zeta potential ($\mu_{EP,fs}$) and the retardation coefficient [32], [33]. In the latter, proteins are denatured and coated with sodium dodecyl sulfate (SDS), an anionic detergent [34]. SDS-PAGE, also known as the western blot, confers a constant mass-to-charge ratio due to the coating of the SDS. This results in the separation of proteins based on their size alone, as retardation coefficient scales with protein molecular weight [35], [36].

Separation performance

In electrophoretic assays, the sample is injected and then separated into individual analytes as the porous matrix differentially impedes protein electromigration based on analyte size or other particle parameters. Assuming we start with a sample plug, a protein separation results in the formation of separated product that appears as a series of protein bands within the sieving matrix (**Figure 1.2**). In SDS-PAGE, the distance of each analyte band from the injection site correlates to the size of that analyte (i.e., protein). The analyte concentration distribution in the axial direction during separation is the result of spontaneous diffusion causing the dispersion of analyte over time. Dispersive mass transport causes protein bands to assume a Gaussian distribution during electrophoresis [37], [38]. The corresponding equation for diffusion from a point source in one dimension is:

$$c(x,t) = \frac{c_0}{\sqrt{4\pi D_t}} \exp(-\frac{x^2}{4Dt}) \quad \text{Eq. 7}$$

Here, the concentration distribution is expressed in terms of the diffusivity coefficient (D), the initial concentration of the analyte (C_0) and the axial location (x) and time (t). The variance off

the Gaussian profile can be expressed as $\sigma^2 = 2Dt$ .The integral of the Gaussian curve produced by the analyte equates the total analyte concentration, such that the total protein abundance can be calculated by summing over $\mu \pm 2\sigma$, where σ is the standard deviation of the curve and $\pm 2\sigma$ correlates to the 95.45% coverage of the signal (confidence interval). The Stokes-Einstein equation allows the estimation of diffusion coefficient based on the Boltzmann constant (k), the temperature (T), viscosity (η), and the radius of the particle (r):

$$D = \frac{kT}{6\pi r\eta} \qquad \text{Eq. 8}$$

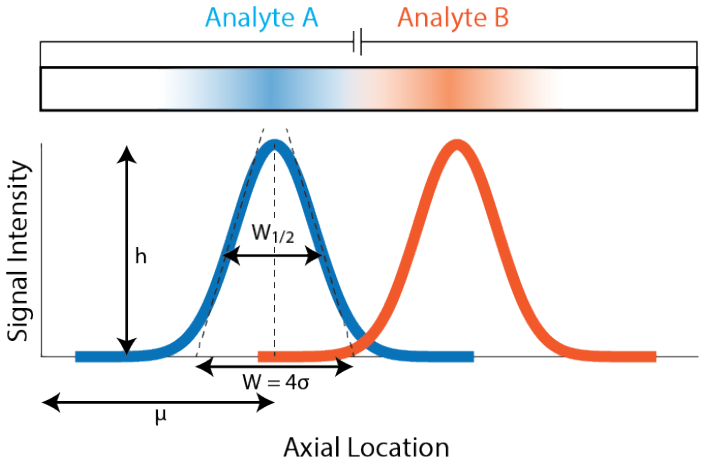

Figure 1.2: Graphical representation of analyte concentration distribution within a separation matrix. Here, two analytes are detected (analyte A, blue; analyte B, orange). Each analyte appears as a Gaussian distribution in the axial direction along the separation axis. In SDS-PAGE, the distance from the injection point (μ) directly correlates to analyte size. Here, analyte A has a larger molecular mass than analyte B. The width of the peaks (w = 2.35σ) and height can be described according to standard Gaussian specifications. The separation resolution refers to the amount of overlap between the two peaks. An assay with great separation resolution will have minimal overlap between the two peaks.

The efficiency of a molecular separation within a sieving matrix is an important design criterion for electrophoretic cytometry measurements. Key analytical metrics include peak width and peak intensity. If more than one species is separated and detected, separation resolution is crucial for assessing the clarity of each protein peak. The latter is a unitless metric that can be used to compare across devices and platforms. separation resolution describes the overlap of the two Gaussian profiles. To calculate separation resolution (R_s), the difference in migration distance is divided by the average peak width of the two analytes:

$$R_s = \frac{\Delta X_{1,2}}{2\sigma_1 + 2\sigma_2} = \frac{(\mu_1 - \mu_2)Et}{4\sqrt{2D_t + \sigma^2}} \quad \text{Eq. 9}$$

Where μ_1 and μ_2 are the peak locations from the injection point for the two analytes, also known as the differential mobility, and σ is the mean width of the analyte peaks. D is the diffusion constant, and E is the electric field. Thus, the efficiency of a separation is directly proportional to the width of the analyte concentration distribution. The width of the Gaussian is impacted by diffusion, injection, and joule heating, all contributing to 'band-broadening' [39], [40]. From this equation, strategies for improving separation performance are derived. Increasing the separation time increases the separation resolution. Conversely, as the widths of the protein bands increase (because of diffusion or injection dispersion), separation resolution decreases. When Rs = 1.5, there is no overlap between the two analytes. Commonly, Rs = 1 (98% resolved) is sufficient for deconvolution of signal.

The maximum number of analytes that can be resolved in a separation is quantified by the peak capacity (n_c) [38]:

$$n_c = \frac{L}{\sigma} \quad \text{Eq. 10}$$

Where L is the separation axis length and σ the average peak width. A longer separation axis and/or narrower analyte bands permits the detection and deconvolution of a greater number of analytes. The width of the analyte band is the result of band broadening (σ^2) factors such as molecular diffusion, sample injection, joule heating and surface adsorption [41].

Sample preparation for electrophoresis

When working with complex analyte samples from cellular origins, proper sample preparation is necessary for predictable sample injection. Prior to electrophoresis, proteins must be extracted from the biological sample, freed of contaminants or interfering substances, and kept in solution during the separation process [42]. In short, proteins must be solubilized for electrophoretic separations to occur. The solubilization process involves the breaking of interactions between the substances to be analyzed and interfering substances, and requirements vary greatly from sample to sample, and from electrophoretic technique to technique [43]–[46]. Difficulty extracting proteins for single-cell analysis techniques arise due to the presence of the plasma membrane. Besides disulfide bonds, noncovalent interactions (hydrogen bonding, Van der Waals forces, and electrostatic interactions) keep macromolecules together and proteins folded. Detergents (synonym with surfactants, derived from surface-active agent) create a stable dispersion of hydrophobic components, such as lipids, in the aqueous medium due to the formation of micelles. In solution, detergent molecules form micelles with the hydrophobic tails aligning to the center and the hydrophilic headgroups interfacing with the solution. The critical micelle concentration (CMC) refers to the minimum concentration at which micelles form [47], [48].

While most (if not all) samples must be solubilized for analysis, proteins can be either in their native or denatured state. For example, the sample preparation of cellular lysate for size-based separation by SDS-PAGE requires both solubilization and denaturation of the sample. In comparison to solubilization, denaturation is the disruption of native, functional protein state by disrupting interactions within a single protein [42], [48]. It is difficult to solubilize membrane proteins without denaturation of those same proteins. Denaturation of proteins can be achieved by a range of means, including heat, change in pH, organic solvents, denaturation via agents such as urea, and detergents.

As mentioned earlier, SDS-PAGE is the mass-based sizing of proteins. In this assay, proteins are linearized by the ionic surfactant SDS, which also confers a uniform mass-to-charge ratio. SDS is hypothesized to bind proteins in a necklace-and-beads fashion. SDS can form hydrophobic interaction between its alkyl tail and amino acids, leading to protein denaturation. Furthermore, the ionic head of SDS drives electrostatic repulsion between micelles is used to denature the protein as they form on different parts of an extended protein [49]–[51]. SDS binds at a known ratio of 1.4 g SDS to 1 g protein independent of amino acid composition [42]. As a result, protein mobility inside the polyacrylamide sieving matrix is dependent on protein size and is independent of native, three-dimensional conformation of the protein. In contrast to solubilization, denaturation involves the linearization and disruption of intra-protein interactions. Chaotropic agents, such as urea, are chemical denaturants that prevent aggregation of proteins as hydrophobic residues are revealed during protein unfolding process. However, these agents are not able to solubilize the lipid bilayer.

Novel bioanalytical assays require the optimization of both detergents and chaotropic agents for the solubilization and, if required, denaturation of the analyte.

Scaling laws in microscale electrophoresis

The advancements of microfluidics and microscale analytical techniques have led to the development of microchip-based electrophoretic separations, such as the scWB. Microscale tools enable high precision measurements of biomolecules that were not previously possible. For example, microchip-based capillary electrophoresis (μCE) [52], the earliest format of microfluidics, has been used to analyze proteins [53]–[56], DNA [57]–[59], antibody-drug conjugates [60], and glycans [61]. In general, microfluidics is the handling and manipulation of fluids at the microscale [62]. Outside of separation techniques, microfluidic systems developed over the past 50 years have permitted the development of organ-on-a-chip [63], diagnostics [64]–[66], analytical devices and single-cell sequencing [67].

At the microscale, some physical phenomena and forces scale more favorably than others [71], [72]. Common scaling laws derived from dimensional analysis for microfluidics are summarized in T**able 1**. These laws have been used to inform device designs presented in this dissertation. Generally, forces and metrics that follow ℓ^2 and higher power dependencies have a greater dependence on length, while characteristics with ℓ^2 and lower power dependencies are less

dependent on length. In microfluidics, phenomena with large power dependencies on length will have a reduced effect at smaller length scales. For example, for a 10-time reduction in scale, diffusion time is reduced by a factor of 10^2 and electric field strength is reduced by a factor of 10^{-1}. Generally, the small geometrical features in microfluidics are less affected by volume-dependent phenomena, and more affected by surface area-dependent phenomena.

Table 1.1: Scaling laws relevant to microfluidics for use of in biological measurements in electrophoretic assays. (Derived after [68]–[70]).

Physical Phenomena	**Units**	**Scaling law (in relation to ℓ)**
Capacitance	F	ℓ^1
Diffusion time	s	ℓ^2
Drag force	N	ℓ^{2+2n} (n is fluid velocity)
Electric field	V/m	ℓ^{-1}
Electrostatic force	N	ℓ^2
Gravitation force	N	ℓ^3
Heat capacity	J/K	ℓ^3
Mass	Kg	ℓ^3
Resistance	Ω	ℓ^{-1}
Surface area	m^2	ℓ^2
Surface area : volume ratio	m^{-1}	ℓ^{-1}
Volume	m^3	ℓ^3
Volumetric flow rate	m^3/s	ℓ^4

Generally, microfluidic separation techniques, such as single-cell PAGE assays, can quantify samples with increased speed, reduced sample consumption (nano- to micro-liter) and higher throughput than conventional bulk assays. Miniaturization of these assays enhances performance by maintaining high local analyte concentration. This eliminates the need to pool samples to achieve detectable protein concentration, permitting single-cell resolution of protein abundance [1], [23], [24].

The separation efficiency of electrophoretic assays is dependent on the voltage applied. While a higher electric field might increase separation resolution, it also induces a higher electric current within the microfluidic device [41]. This produces Joule heating ($Q = \rho E^2$, where ρ is the electric conductivity of the buffer). The generation of Joule heating increases analyte dispersion by increasing diffusivity of the molecules, causing a decrease in separation resolution [73], [74]. In an electrophoretic circuit, the Joule heating can be expanded to:

$$Q = E * V * A * \frac{1}{\gamma} \qquad \text{Eq. 11}$$

Where V is the voltage applied, and A is the cross-sectional area with elementary resistivity of γ. While Joule heating correlates to the electric field applied, small cross-sectional areas of microfluidic devices permit the use of higher electric fields without detrimental Joule heating.

Complementary to Joule heating is heat dissipation. Microfluidic chips benefit from small device thicknesses and high surface-to-volume ratio to promote heat dissipation, as per Eq. 12:

$$P = k * \frac{T - T_w}{L} S \qquad \text{Eq. 12}$$

Where T is the temperature of the microfluidic device, T_w is the atmospheric temperature, K is the thermal conductivity of the device material, L is the distance of heat dissipation (often the thickness of the device) and S is the heat dissipating area (often the top/bottom surface area) [39].

Similarly, higher electric field strengths can be obtained in microscale separations using a low voltage to the short separation axis. High electric field strengths correspond to high separation speed [74]. As a result, species can be resolved in seconds over short distances [75], [76]. Miniaturization of separation axis allows for parallelization to improve throughput of the assay. Some benefits of scaling for biological measurements are speed and power consumption [77]. The former implies that biomolecule interaction frequency increases, and the thermal time constraints decrease. Rapid analysis makes these platforms compatible with biological kinetic rates.

In summary, the miniaturization of separation-based assays enables the interrogation of small sample sizes in a rapid, high-throughput way. This lends itself to implementation of single-cell samples for electrophoresis-based proteomic evaluation. With separation rates comparable to biological kinetic rates, microscale separation assays enable new types of biological measurements that were not previously possible.

1.4: Molecular interactions in biology

Proteins are dynamic biomolecules. While essential for most biological processes, their function extends beyond simple chemical reactions. Proteins localize to specific environments within the cell, undergo directed movements, and assemble into protein complex machinery to execute specific chemical events within a cell [78], [79]. Molecular binding interactions, permitted by the complementary binding sites on two or more molecules, are integral to many biological processes. In addition to being a ubiquitous feature of proteins in their native state, binding interactions are harnessed by proteins for the detection of biomolecules and to trigger biological pathways. They are also often implemented as a biorecognition event in biosensing applications (i.e. immunoassays). There are several types of transient binding interactions that occur in biology. These include the binding of small molecule to receptors in drug development, antibody to antigen in immuno-based bioassays, and protein-protein binding in protein complexes and formation of quaternary protein structure [80].

Binding reactions, whether between two proteins of the same species or two different biomolecules, are characterized by their binding specificity and affinity. Affinity refers to the strength with which two biomolecules interact. Affinity can also be described in terms of ΔG, the change in free energy upon binding [81]. This metric is dependent on epitope availability and the environment of the reaction. Specificity refers to the affinity to other biomolecules in the environment compared to that of the reactions intended binding partner [82], [83].

To describe the fundamental binding kinetics and affinity constants of a bimolecular system, we will pick a bimolecular model system of antibody (A) binding to antigen (B) and forming a complex (AB). This bimolecular interaction can be represented as $A + B \leftrightarrow AB$. The forward rate constant (k_1, units: $M^{-1}s^{-1}$) and the reverse rate constant (k_{-1}, units: s^{-1}) describe association and dissociation, respectively. Assuming the reaction is at equilibrium, k_1 and k_{-1} define the molecular dissociation rate constant as $K_D = \frac{k_{-1}}{k_1} = \frac{[A][B]}{[AB]}$ (units: M). K_D depends on the concentration of all three species in the reaction.

1.5: Dissertation Overview

In this dissertation, we report the development of two microscale platforms and associated technology for highly sensitive and specific protein measurements. The bioanalytical separation techniques leverage the miniaturization of existing separation techniques for the characterization and quantification of various physiochemical properties. We focus on specific protein measurements from single cells, defining specific measurements as those highly sensitive to protein state or dynamic cellular processes.

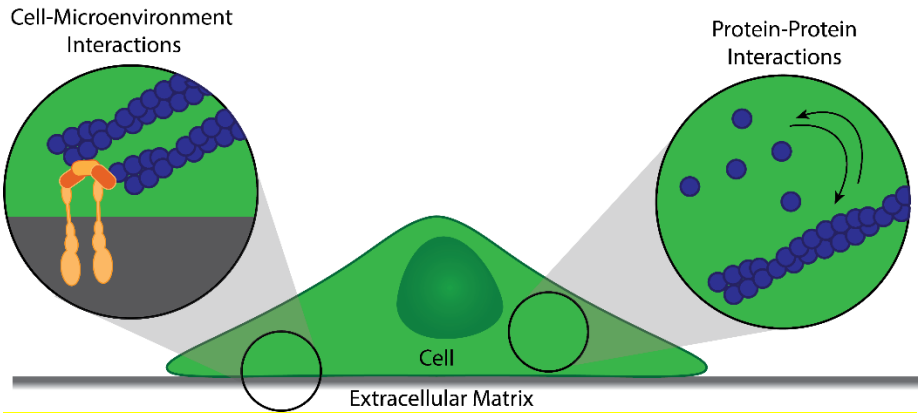

Figure 1.3: Dissertation overview. Techniques introduced in this dissertation are focused on the development and application of microscale separations for the measurements of cell-microenvironment interactions and protein-protein complexes. Both measurements are context-dependent and require not just the quantification of a target analyte, but the state of the analyte or the cell from which the measurement is made.

Specifically, two context-dependent measurements of dynamic relationships are interrogated in this dissertation (**Figure 1.3**):

1) Protein-protein: Differentiation of protein complex from monomers
2) Cell-microenvironment: Measurements with substrate sensitivity as tunable stimulus input

In both cases, the quantification of analyte concentration alone is insufficient for accurate characterization of the dynamic biological processes. We introduce advancements in separation techniques to quantify the presence of biological species in a context-dependent manner. In addition to the protein abundance, these tools report either the state of the analyte or the cell from which the measurement is made. Such measurements expand capabilities to report on the specific quaternary state of the protein analyte or the transient state of a cell in response to external stimulus.

In chapter 2, we present the design and validation of Single-cell protein Interaction Fractionation Through Electrophoresis and immunoassay Readout, or SIFTER. SIFTER addresses the gaps in multimeric protein-complex quantification by combining size-based fractionation in polyacrylamide gel with sequential differential detergent fractionation. We apply this technology for the interrogation of actin filaments, microtubules, and intermediate filaments from single cells perturbed with diverse stimuli, revealing intra-population heterogeneity. SIFTER expands the sensitivity of cytoskeletal measurements by distinguishing quaternary state of proteins, reporting not only on the pure abundance of the analyte, but also on its participation in functional complexes.

In chapter 3, we expand on the previously developed single-cell western blot by coupling it with on-chip culture for the evaluation of cytoskeletal proteins of adhered cells. Cells are cultured on substrates ranging in stiffness, and we link classical morphological features to intracellular protein expression. By coupling on-chip culture of cells with subsequent proteomic evaluation, we can report the proteomic state of single cells in response to external stimulus.

Next, key learnings for optimization and mitigation of injection dispersion are summarized in chapter 4. While a combination of computational and theoretical approaches is used to study the adverse effects of injection dispersion, experimental approaches focus on remedial options compatible with open microfluidic devices. To support the development of novel separation assays of mixed materials, we detail a method for developing large-area PDMS-polyacrylamide structures in chapter 5.

Lastly, in chapter 6, we summarize the work and suggest directions for future work.

1.6: References

[1] J. J. Li, P. J. Bickel, and M. D. Biggin, "System wide analyses have underestimated protein abundances and the importance of transcription in mammals," *PeerJ*, vol. 2, p. e270, 2014.

[2] B. Schwanhüusser *et al.*, "Global quantification of mammalian gene expression control," *Nature*, vol. 473, pp. 337–342, 2011.

[3] J. R. S. Newman *et al.*, "Single-cell proteomic analysis of S. cerevisiae reveals the architecture of biological noise," *Nature*, no. 441, pp. 840–846, 2006.

[4] G. Chen *et al.*, "Discordant protein and mRNA expression in lung adenocarcinomas.," *Molecular & Cellular Proteomics*, vol. 1(4), pp. 304–313, 2002.

[5] R. De Sousa Abreu, L. O. Penalva, E. M. Marcotte, and C. Vogel, "Global signatures of protein and mRNA expression levels," *Mol Biosyst*, no. 5(12), pp. 1512–1526, 2009.

[6] E. Furlanis, L. Traunmüller, G. Fucile, and P. Scheiffele, "Landscape of ribosome-engaged transcript isoforms reveals extensive neuronal-cell-class-specific alternative splicing programs," *Nat Neurosci*, no. 22, pp. 1709–1717, 2019.

[7] B. Raj and B. J. Blencowe, "Alternative Splicing in the Mammalian Nervous System: Recent Insights into Mechanisms and Functional Roles," *Neuron*, vol. 87(1), pp. 14–27, 2015.

[8] R. Aebersold *et al.*, "How many human proteoforms are there?," *Nature Chemical Biology*, vol. 14, no. 3. Nature Publishing Group, pp. 206–214, Feb. 14, 2018. doi: 10.1038/nchembio.2576.

[9] "Cell-to-cell variation and single-cell functional proteomics analysis," 2010. [Online]. Available: http://genomemedicine.com/content/5/8/75

[10] Y. Liu and A. K. Singh, "Microfluidic Platforms for Single-Cell Protein Analysis," *Journal of Laboratory Automation*, vol. 18, no. 6. pp. 446–454, Dec. 2013. doi: 10.1177/2211068213494389.

[11] Y. Zhang, I. Naguro, and A. E. Herr, "In Situ Single-Cell Western Blot on Adherent Cell Culture," *Angewandte Chemie - International Edition*, vol. 58, no. 39, pp. 13929–13934, Sep. 2019, doi: 10.1002/anie.201906920.

[12] W. Yang, H. Yu, Y. Wang, and L. Liu, "Patterned microwell arrays for single-cell analysis and drug screening."

[13] D. di Carlo and L. P. Lee, "Dynamic single-cell analysis for quantitative biology," *Anal Chem*, vol. 78, no. 23, pp. 7918–7925, Dec. 2006, doi: 10.1021/AC069490P/ASSET/AC069490P.FP.PNG_V03.

[14] A. I. Nesvizhskii and R. Aebersold, "Interpretation of Shotgun Proteomic Data," *Molecular & Cellular Proteomics*, vol. 4(10), pp. 1419–1440, 2005, doi: 10.1074/mcp.r500012-mcp200.

[15] A.-C. Gingras, R. Aebersold, and B. Raught, "Advances in protein complex analysis using mass spectrometry," *Journal of Physiology*, vol. 563, pp. 11–21, 2005.

[16] A. J. Link *et al.*, "Direct analysis of protein complexes using mass spectrometry," vol. 17, pp. 676–682, 1999.

[17] A. Lesur and B. Domon, “Advances in high-resolution accurate mass spectrometry application to targeted proteomics,” *Proteomics*, vol. 15(5–6), pp. 880–890, 2015.
[18] J. R. Yates, C. I. Ruse, and A. Nakorchevsky, “Proteomics by mass spectrometry: Approaches, advances, and applications,” *Annu Rev Biomed Eng*, vol. 11, pp. 49–79, 2009.
[19] A. Berod, B. K. Hartman, and J. F. Pujol, “Importance of fixation in immunohistochemistry: Use of formaldehyde solutions at variable pH for the localization of tyrosine hydroxylase,” *Journal of Histochemistry and Cytochemistry*, vol. 29, pp. 844–850, 1981, doi: 10.1177/29.7.6167611.
[20] J. L. A. Voskuil, “Commercial antibodies and their validation,” *F1000Res*, vol. 3, 2014, doi: 10.12688/f1000research.4966.2.
[21] R. Ivell, K. Teerds, and G. E. Hoffman, “Proper application of antibodies for immunohistochemical detection: Antibody crimes and how to prevent them,” *Endocrinology*, vol. 155(3), pp. 676–687, 2014, doi: 10.1210/en.2013-1971.
[22] S. S. Teves, L. An, A. S. Hansen, L. Xie, X. Darzacq, and R. Tjian, “A dynamic mode of mitotic bookmarking by transcription factors,” *Elife*, vol. 5, 2016, doi: 10.7554/eLife.22280.
[23] C.-C. Kang, J.-M. G. Lin, Z. Xu, S. Kumar, and A. E. Herr, “Single-Cell Western Blotting after Whole-Cell Imaging to Assess Cancer Chemotherapeutic Response.,” *Anal Chem*, vol. 86, no. 20, pp. 10429–10436, Oct. 2014.
[24] A. J. Hughes, D. P. Spelke, Z. Xu, C.-C. Kang, D. V Schaffer, and A. E. Herr, “Single-cell western blotting,” *Nat Methods*, vol. 11, no. 7, pp. 455–464, 2014.
[25] A. C. Eldridge and W. J. Wolf, “Polyacrylamide-Gel Electrophoresis of Reduced and Alkylated Soybean Trypsin Inhibitors 1,” 1969.
[26] A. L. Shapiro, E. Viñuela, and J. v. Maizel Jr., “Molecular weight estimation of polypeptide chains by electrophoresis in SDS-polyacrylamide gels,” *Biochem Biophys Res Commun*, vol. 28, no. 5, pp. 815–820, Sep. 1967, doi: 10.1016/0006-291X(67)90391-9.
[27] D. L. Holmes, N. C. Stellwagen, D. L. Holmes, and N. C. Stellwagen, “Estimation of polyacrylamide gel pore size from Fergwson plots of linear DNA fragments 11. Comparison of gels with different crosslinker concentrations, added agarose and added linear polyacrylamide,” 1991.
[28] A. Chrambach, “Huan-Tsung Chang Dispersion coefficients of conalbumin and DNA fragments in gel electrophoresis Dispersion coefficients of a protein and DNA fragment in polyacrylamide gel electrophoresis as a function of parameters defining the effective gel pore size and particle size,” 1995.
[29] K. A. Ferguson, “Starch-gel electrophoresis—Application to the classification of pituitary proteins and polypeptides,” *Metabolism*, vol. 13, no. 10, pp. 985–1002, 1964, doi: 10.1016/S0026-0495(64)80018-4.
[30] I. Wittig and H. Schägger, “Features and applications of blue-native and clear-native electrophoresis,” *Proteomics*, vol. 8, no. 19. pp. 3974–3990, Oct. 2008. doi: 10.1002/pmic.200800017.

[31] M. M. Camacho-Carvcajal, B. Wollscheid, R. Aebersold, V. Steimle, and W. W. A. Schamel, "Two-dimensional Blue Native/SDS gel electrophoresiss of multi-protein complexes from whole cellular lysates: A proteomics approach," *Molecular and Cellular Proteomics*, vol. 3, no. 2, pp. 176–182, Feb. 2004, doi: 10.1074/mcp.T300010-MCP200.

[32] D. P. Blattler and F. J. Reithel, "Molecular weight determinations and the influence of gel density, protein charges and protein shape in polyacrylamide gel electrophoresis," *J Chromatogr A*, vol. 46, pp. 286–292, 1970.

[33] H. Schaägger, W. A. Cramer, and G. von Jagow, "Analysis of molecular masses and oligomeric states of protein complexes by blue native electrophoresis and isolation of membrane protein complexes by two-dimensional native electrophoresis," *Anal Biochem*, vol. 217, no. 2, pp. 220–230, 1994, doi: 10.1006/abio.1994.1112.

[34] A. K. Bhuyan, "On the mechanism of SDS-induced protein denaturation," *Biopolymers*, vol. 93, no. 2, pp. 186–199, 2010, doi: 10.1002/bip.21318.

[35] W. N. Burnette, "'Western Blotting': Electrophoretic transfer of proteins from sodium dodecyl sulfate-polyacrylamide gels to unmodified nitrocellulose and radiographic detection with antibody and radioiodinated protein A," *Anal Biochem*, vol. 122, no. 2, pp. 195–203, 1981.

[36] K. M. Bischoff, L. Shi, and P. J. Kennelly, "The detection of enzyme activity following sodium dodecyl sulfate- polyacrylamide gel electrophoresis," *Analytical Biochemistry*, vol. 260, no. 1. pp. 1–17, 1998. doi: 10.1006/abio.1998.2680.

[37] D. Rodbard and A. Chrambach, "Unified Theory for Gel Electrophoresis and Gel Filtration*," 1970.

[38] P. C. Wankat, "Unified separation science. By J. Calvin Giddings, Wiley, New York, 320 pp., 1991," *AIChE Journal*, vol. 38, no. 8, pp. 1303–1303, Aug. 1992, doi: 10.1002/AIC.690380818.

[39] Q. Pan, K. A. Yamauchi, and A. E. Herr, "Controlling Dispersion during Single-Cell Polyacrylamide-Gel Electrophoresis in Open Microfluidic Devices," *Anal Chem*, vol. 90, no. 22, pp. 13419–13426, Nov. 2018, doi: 10.1021/acs.analchem.8b03233.

[40] A. E. Herr and A. K. Singh, "Photopolymerized cross-linked polycrylamide gels for on-chip protein sizing," *Anal Chem*, vol. 76, no. 16, pp. 4727–4733, Aug. 2004, doi: 10.1021/AC049686U/ASSET/IMAGES/LARGE/AC049686UF00006.JPEG.

[41] D. Wu, J. Qin, and B. Lin, "Electrophoretic separations on microfluidic chips," *J Chromatogr A*, vol. 1184, no. 1–2, pp. 542–559, Mar. 2008, doi: 10.1016/J.CHROMA.2007.11.119.

[42] T. Rabilloud, "Solubilization of proteins for electrophoretic analyses," *Electrophoresis*, vol. 17, no. 5, pp. 813–829, Jan. 1996, doi: 10.1002/ELPS.1150170503.

[43] T. Berkelman, "Removal of interfering substances in samples prepared for two-dimensional (2-D) electrophoresis.," *Methods Mol Biol*, vol. 424, pp. 51–62, 2008

[44] W. J. Hurkman and C. K. Tanaka, "Solubilization of Plant Membrane Proteins for Analysis by Two-Dimensional Gel Electrophoresis," *Plant Physiol*, vol. 81, no. 3, pp. 802–806, Jul. 1986, doi: 10.1104/PP.81.3.802.

[45] A. Posch, Ed., “2D PAGE: Sample Preparation and Fractionation,” vol. 424, 2008, doi: 10.1007/978-1-60327-064-9.
[46] A. Al-Mahrouki, M. Berezovski, and S. N. Krylov, “Zhulin Pang,” 2006, doi: 10.1002/elps.200500732.
[47] M. F. Mora, J. Felhofer, A. Ayon, and C. D. Garcia, “Surfactants as a Preferred Option to Improve Separation and Electrochemical Detection in Capillary Electrophoresis,” vol. 41, no. 2, pp. 312–334, Jan. 2008, doi: 10.1080/00032710701792927.
[48] D. Linke, “Chapter 34 Detergents: An Overview,” *Methods Enzymol*, vol. 463, no. C, pp. 603–617, Jan. 2009, doi: 10.1016/S0076-6879(09)63034-2.
[49] D. Otzen, “Protein–surfactant interactions: A tale of many states,” *Biochimica et Biophysica Acta (BBA) - Proteins and Proteomics*, vol. 1814, no. 5, pp. 562–591, May 2011, doi: 10.1016/J.BBAPAP.2011.03.003.
[50] M. R. Stoner, D. A. Dale, P. J. Gualfetti, T. Becker, and T. W. Randolph, “Surfactant-induced unfolding of cellulase: Kinetic studies,” *Biotechnol Prog*, vol. 22, no. 1, pp. 225–232, Jan. 2006, doi: 10.1021/BP0501468.
[51] K. K. Andersen *et al.*, “The Role of Decorated SDS Micelles in Sub-CMC Protein Denaturation and Association,” *J Mol Biol*, vol. 391, no. 1, pp. 207–226, Aug. 2009, doi: 10.1016/J.JMB.2009.06.019.
[52] M. Fu, J.-C. Leong, C.-F. Lin, C.-H. Tai, and C.-H. Tsai, “High performance microfluidic capillary electrophoresis devices”, doi: 10.1007/s10544-007-9049-3.
[53] C. W. Huck and G. K. Bonn, “Analysis of Proteins by Capillary Electrophoresis.”
[54] M. Tabuchi, Y. Kuramitsu, K. Nakamura, and Y. Baba, “Rapid Subpicogram Protein Detection on a Microchip without Denaturing,” 2003, doi: 10.1021/pr034009m.
[55] K. L. Saar, Q. Peter, T. Müller, P. K. Challa, T. W. Herling, and T. P. J. Knowles, “Rapid two-dimensional characterisation of proteins in solution”, doi: 10.1038/s41378-019-0072-3.
[56] R. F. Renzi *et al.*, “Hand-Held Microanalytical Instrument for Chip-Based Electrophoretic Separations of Proteins,” *TrAC, Trends Anal. Chem*, vol. 979, no. 3, p. 435, 2002, doi: 10.1021/ac049214f.
[57] C.-H. Lin, Y.-N. Wang, and M. Fu, “Integrated microfluidic chip for rapid DNA digestion and time-resolved capillary electrophoresis analysis ARTICLES YOU MAY BE INTERESTED IN,” *Biomicrofluidics*, vol. 6, p. 12818, 2012, doi: 10.1063/1.3654950.
[58] E. T. Lagally, P. C. Simpson, and R. A. Mathies, “Monolithic integrated microfluidic DNA amplification and capillary electrophoresis analysis system,” *Sens Actuators B Chem*, vol. 63, no. 3, pp. 138–146, May 2000, doi: 10.1016/S0925-4005(00)00350-6.
[59] D. Schmalzing, L. Koutny, A. Adourian, P. Belgrader, P. Matsudaira, and D. Ehrlich, “DNA typing in thirty seconds with a microfabricated device,” *Proceedings of the National Academy of Sciences*, vol. 94, no. 19, pp. 10273–10278, Sep. 1997, doi: 10.1073/PNAS.94.19.10273.
[60] E. A. Redman, J. S. Mellors, J. A. Starkey, and J. M. Ramsey, “Characterization of Intact Antibody Drug Conjugate Variants Using Microfluidic Capillary Electrophoresis-Mass Spectrometry,” *Anal Chem*, vol. 88, no. 4, pp. 2220–2226, Feb. 2016, doi:

10.1021/ACS.ANALCHEM.5B03866/ASSET/IMAGES/LARGE/AC-2015-038667_0007.JPEG.
[61] K. Khatri *et al.*, “Microfluidic Capillary Electrophoresis–Mass Spectrometry for Analysis of Monosaccharides, Oligosaccharides, and Glycopeptides,” *Anal. Chem*, vol. 89, p. 47, 2017, doi: 10.1021/acs.analchem.7b00875.
[62] A. Manz, N. Graber, and H. M. Widmer, “Miniaturized total chemical analysis systems: A novel concept for chemical sensing,” *Sens Actuators B Chem*, vol. 1, no. 1–6, pp. 244–248, 1990, doi: 10.1016/0925-4005(90)80209-I.
[63] D. Huh, G. A. Hamilton, and D. E. Ingber, “From 3D cell culture to organs-on-chips,” *Trends in Cell Biology*, vol. 21, no. 12. pp. 745–754, Dec. 2011. doi: 10.1016/j.tcb.2011.09.005.
[64] A. E. Herr *et al.*, “Microfluidic immunoassays as rapid saliva-based clinical diagnostics,” 2007.
[65] M. A. Kapil, “Microfluidic technologies for rapid, high-throughput screening and selection of antibodies for disease diagnostics and novel therapeutics,” 2015.
[66] R. Wang, J. Wu, X. He, P. Zhou, and Z. Shen, “A sample-in-answer-out microfluidic system for the molecular diagnostics of 24 hpv genotypes using palm-sized cartridge,” *Micromachines (Basel)*, vol. 12, no. 3, pp. 1–14, Mar. 2021, doi: 10.3390/mi12030263.
[67] F. Lan, B. Demaree, N. Ahmed, and A. R. Abate, “Single-cell genome sequencing at ultra-high-throughput with microfluidic droplet barcoding,” *Nature Publishing Group*, vol. 35, 2017, doi: 10.1038/nbt.3880.
[68] E. Meng, “Biomedical Microsystems,” *Biomedical Microsystems*, pp. 1–392, Sep. 2010, doi: 10.1201/9781439894521/BIOMEDICAL-MICROSYSTEMS-ELLIS-MENG.
[69] “Introduction to Microfluidics - Patrick Tabeling - Google Books.”
[70] J. J. Kim, M. J. Kim, S. Choe, and M. Wautelet, “Scaling laws in the macro-, micro-and nanoworlds,” 2001.
[71] M. Z. Rashed, N. G. Green, and S. J. Williams, “Scaling law analysis of electrohydrodynamics and dielectrophoresis for isomotive dielectrophoresis microfluidic devices,” *Electrophoresis*, vol. 41, no. 1–2, pp. 148–155, Jan. 2020, doi: 10.1002/elps.201900311.
[72] H. Bruus, “Chapter 1 Governing Equations in Microfluidics,” *Microscale Acoustofluidics*, pp. 1–28, Dec. 2014, doi: 10.1039/9781849737067-00001.
[73] J. Vlassakis and A. E. Herr, “Joule Heating-Induced Dispersion in Open Microfluidic Electrophoretic Cytometry,” *Anal Chem*, vol. 89, no. 23, pp. 12787–12796, Dec. 2017, doi: 10.1021/acs.analchem.7b03096.
[74] Y. Sun, “Microfluidic capillary electrophoresis chip techniques: Theory and different separation modes,” *Multidisciplinary Microfluidic and Nanofluidic Lab-on-a-Chip: Principles and Applications*, pp. 99–142, Jan. 2021, doi: 10.1016/B978-0-444-59432-7.00002-9.
[75] T. A. Duncombe *et al.*, “Hydrogel Pore-Size Modulation for Enhanced Single-Cell Western Blotting,” *Advanced Materials*, vol. 28, no. 2, pp. 327–334, Jan. 2016, doi: 10.1002/adma.201503939.

[76] C. C. Kang *et al.*, "Electrophoretic cytopathology resolves ERBB2 forms with single-cell resolution," *NPJ Precis Oncol*, vol. 2, no. 1, Dec. 2018, doi: 10.1038/s41698-018-0052-3.
[77] N. Lion, F. Reymond, H. H. Girault, and J. S. Rossier, "Why the move to microfluidics for protein analysis?," *Curr Opin Biotechnol*, vol. 15, no. 1, pp. 31–37, 2004, doi: 10.1016/J.COPBIO.2004.01.001.
[78] M. Frenkel-Morgenstern *et al.*, "Dynamic Proteomics: a database for dynamics and localizations of endogenous fluorescently-tagged proteins in living human cells", doi: 10.1093/nar/gkp808.
[79] J. Lippincott-Schwartz, E. Snapp, and A. Kenworthy, "Studying protein dynamics in living cells," *Nat Rev Mol Cell Biol*, vol. 2, pp. 444–456, 2001
[80] N. J. Bruce, G. K. Ganotra, D. B. Kokh, S. K. Sadiq, and R. C. Wade, "New approaches for computing ligand–receptor binding kinetics," *Curr Opin Struct Biol*, vol. 49, pp. 1–10, Apr. 2018, doi: 10.1016/J.SBI.2017.10.001.
[81] B. G. Regulatory and J. Carey, "Citation: Carey, J. Affinity, Specificity, and Cooperativity of DNA Binding Affinity, Specificity, and Cooperativity of DNA Binding by Bacterial Gene Regulatory Proteins," *Proteins. Int. J. Mol. Sci*, vol. 2022, p. 562, 2022, doi: 10.3390/ijms23010562.
[82] G. O'Hurley *et al.*, "Garbage in, garbage out: A critical evaluation of strategies used for validation of immunohistochemical biomarkers," *Molecular Oncology*, vol. 8, no. 4. John Wiley and Sons Ltd, pp. 783–798, Jun. 01, 2014. doi: 10.1016/j.molonc.2014.03.008.
[83] J. E. Gilda, R. Ghosh, J. X. Cheah, T. M. West, S. C. Bodine, and A. v. Gomes, "Western blotting inaccuracies with unverified antibodies: Need for a Western Blotting Minimal Reporting Standard (WBMRS)," *PLoS One*, vol. 10, no. 8, Aug. 2015, doi: 10.1371/journal.pone.0135392.

Chapter 2: Measuring expression heterogeneity of single-cell cytoskeletal protein complexes

Reproduced with permission from:

Vlassakis, J.*, **Hansen, L.L.*,** Higuchi-Sanabria, R. *et al.* Measuring expression heterogeneity of single-cell cytoskeletal protein complexes. *Nat Commun* **12**, 4969 (2021). https://doi.org/10.1038/s41467-021-25212-3. (* These authors contributed equally)

2.1: Abstract

Multimeric cytoskeletal protein complexes orchestrate normal cellular function. However, protein-complex distributions in stressed, heterogeneous cell populations remain unknown. Cell staining and proximity-based methods have limited selectivity and/or sensitivity for endogenous multimeric protein-complex quantification from single cells. We introduce micro-arrayed, differential detergent fractionation to simultaneously detect protein complexes in 100s of individual cells. Fractionation occurs by 60 s size-exclusion electrophoresis with protein complex-stabilizing buffer that minimizes depolymerization. Proteins are measured with a ~5-hour immunoassay. Co-detection of cytoskeletal protein complexes in U2OS cells treated with filamentous actin (F-actin) destabilizing Latrunculin A detects a unique subpopulation (~2%) exhibiting downregulated F-actin, but upregulated microtubules. Thus, some cells may upregulate other cytoskeletal complexes to counteract the stress of Latrunculin A treatment. We also sought to understand the effect of non-chemical stress on cellular heterogeneity of F-actin. We find heat shock may dysregulate filamentous and globular actin correlation. In this work, our assay overcomes selectivity limitations to biochemically quantify single-cell protein complexes perturbed with diverse stimuli.

2.2: Introduction

Over 80,000 protein complexes comprised of interacting proteins regulate processes from proteostasis to transcription[1]. A critical set of multimeric protein complexes form the cell cytoskeleton: actin filaments, microtubules, and intermediate filaments. For example, actin dynamically polymerizes and depolymerizes[2,3] between monomeric G-actin (~42 kDa) and filamentous F-actin[4] to determine cell morphology, motility, and proliferation[5]. F-actin is considered the functional actin species in the cytoskeleton. Thus, the F-actin ratio (or F-actin abundance divided by total actin) is a metric for cytoskeletal integrity. F-actin levels can be increased in metastatic cancer cells[5], thus underpinning the design of oncology drugs that disrupt F-actin filaments[6]. In addition, microtubule stabilizing chemotherapeutics (e.g., taxanes) are widely used in treatment of numerous cancers[7] (e.g., breast, lung, prostate). However, development of taxane-resistant cell subpopulations[8] requires further advances to screen drugs that target the cytoskeleton. Quantifying the distribution of cytoskeletal protein complexes in single cells would inform drug development and help elucidate stress-induced cancer transformations.

To understand cytoskeletal protein-complex expression heterogeneity, no existing method combines the needed detection sensitivity, throughput, and selectivity for multimeric protein complexes in single cells. Single-cell, bottom-up mass spectrometry has been demonstrated,[9,10] with identification of up to 1000 protein groups from individual cells with the nanoPOTS system[11]. Bottom-up mass spectrometry digests proteins and cannot determine protein-complex stoichiometry like top-down mass spectrometry of intact proteins. However, lossy sample fractionation in top-down mass spectrometry limits identification of protein complexes from low-cell number samples[12]. Indeed, with nanoPOTS integrated with top-down mass spectrometry, only ~170 of over a million possible proteoforms were detectable from ~70 pooled HeLa cells[13]. Thus, while highly multiplexed, top-down mass spectrometry currently lacks single-cell resolution for protein complexes. Targeted approaches such as proximity ligation assay and FRET achieve single-cell sensitivity and can assess cellular heterogeneity with flow cytometry readout (10,000 or more cells[14]). Proximity ligation assay and FRET rely on adjacent oligo-bound antibodies or fluorescent probes to infer that two proteins are interacting[15,16]. As proximity-based techniques are designed to measure 1:1 interaction, the most commonly used probes (whether fluorophores for FRET, or antibody-oligonucleotide conjugates for proximity ligation assay) do not distinguish multi-component or multimeric complexes from 1:1 complexes. Further, with flow cytometry, it is challenging to discern protein complexes from monomeric proteins without a selective probe. Finally, actin-specific detection methods are numerous, but suffer from limitations impacting sensitivity, selectivity and applicability to other cytoskeletal protein complexes. Visualization of the actin cytoskeleton relies on fluorescently tagged actin (e.g., GFP-actin fusion or split GFP-actin fusion[17]), GFP-fused actin binding proteins or peptides (e.g., Lifeact, F-tractin, Utrophin), nanobodies[18], or chemicals that directly bind actin (e.g., phalloidin). Such molecules may alter cytoskeletal dynamics both *in vitro* and *in vivo*[19–21]. Phalloidin competes with, or is dissociated by, endogenous actin-binding proteins[22,23] and actin-targeting drugs, such as Jasplakinolide[24]. Bulk ultracentrifugation overcomes these limitations while sacrificing single-cell resolution. In bulk ultracentrifugation, mild lysis in F-actin stabilization buffer solubilizes G-actin and preserves F-actin. The supernatant (G-actin) and pellet (F-actin) fractions are subsequently quantified by western blot or DNase inhibition assay[25]. However, bulk ultracentrifugation typically requires ~10^7 cells, masking underlying cell-to-cell variation[25].

In this work, we address gaps in multimeric protein-complex quantification by introducing Single-cell protein Interaction Fractionation Through Electrophoresis and immunoassay Readout, or SIFTER. With sequential differential detergent fractionation and bi-directional, single-cell polyacrylamide gel electrophoresis (originally developed for nuclear versus cytoplasmic protein separation[26]), we electrophoretically separate monomers from protein complexes. Single cells are gravity-settled in microwells formed in polyacrylamide, where the microwell aspect ratio is selected to maximize single-cell microwell occupancy[27]. Here, each cell is lysed in situ in buffer designed to maintain protein complexes. Under an applied electric field, the gel size-excludes protein complexes larger than ~740 kDa to the microwell. Small monomeric proteins electromigrate into the gel in two steps: first from the monomeric fraction, and second from the intentionally depolymerized protein complex fraction after a buffer exchange. SIFTER fractionates protein complexes in < 1 min, or 40× faster than the ultracentrifugation assay. The thin SIFTER gel (0.5 mm thick) minimizes resistive heating that could prematurely depolymerize or dissociate protein complexes. Owing to the arrayed format and open microfluidic design, hundreds of fractionation separations are performed

simultaneously. After fractionation and bi-directional electrophoresis, both the depolymerized protein complex (e.g., F-actin, microtubule, and/or intermediate filament) and monomer (e.g., G-actin, β-tubulin, or vimentin) states are blotted (or immobilized) in distinct gel regions abutting each microwell. Protein complex and monomer states are quantified by in-gel immunoprobing, allowing target multiplexing[27]. We applied SIFTER to four basic questions. First, do two well-studied actin-targeting drugs (Latrunculin A and Jasplakinolide) induce variation in F-actin complex-levels in single cells compared to controls? Second, as a corollary, does Latrunculin A yield cellular phenotypes distinct from controls with different organization of other cytoskeletal protein complexes, such as microtubules and intermediate filaments? Third, what is the distribution of the F-actin ratio across a population of single cells? Fourth, how does heat shock, another cellular stress, shift the F-actin ratio distribution and coordination between F- and G-actin at the single-cell level? We show SIFTER is a versatile method for understanding cellular heterogeneity – at single-cell resolution – in protein-complex levels in response to perturbation.

2.3: Materials and Methods

Chemicals: Tetramethylethylenediamine (TEMED, T9281), 40% T, 3.4% C acrylamide/bis-acrylamide (29:1) (A7802), N,N,N′,N′-, ammonium persulfate (APS, A3678), sodium deoxycholate (NaDOC, D6750), sodium dodecyl sulfate (SDS, L3771), bovine serum albumin (BSA, A7030), dithioerythritol (DTE, D8255), triton X-100 (X100), urea (U5378), β-Mercaptoethanol (M3148), anhydrous magnesium chloride ($MgCl_2$, 814733) and dimethylsulfoxide (DMSO, D2438) were acquired from Sigma Aldrich. An Ultrapure Millipore filtration system provided deionized water (18.2 MΩ). PharmAgra Laboratories custom-synthesized N-[3-[(3-Benzoylphenyl)- formamido] propyl] methacrylamide (BPMAC). Phosphate buffered saline was purchased from VWR (10X PBS, 45001−130). Tris glycine (10X) buffer was obtained from Bio-Rad (25 mM Tris, pH 8.3; 192 mM glycine, #1610734). Petroleum jelly (Cumberland Swan Petroleum Jelly, cat. no. 18−999−1829). Tris-HCl was obtained from Fisher Scientific (1M, pH = 7.5; Corning MT46030CM), while 0.5 M Tris-HCl, pH 6.8 was purchased from Teknova (T1568). Photoinitiator 2,2-Azobis(2-methyl-N-(2-hydroxyethyl) propionamide) (VA-086) was acquired from FujiFilm Wako Pure Chemical Corporation. Gel Slick was purchased from Lonza (#50640). Tris Buffered Saline with Tween 20 (TBST-10X) was procured from Cell Signaling Technology (9997S). Paraformaldehyde (4% EM grade) was purchased from Electron Microscopy Sciences (157-4).

Cell culture: All cell lines were authenticated by short tandem repeat profiling by the UC Berkeley Cell Culture facility and tested negative for mycoplasma. Naive U2OS cells were purchased from the UC Berkeley Cell Culture Facility. BJ fibroblasts expressing hTERT and Cas9 were provided by the Dillin lab. U2OS RFP-Lifeact cells were previously generated by the Kumar lab[91] at UC Berkeley, and kindly provided for this study. MDA-MB-231 GFP-actin cells were kindly provided by the Drubin lab at UC Berkeley. BJ fibroblasts and U2OS (RFP-Lifeact and naive) cells were maintained in DMEM (11965, ThermoFisher Scientific) supplemented with 10% FBS (100-106, GeminiBio), 1% penicillin/streptomycin (15140-122, ThermoFisher Scientific), and 1% non-essential amino acids (11140-050, ThermoFisher Scientific), while MDA-MB-231 GFP-actin cells were maintained in the same media minus the 1% non-essential amino acids. All cells were cultivated in a humidified incubator in 5% CO_2 kept at 37 °C. Cells were sub-cultured at ~80% confluency and detached with 0.05% Trypsin-EDTA (Gibco #25300-054) for 3 min. Each SIFTER assay was performed on a distinct single-cell suspension.

Generation of RFP-Lenti MDA-MB-231 GFP-Actin cells: MDM-MB-231 GFP-actin cells were a kind gift from the laboratory of Dr. David Drubin. Genome editing was performed at the genomic locus by integrating TagGFP (see Source Data for sequence) at the genomic locus for *ACTB*. Verification of genome editing was performed via standard PCR and sequencing. Briefly, DNA was collected from cells using the Qiagen DNeasy Blood and Tissue Kit (69506) as per manufacturer's guidelines. 100 ng of genomic DNA was used for PCR and sequencing was performed using standard sanger sequencing (primers provided in **Table 2.1**). A schematic for genome editing is provided in **Figure 2.1**. MDA-MB-231 GFP-actin cells were infected with lentivirus containing CD510B-1_pCDH-CMV-MCS-ED1-Puro (SystemBio) modified to carry TagRFP (see Source Data for sequence) under the CMV promoter.

Table 2.1: Primers used in the study.

Type of Primer	Sequence
Forward Primer for PCR	5'GGACTCAAGGCGCTAACTGC3'
Reverse Primer for PCR	5' GGTACTTCAGGGTGAGGATGCC3'
Primer for Sanger Sequencing	5'GCTTCCTTTGTCCCCAATCTGG3'

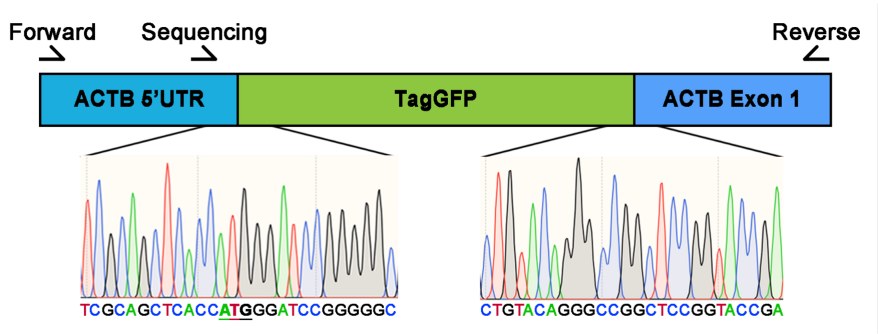

Figure 2.1: Schematic of genome edit generating the GFP-actin fusion in the MDA-MB-231 cells. Actin gene (ACTB) exon, inserted GFP sequence (TagGFP) and untranslated region (UTR) shown.

SIFTER assay (step-by-step protocol provided on Protocol Exchange[93]): Buffers and gel lid incubation: F-actin stabilization lysis buffer used was 10 mM Tris-HCl, 1% Triton X-100, 2 mM $MgCl_2$, and 0.5 mM DTE (titrated to pH=7.4). The DTE was added at the time of a given experiment. The depolymerization buffer was prepared as a 1.56x RIPA buffer such that upon addition of 8 M urea, the final buffer composition was 0.5x Tris glycine, 0.5% SDS, 0.25% sodium deoxycholate, 0.1% Triton X-100, 8 M urea, pH = 8.3. Urea was added fresh at the time of the experiment and allowed to dissolve at 75 °C. Hydrogel lids (15%T, 3.3% C) were photopolymerized as previously described between Gel Slick-coated glass plates offset with a 500 µm spacer[26]. Hydrogel lids were incubated overnight at 4 °C in either the F-actin

stabilization or the depolymerization buffer (before urea or DTE addition). Upon complete preparation of the urea-containing depolymerization buffer, the buffer was introduced to the gel lids in a water bath set to 75 °C and incubated for ~30 min before beginning the experiments. F-actin stabilization buffers and gel lids were kept at room temperature. Gel lids and buffers were only stored for up to 2 weeks, and buffer solution was never re-used.

Polyacrylamide fractionation gels (8%T and 3.3%C with 3 mM BPMAC incorporated) were polymerized on SU-8 micro-post molds as described elsewhere[27]. Trypsinization was performed for 3 min at 37 °C, and cells in PBS (10010049, Thermo Fisher Scientific, pH = 7.4, magnesium and calcium free) settled in the microwell array for 10 min. Trypsinized cells were introduced to the microwell array in 1X PBS solution for passive gravity settling settling[27]. Every few minutes, the fractionation gel is gently slid back and forth to distribute cells across the gel. After ten minutes, the gel is placed at a slight incline and excess cells are lightly rinsed off the gel surface with PBS. Each replicate experiment was run with a different 1-cm petri dish of freshly trypsinized cells in suspension.

For the fractionation separation, the fractionation gel device was pre-incubated in 10 mM Tris-HCl (pH = 7.5) briefly before the glass slide was adhered to the surface of a custom 3D-printed PAGE chamber with petroleum jelly. A custom heater with a 12V PTC ceramic heating element (ELE147, Bolsen Tech) and PID temperature controller (ITC-106VH, Inkbird) was interfaced to the bottom surface of the PAGE chamber at 37 °C. The F-actin stabilization hydrogel lid was then applied to the array and cell lysis proceeded for 45 s before the electric field was applied (30 V cm^{-1}, 45 s for 42 kDa actin in U2OS or BJ fibroblasts, or 60 s for 69 kDa GFP-actin from the GFP-actin cells; Bio-Rad Powerpac basic power supply). Proteins were blotted, or bound to the fractionation gel, by UV-induced covalent immobilization to the BPMAC incorporated in the fractionation gel (Lightningcure LC5, Hamamatsu, 100% power, 45 s). The electrode terminals were reversed, and the hydrogel lid was exchanged with depolymerization buffer gel hydrogel lid for 45 s. PAGE was performed for the same duration in the opposite direction before a final UV photo-immobilization step (same UV power and duration). The glass slide was peeled from the PAGE chamber, and the fractionation gel was washed in 1X TBST for at least 30 min to overnight prior to immunoprobing.

Immunoprobing was performed as previously described[27], utilizing a rabbit anti-GFP antibody for GFP-actin (Abcam Ab290), rabbit anti-actin monoclonal antibody (Ab 200658 for BJ fibroblasts in Figure 3), rabbit anti-actin monoclonal antibody (Abcam Ab 218787 for U2OS cells), mouse anti-vimentin monoclonal antibody (Abcam Ab8978) and rabbit anti-β-tubulin monoclonal antibody (Abcam Ab6046). See additional antibodies tested in **Table 2.2**. Gels were incubated with 50 µl of 1:10 dilution of the stock primary antibody in TBST for two hours and then washed 2x for 30 min in 1X TBST. Donkey Anti-Rabbit IgG (H+L) Cross-Adsorbed Secondary Antibody, Alexa Fluor 647-labeled (A31573, Thermo Fisher Scientific), Donkey Anti-Mouse IgG (H+L) Cross-Adsorbed Secondary Antibody, Alexa Fluor 555-labeled (A31570, Thermo Fisher Scientific) and Donkey Anti-Mouse IgG (H+L) Cross-Adsorbed Secondary Antibody, Alexa Fluor 647-labeled (A31571, Thermo Fisher Scientific) were used at a 1:20 dilution in TBST for a one-hour incubation after 5 min of centrifugation at 10,000 xg. Two more 30-min TBST washes were performed prior to drying the gels in a nitrogen stream and imaging with a laser microarray scanner (Genepix 4300A, Genepix Pro 7 software, Molecular Devices). When immunoprobing with rhodamine-labeled anti-actin Fab (see **Table**

2.2) and Ab 200658, 1:5 dilutions were used. For the Fab, immunoprobing completed after the two-hour incubation and two 30-minute washes in TBST. For multiplexed analysis of actin, vimentin and β-tubulin protein complexes, actin and vimentin were immunoprobed together, the gels were chemically stripped[27] and then re-probed for β-tubulin. Chemical stripping was performed for at least one hour at 55 °C. Gels were briefly rinsed in fresh 1x TBST three times and then washed in 1x TBST for at least one hour prior to re-probing.

Images were analyzed as described elsewhere[27]. Briefly, the images were median filtered utilizing the Remove Outliers macro in Fiji (pixel radius = 2 and threshold = 50 AFU; except for the data presented in **Figures 2.7** and **Figure 2.16**). The images were then segmented, intensity profiles were generated for each separation lane and peaks were fitted to a Gaussian curve. For fits with an $R^2 > 0.7$ user-based quality control is performed, and area under the curve is calculated within two peak widths from the center on the background subtracted profile. The signal-to-noise ratio (SNR) of each peak is calculated with signal taken as the amplitude of the Gaussian fit. Noise is calculated as the standard deviation of pixel intensities in a background region at the edge of the region of interest (aligned with two peak widths from the peak center location of the Gaussian). We report the area-under-the-curve for peaks with SNR > 3, a criterion used when determining a lower limit of detection for a semi-quantitative assay. Image analysis was performed in MATLAB R2019b.

Table 2.2: **Summary of immunoprobing results with various antibodies**. Epitope information and valid applications indicated by the manufacturer are included. The 'Heater Status' column indicates whether the SIFTER assay was performed with the heater interfaced with the device during lysis and electrophoresis. Gels from the 'Without Heater' protocol were immunoprobed with 25 µl antibody solution instead of 50. Abbreviations: western blot (WB), enzyme-linked immunosorbent assay (ELISA), immunofluorescence (IF), immunohistochemistry (IHC), flow cytometry (flow), immunoprecipitation (IP), immunocytochemistry (ICC), amino acid (a.a.).

Vendor	Product #	Clonality	Epitope Info	Valid Applications	Separation results	Heater status
Millipore	MAB1501	Monoclonal (clone c4)	a.a. 50-70 (Chicken gizzard actin)	ELISA, IHC IF, ICC, & WB	F-actin band only (BJ fibroblasts)	With and without heater
CST	8456S	Monoclonal	C-terminus of β-actin (synthetic peptide)	WB, IF, IHC	F-actin band only (BJ fibroblasts)	Without heater
CST	8457	Monoclonal	Near N-terminus of β-actin (synthetic peptide)	WB, IF, Flow	F-actin band only (BJ fibroblasts)	With heater

CST	3700	Monoclonal	Near N-terminus of β-actin (synthetic peptide)	WB, IHC, IF, Flow	F-actin band only (BJ fibroblasts)	With heater
CST	4968S	Polyclonal	Residues around Asp244 (synthetic peptide)	WB, IHC	F-actin band only (BJ fibroblasts)	Without heater
Abcam	ab1801	Polyclonal	~residues 350 to C-terminus (peptide)	WB, IHC	No signal (BJ fibroblasts)	Without heater
Abcam	ab198991	Monoclonal	Synthetic peptide ~a.a. 300 to C-terminus	WB, IP	F-actin band only (BJ fibroblast)	With heater
Abcam	ab200658	Monoclonal	Synthetic peptide ~ a.a. 300 to C-terminus	WB, ICC, Flow	F-actin band with few G-actin bands (BJ fibroblast)	With heater
Abcam	ab218787	Monoclonal	Synthetic peptide corresponding to human actin	ICC, WB	F-actin band only (U2Os and BJ fibroblast)	With heater
Biorad	12004164	Unspecified; rhodamine-labeled Fab	Recombinant human beta β-actin expressed in e. Coli	WB	F-actin band and some G-actin bands (BJ fibroblasts)	Without heater

Temperature measurement in SIFTER: Temperature sensors (liquid crystal thermometers; Type C 30-60 °C with 5 °C intervals from ThermometerSite) were placed directly under the hydrogel lid (immersed in F-actin stabilization lysis buffer). The temperature was monitored while applying 30 V cm^{-1} across the electrodes of the electrophoresis chamber without interfacing with the custom heater.

Fluorescence imaging of cells in microwells, lysis and PAGE: Imaging was performed via time-lapse epi-fluorescence microscopy on an Olympus IX50 and IX51 inverted epifluorescence microscope (and thus the custom heater was not used as it would block the illumination path

through the PAGE chamber). The microscope was controlled using Metamorph software (Molecular Devices) and images were recorded with a CCD camera (Photometrics Coolsnap HQ2). The imaging setup included a motorized stage (ASI), a mercury arc lamp (X-cite, Lumen Dynamics) and a XF100-3 filter (Omega Optical) and 41017 (Chroma) for GFP and an XF111-2 filter for RFP (Omega Optical). Imaging was performed with a 10× magnification objective (Olympus UPlanFLN, NA 0.45 or UPLFLN10X2, NA 0.3) and 900 ms exposures with 1s intervals with U2OS RFP-Lifeact, and 2s exposure with 2s intervals with MDA-MB-231 GFP-actin (1x pixel binning). Exposure times were lowered for lysis imaging to 600 ms.

F-actin cell staining and drug treatment: Latrunculin A (Cayman Chemicals 10010630) was dissolved in DMSO as a 2 mM stock solution and stored at -20 °C until use. Jasplakinolide (Millipore-Sigma, 420107) was reconstituted in DMSO and stored at -20 °C for up to 3 months. Cells were incubated in the LatA for 60 min at 2 μM and in the Jpk for 120 min at 0.1 or 0.2 μM. Dosing concentration and duration to induce actin depolymerization were based on reported conditions for other cell types[62,92,94] and verified qualitatively by phalloidin staining and fluorescence microscopy of adherent cells. The DMSO control cells were exposed to 0.1% DMSO in cell culture media for the same time as the drug treated cells. Cells were fixed with 3.7% paraformaldehyde in 1X PBS (10 min at room temperature), and permeabilized with 0.1% Triton X-100 (for 5 min at room temperature and stained with Alexa Fluor 647-labeled phalloidin (20 min at room temperature, ThermoFisher Scientific, A22287).

Cells were imaged by epi-fluorescence with an Olympus IX70 inverted microscope controlled with Metamorph (Molecular Dynamics). Images were captured with an Andor iXon+ EMCCD camera (DU-885K-C00-#VP) with an Olympus LCPlanFl 40X (0.6 NA) objective, a mercury arc lamp (X-cite exacte, Lumen Dynamics) and a Chroma 49009 ET filter. Exposure time was 800 ms and pixel binning was 1x.

Flow cytometry analysis of phalloidin-stained cells: Fixed cells were incubated in permeabilization buffer (0.1% Triton X-100 in PBS) at room temperature for 10 minutes. Cells were then spun down and incubated in staining solution (66 nM AlexaFluor 594 phalloidin in PBS supplemented with 2% BSA) at 4 °C for 30 minutes. Finally, cells were washed twice with PBS and analyzed with flow cytometry using BD LSRFortessa (and Flowjo v10.6 software). To analyze stained cells, single cells were gated by forward and side scatter (Figure 2). Only single cells were included in the fluorescence analysis.

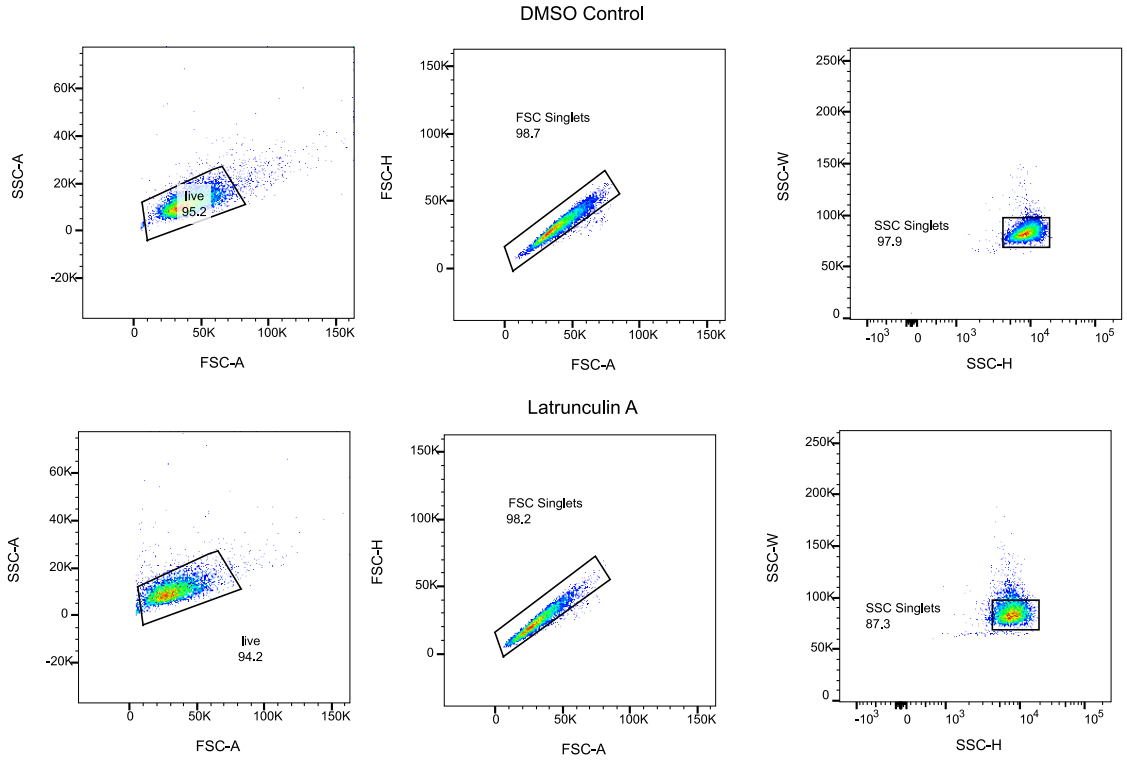

Figure 2.2: Area density plots showing gating strategy for flow cytometry data presented in Figure 7d for the DMSO control and Latrunculin A-treated cells. Blue points correspond to the lowest densities and red are the highest densities of the color scale. Abbreviations: Side Scatter Area (SSC-A), Forward Scatter Area (FSC-A), Side Scatter Width (SSC-W), Side Scatter Height (SSC-H). Values provided on each plot are the percentage of events within each gate out of total events. Cells were first gated on FSC and SSC areas for live cells (i.e., live at the time of fixation), then gated on FSC (FSC singlets) and SSC (SSC singlets) for single cells. Fluorescence analysis was performed only on single cells.

Heat shock treatment of cells: MDA-MB-231 GFP-actin RFP-lenti cells were incubated at 45 °C (VWR mini incubator, 10055-006) for heat shock, or at 37 °C in a humidified 5% CO_2 incubator for controls for 1-h prior to trypsinization and gravity settling in the fractionation gel.

Statistical analysis: Mann-Whitney test (with U test statistic) and Kruskal-Wallis test with post-hoc Dunn's test (Chi-squared test statistic), Spearman rank correlations, and QQ-plot generation with normal and gamma distributions were performed using pre-existing functions in MATLAB 2019b. All tests were two-sided. All boxplots include a centerline for the median, boxes at the 25th and 75th percentile and whiskers that extend to the extremes of the data. Violin plots were generated in RStudio (Version 0.99.903) using the library Vioplot. The boxplot within the kernel density plot displays boxes at the 25th and 75th percentile, a point at the median, and whiskers that extend to the extremes of the data. Beeswarm plots used the library swarm.

Cell Fishing clustering analysis: Standardization is by row for both the LatA treated and DMSO control data sets (expression level, or Gaussian protein peak AUC, for each protein complex) with the mean at 0 and standard deviation of 1. Initial agglomerative hierarchical clustering was performed separately for the LatA treated and DMSO control data sets utilizing Euclidean

distances, and the Ward linkage criterion (R version 3.6.1, NMF package). Distinct sub-clusters in the LatA treated data were further inspected as bait groups of cells inspired by the GeneFishing method described elsewhere[72]. We conducted an analogous analysis to GeneFishing, which we call Cell Fishing. Candidate cells from the DMSO control data sets were randomly split into subsamples of 100 cells, and each subsample was pooled together with the bait cells to form a sub-dataset. Semi-supervised clustering is applied to each sub-dataset using spectral analysis and a clustering algorithm based on the EM-fitted mixture Gaussian of two components model[95] (R version 3.6.1, mclust package). The subsampling protocol was repeated 3000 times for a given bait set, and cells were considered fished out if they had a capture frequency rate of 0.999 or higher.

2.4: Results

SIFTER design principles and characterization

To selectively detect cytoskeletal protein complexes from single cells, we integrate differential detergent fractionation, electrophoretic separation, and immunoassay steps into a single microdevice. An important set of dynamic protein complexes comprise the cytoskeleton, including F-actin filaments, microtubules (MT) and intermediate filaments (IF; **Figure 2.3a**). Two design considerations are central to our measurement of dynamic protein complexes: (1) discerning the protein complexes from monomers; and (2) maintaining protein complexes during fractionation. For the first design consideration, we focus on the F-actin filament, which is the smallest and most dynamic of the three cytoskeletal protein complexes. Each filament can be composed of up to 100s of globular G-actin monomers (k_{off} ~ 0.2 - 1.0 s^{-1} *in vivo*[28]). F-actin averages ~2.7 MDa (versus MT at ~178 MDa with 1 μm average MT length[29] and 1625 tubulin heterodimers per μm of MT[30], and IF at ~30 MDa for typical μm-scale IF[31] at >30 kDa per nm of filament[32]). F-actin polymerization proceeds rapidly once four G-actin are incorporated in a filament. Steady-state polymerization (k_{on} ~0.1-5 $\mu M^{-1}s^{-1}$)[28] yields a distribution of filament masses[33]. While the F-actin mass distribution below ~2700 kDa is unknown *in vivo*, F-actin is highly enmeshed. Thus, discerning F- (>160 kDa) vs. G-actin (42 kDa) requires coarse size cutoff (~100s of kDa), which should also fractionate MT and IF. On the second design consideration, rapid F-actin depolymerization occurs below the critical concentration of total actin (~0.2 - 2.0 μM *in vivo*). To maintain local concentrations of actin above the critical concentration demands < ~10× dilution during the assay, as cellular total actin is ~10-100 μM. Thus, the SIFTER fractionation gel contains microwells with ~10^8× smaller reaction volume versus bulk ultracentrifugation to minimize dilution. The microwells accommodate gravity-sedimented single cells[27] within the fractionation gel (**Figure 2.3a**). The open SIFTER device is suited to rapid serial introduction of buffers via interchangeable hydrogel lids to first lyse cells and stabilize protein complexes during fractionation, and then depolymerize or dissociate protein complexes to spatially separate monomers from protein complexes (**Figure 2.3b-c**).

To report both the state (protein complex *vs*. monomer) and amount of specific protein complexes per cell, SIFTER comprises five assay steps (**Figure 2.3c**). First, single trypsinized cells are gravity-settled in the microwell array (from a cell suspension[27]) and lysed in an F-actin stabilization buffer delivered by the hydrogel lid, creating a lysate containing the monomers and complexes. Second, protein complexes are fractionated from the smaller monomers by polyacrylamide gel electrophoresis (PAGE, 60 s), during which large protein complexes are size-

excluded from the gel and retained in each microwell. Monomers electrophorese into the gel and are immobilized (blotted) using a UV-induced covalent reaction to benzophenone methacrylamide integrated into the gel polymer network[27]. Covalent immobilization to the gel prevents monomer diffusion that would broaden the protein peak and result in protein loss out of the gel. Third, to depolymerize the complexes retained in each microwell, a protein-complex depolymerization buffer is introduced by another hydrogel lid. Fourth, we electrophorese the now depolymerized complexes into a region of the gel separate from the immobilized monomers, where depolymerized complexes are in turn immobilized. Fifth, in-gel immunoprobing (~5 hours) detects the immobilized populations of monomer and monomer depolymerized from the complexes (**Figure 2.3e-f**). We use a fluorescently labeled antibody probe against the protein (i.e., anti-actin antibody probe to detect F- and G-actin, and anti-vimentin antibody probe to detect vimentin monomers and intermediate filaments).

To maintain intact protein complexes in each microwell during PAGE fractionation, the F-actin stabilization buffer slows the natural depolymerization kinetics. The non-ionic detergent Triton X-100 at ~1% v/v lyses the cell and minimally alters in vitro polymerization rates of actin[25,34,35]. The addition of 2 mM $MgCl_2$ stabilizes F-actin complexes[25], as Mg^{2+} binds G-actin to lower depolymerization rates[33]. Consequently, only ~2% of total F-actin depolymerizes per minute in mammalian cells lysed in stabilization buffer[25], compatible with our goal to fractionate in ~1 min. Cell lysis depends on diffusion of Triton X-100 micelles, which requires ~10 s to reach the bottom of the microwells[36]. Imaging release of monomeric G-actin fused to fluorescent GFP from GFP-actin expressing breast cancer cells (MDA-MB-231 GFP-actin) within a microwell confirms a 45 s lysis yields only ~2.5-4× dilution of total actin to remain above the actin critical concentration (**Figure 2.3d**). Important to minimizing F-actin-complex depolymerization during the assay, SIFTER completes cell lysis and fractionation in <5 min, or ~40× faster than bulk ultracentrifugation.

Validation and benchmarking SIFTER

We first validated SIFTER by fractionating and quantifying the G-actin monomer *vs*. F-actin complexes in single MDA-MB-231 GFP-actin cells. We selected GFP-actin expressing cells to utilize fluorescence imaging to optimize cell lysis (**Figure 2.3d**) and PAGE conditions. Immunoprobing for GFP yields distinct Gaussian protein peaks corresponding to GFP G-actin (*G*) on the left and GFP F-actin (*F*) to the right of each microwell (**Figure 2.3e**). The area-under-the-curve of F-actin and G-actin peaks corresponds to the F-actin (F) and G-actin (G) protein fraction abundances, respectively. By design, the target peak is identified using a combination of reactivity with immunoprobe and migration distance (size). For immunoblots where dispersed signal between the target actin peak and microwell is both detectable and resolvable, the off-target signal is excluded from quantification. Immunoblots with non-Gaussian target signal are omitted from data analysis. We attribute the dispersed signal to either (or both): (i) cross-reactivity of the fluorescent antibody probes with smaller proteins and cellular material or (ii) injection dispersion arising from likely incomplete protein solubilization[37] (including dissociation of the filamentous actin we study here). Full solubilization of the F-actin filament may not be complete for all cells in the short 45-s lysis and solubilization period, a duration that is dictated by diffusive losses of protein out of the microwell prior to electrophoresis[26]. We calculate the F-actin ratio:

$$F_{ratio} = F / (F+G) \qquad (1)$$

for each cell. The MDA-MB-231 GFP-actin fusion cell average F_{ratio} = 0.45 ± 0.10 (standard deviation; n = 578 cells, from N = 3 SIFTER devices), in reasonable agreement *with* F_{ratio} ~0.5 for MDA-MB-231 from bulk ultracentrifugation[38]. With SIFTER, the F_{ratio} coefficient of variation is 22%, revealing single-cell variation obscured in the bulk assay. F_{ratio} variation measured by SIFTER includes cellular variation, such as the inverse correlation between the F_{ratio} and cell volume. For example, cells grown in microniches that controllably decrease cell volume by half undergo similar magnitude increase in F-actin and decrease in G-actin (which should correspond to ~2× increase in F_{ratio})[39].

Further, the F-actin stabilization buffer also maintains IF complexes (**Figure 2.3f**). We apply the F-actin stabilization buffer to the measurement of intermediate filament (IF) and microtubule (MT) cytoskeletal protein complexes. First, we note that MT and IF are relatively stable compared to F-actin. MT have depolymerization $t_{1/2}$ timescales of minutes[97] and IF experience subunit exchange ~10% over 7 hr[98]. Due to the similarity in protein complex-stabilizing buffers for each cytoskeletal protein complex (Triton X-100 ~0.5-1.0%, pH ~6.7-7.4, and inclusion of 1 mM $MgCl_2$ for MT[25, 99, 100], we determined the F-actin stabilization buffer employed in SIFTER could be usable for MT and IF fractionation.

As such, we define and quantify an *IF ratio:*

$$IF_{ratio} = IF/(IF + VIM_{monomer}) \qquad (2)$$

from the area-under-the-curve of the peaks, where $VIM_{monomer}$ is the amount of native vimentin monomer. The IF_{ratio} indicates the fraction of vimentin actively giving structure to the cell, the primary function of IF. We find MDA-MB-231 GFP-actin cells have an average IF_{ratio} = 0.63 ± 0.11 (error is the standard deviation; n = 168 cells, from N = 4 SIFTER devices measured on the same day). The significance of determining metrics such as F_{ratio} and IF_{ratio} with single-cell resolution is to detect small sub-populations of cells with distinctive filament and monomer distributions, especially the phenotypes that arise in response to stresses. Observed cell-to-cell variation in F_{ratio} and IF_{ratio} raises the intriguing question of whether cells compensate levels of one cytoskeletal protein complex for another. We investigate differential stress responses and compensation of cytoskeletal protein complexes later in this work.

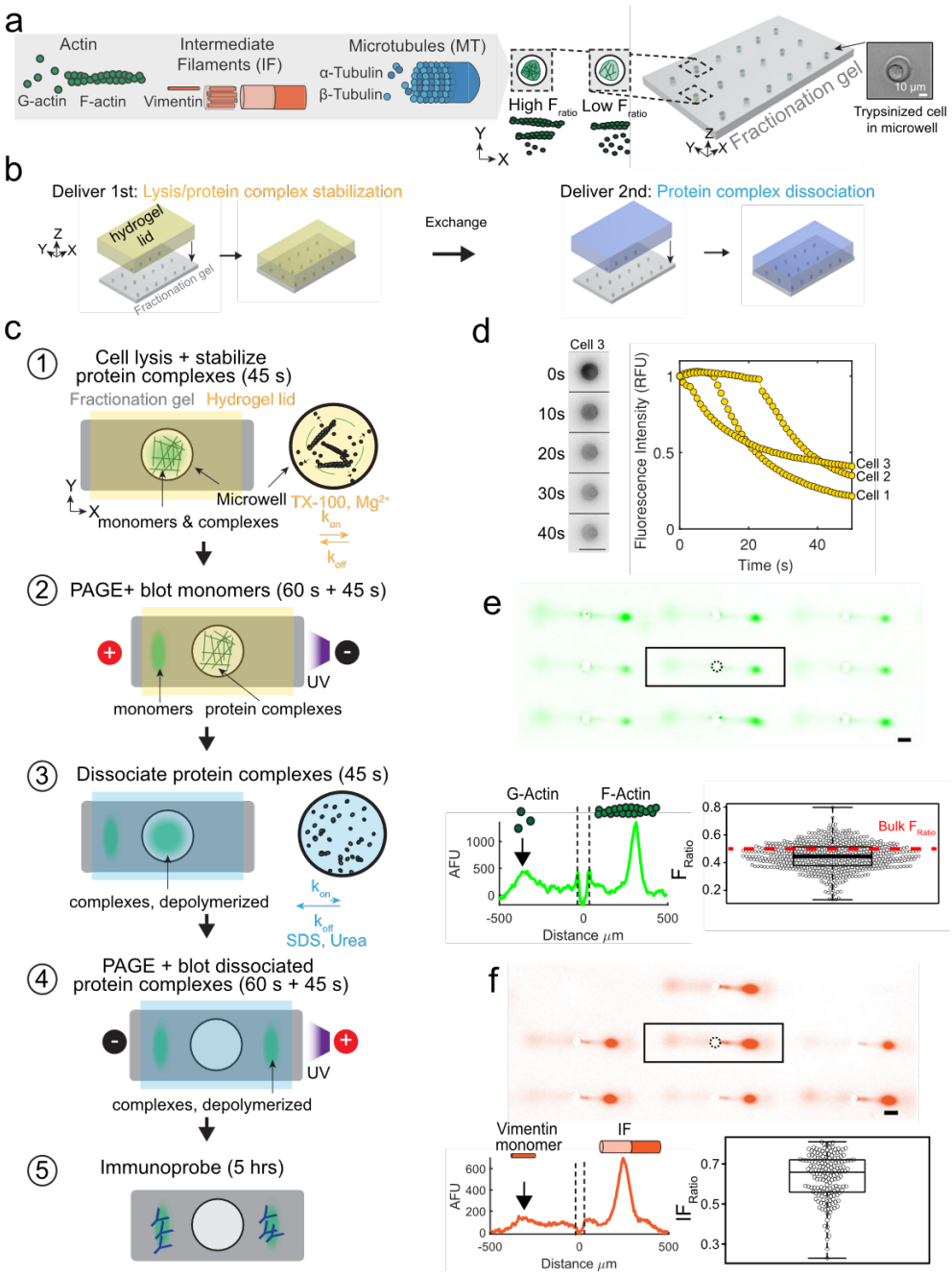

Figure 2.3: SIFTER detects cytoskeletal complexes from hundreds of single cells by on-chip integration of single-cell differential detergent fractionation and immunoblotting. (a) Schematic of three key cytoskeletal protein complexes: filamentous actin (F-actin; 4-100s of globular G-actin, 42 kDa each), microtubules (MT; assembled from α- and β-tubulin heterodimers) and intermediate filaments (IF; comprising vimentin monomers). Trypsinized cells contain the three cytoskeletal protein complexes and are heterogeneous with low to high F-actin ratios (F_{ratio}). Brightfield image shows a cell gravity settled into an individual microwell of a polyacrylamide fractionation gel. (b) Side-view schematic of hydrogel lid delivery of assay-stage optimized buffers to microwells in the fractionation gel. (c) The SIFTER assay comprises: 1) hydrogel lid delivery of protein complex-stabilizing lysis buffer

to the array; 2) polyacrylamide gel electrophoresis (PAGE) and UV-immobilization of monomers (e.g., G-actin) in the gel; 3) hydrogel lid delivery of protein-complex dissociation buffer; 4) PAGE of dissociated protein complexes (e.g., F-actin, depolymerized) in the opposite direction of monomers and UV immobilization; and 5) in-gel antibody immunoprobing. (d) Cell lysis monitoring: false-color fluorescence micrograph montage and quantification of single MDA GFP-actin cells in microwells (cells 1-3) upon lysis with F-actin stabilization buffer (lyses cell but retains F-actin). Scale bar is 100 μm. Total fluorescence in the microwell normalized to initial in-microwell fluorescence as a function of lysis time for n = 3 cells (yellow circles). (e) Immunoassay results: representative false-color micrograph of subset of the SIFTER array and intensity profile of GFP F-actin and GFP G-actin from single MDA-MB-231 GFP-actin cells (scale bar is 100 μm). Microwell annotated with dashed line. Boxplot with beeswarm (white circles) shows the F_{ratio} calculated from F- and G-actin peak area-under-the-curve from n = 578 single-cell protein complex separations from N = 3 SIFTER devices. Boxplot box edges are at 25th and 75th percentile, middle line is the median, and whiskers extend to minimum and maximum values of the data set. Red dashed line shows the F_{ratio} from a bulk assay[38]. (f) Representative false-color micrograph of a subset of the SIFTER array and intensity profile of vimentin from single MDA-MB-231 GFP-actin cells (scale bar is 100 μm). Boxplot with beeswarm (white circles) shows $IF_{ratio} = IF/(IF + VIM_{monomer})$, from n = 168 cells from N = 4 SIFTER devices. Boxplot box edges are at 25th and 75th percentile, middle line is the median, and whiskers extend to minimum and maximum values of the data set.

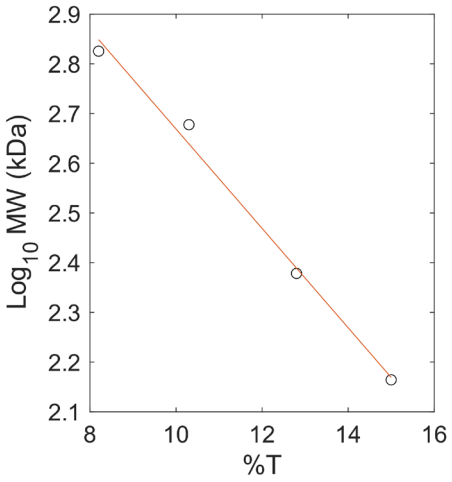

Figure 2.4: Scatter plot of protein size excluded in blue native polyacrylamide gel electrophoresis (black circles) as a function of Total acrylamide concentration (%T, g/mL) as reported by Wittig et al.[41] The linear fit is shown as a red line with equation: y = -0.0999T + 3.6683 (r^2 = 0.992).

To validate monomers *vs.* protein complex detection specificity, we determined the gel composition needed to fractionate F-actin (the smallest of the three cytoskeletal protein complexes) and directly observed PAGE of fluorescently labeled actin from single-cell lysates. The molecular mass cutoff for the gel depends on the total acrylamide concentration (%T). Based on native PAGE[40,41], the SIFTER cutoff for an 8%T gel is ~740 kDa (**Figure 2.4, Figure 2.5a**), or larger than 42 kDa G-actin, but smaller than an average ~2700 kDa F-actin. During PAGE of MDA-MB-231 GFP-actin cells (in which GFP is fused to both G- and F-actin), actin species indeed fractionate at the microwell edge (**Figure 2.5b**). Within 45 s of PAGE, the G-actin Gaussian protein band completely injects a mean distance of 350 ± 16 μm into the polyacrylamide gel (with mean peak width of 66 ± 8 μm, n = 275; errors are standard deviations from one SIFTER device). We confirm the actin state of the species in the microwell by imaging PAGE of U2OS cells expressing RFP-Lifeact, a common marker for F-actin[19]. The microwell retains the F-actin complexes (**Figure 2.5c**), with signal decrease attributable to diffusive losses[27] of RFP-Lifeact-bound G-actin out of the microwell and photobleaching. We hypothesize two factors lead to no observed F-actin electromigration into the gel, including RFP-Lifeact bound dimers[42]. First, small oligomers are a minor fraction of F-actin due to substantial dissociation rates[43]. Second, highly crosslinked filaments[23] remain enmeshed within the cytoskeleton even in lysed cells[44]. Further, we expect that free RFP-Lifeact would diffuse out of the microwell during cell lysis if present. Thus, we confirm that SIFTER fractionates F-actin complexes from single cells. Importantly, size exclusion may fractionate other protein complexes by adjusting the %T, as >99% of individual proteins of the mammalian proteome are larger than the molecular mass cutoff of even a denser 10%T gel[45].

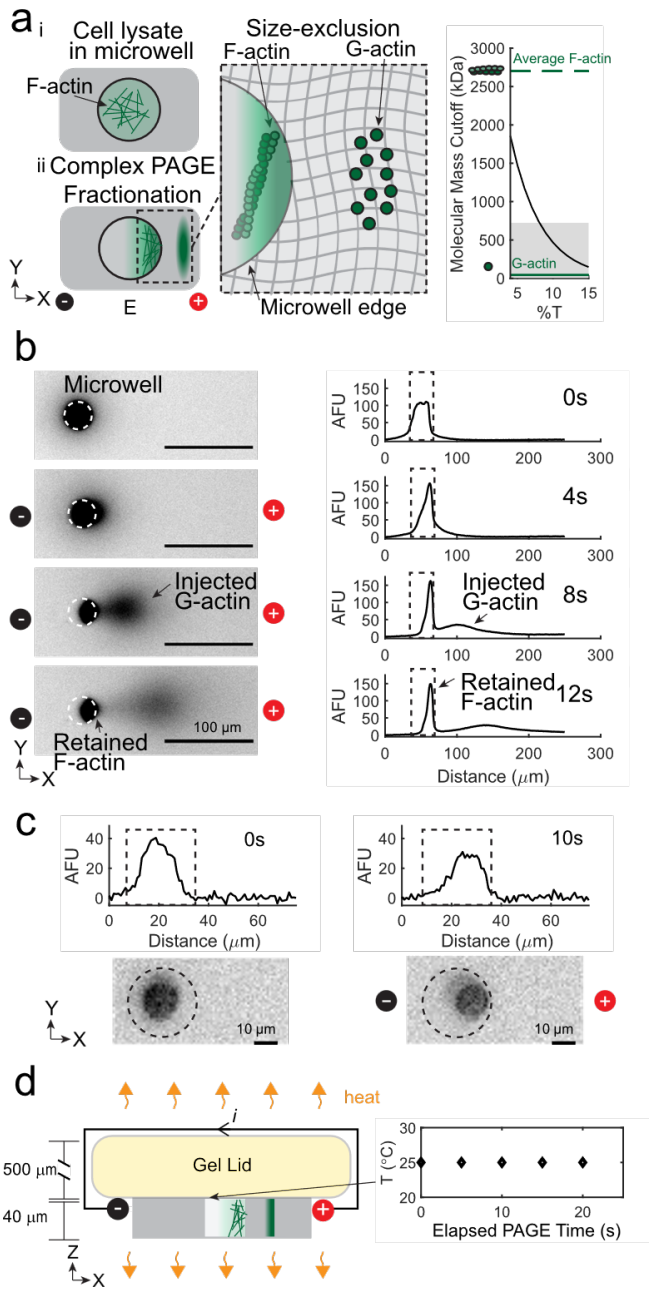

Figure 2.5: Size-based fractionation and efficient heat dissipation at the micro-scale provides molecular specificity to fractionate F-actin complexes from single cells. (a) Left: schematic of fractionation using polyacrylamide gel electrophoresis (PAGE) to separate F-actin complexes from G-actin monomers. Right: Estimated molecular mass cutoff as a function of gel density (%T). Shaded region is the molecular mass range of 99.9% of non-interacting protein species comprising the mammalian proteome, with notations indicating G-actin (42 kDa, solid green line) and average F-actin (~2700 kDa, dashed green line) molecular masses. (b) False-color fluorescence micrographs and corresponding intensity profiles during electrophoresis (30 V cm^{-1}) of MDA-MB-231 GFP-actin single-cell lysates in F-actin stabilization buffer; 76 ± 3% of the fluorescence remains in the microwell (n = 4, error is standard deviation). Microwell outlined with dashed line in the micrograph and intensity

profile. (c) Intensity profiles (top) and false-color fluorescence micrographs of single RFP-Lifeact U2OS cells in microwells (dashed outline; only F-actin is fluorescent) upon lysis in F-actin stabilization buffer. PAGE results in retention of F-actin complexes in the microwell (repeated for a total of n = 3 cells). (d) Left: schematic of heating in the fractionation gel (gray) and gel lid (yellow) upon applying a current. Right: plot of temperature as function of elapsed PAGE time under the F-actin stabilization lysis buffer gel lid at 30 V cm^{-1} (n = 3; black diamonds).

We further validate SIFTER maintains F-actin complexes during fractionation without PAGE-induced temperature rise that may depolymerize or dissociate protein complexes (e.g., as shown in vitro or in certain cell types above 45 °C[46–48]). Electrical current passing through conductive buffer produces heat (Joule heating) during PAGE, which can increase temperature if not efficiently dissipated. The temperature difference, ΔT, between the surrounding medium and the conductor varies along the height axis, z, of the conductor:

$$\Delta T = E^2 \sigma_c \left(\frac{a^2 - z^2}{2k}\right) \quad (3)$$

where E is the electric field strength (V m^{-1}), σ_c is the buffer conductivity (S m^{-1}), $2a$ is the height and k is the thermal conductivity of the conductor (W m^{-1} K^{-1})[49]. Due to large temperature rises during electrophoresis in F-actin stabilization buffers containing $MgCl_2$ (σ_c ~1.3 mS cm^{-1}), E is limited to ~2-10 V cm^{-1} for 120-480 min in native slab gels[50], or ~18 V cm^{-1} in capillaries[50]. In SIFTER, the anticipated ΔT at 30 V cm^{-1} is ~0.02 °C (2a ~ .54 mm) *vs*. ~6.18 °C increase in a slab gel (2a ~ 5 mm; **Figure 2.6**). Indeed, we measure constant room temperature using liquid crystal temperature sensors under the hydrogel lid during PAGE at 30 V cm^{-1} with SIFTER (**Figure 2.5d**). Thus, we confirm SIFTER maintains endogenous protein complexes without Joule heating with ~100× faster fractionation than in a slab gel, 100-1000× higher sample throughput than a capillary (or comparable to automated capillary systems[51]), and without purifying, labeling or crosslinking of complexes[52].

We sought to validate SIFTER's quantification of single-cell heterogeneity of F-actin complex levels as quantitative assessment is needed for screening drugs targeting metastatic cell subpopulations[53]. In conventional imaging of F-actin with phalloidin (conjugated to a fluorophore), two factors pose a challenge to quantifying F-actin complex heterogeneity. First, phalloidin competes with, or is dissociated from, F-actin by both actin-binding proteins (e.g., cofilin)[22,23] and drugs (e.g., actin nucleating drug jasplakinolide, Jpk[24] and the structurally similar MiuA[54]). The number of potential actin-targeting drugs that compete with phalloidin are unknown. Nevertheless, Jpk and MiuA highlight the fact that a decrease in phalloidin staining signal can be due to decreased F-actin expression, competitive binding, or a combination of the two. Second, optimal cell segmentation requires that cells are not in contact with one another[55], which limits quantification from tissues and high-throughput analysis[55]. The latter may be overcome in the case of actin by conducting analysis by flow cytometry. While flow cytometry is compatible with proximity ligation assay for two proximal proteins, the lack of antibodies specific for protein interactions prevents multi-component protein complex measurement by flow cytometry[56]. Alternatively, SIFTER is free from competitive binding, cell segmentation challenges, and can discern and quantify protein complexes.

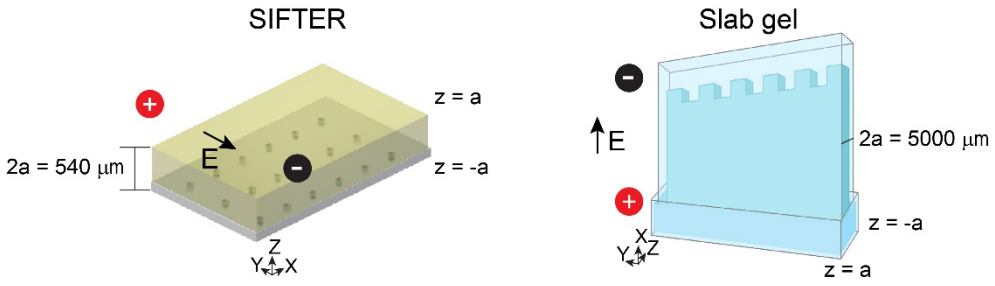

Figure 2.6: Schematic representations of SIFTER and a slab gel setup with parameters used for estimates of temperature difference. Temperature difference between the edge of the conductor and different z positions is given by[2]: $\Delta T = E^2 \sigma_c \left(\frac{a^2 - z^2}{2k}\right)$ where E is the electric field (V m^{-1}), σ_c is the electrical conductivity (S m^{-1}), 2a is the cross-sectional thickness, and k is the thermal conductivity (W m^{-1} K^{-1}). We neglect an additional term in the equation that accounts for heat transfer to a material incasing the conductor (thus we assume the width of the encasing material is zero). For E =3000 V m^{-1}, σ_c = 0.13 S m^{-1}, and approximating the conductor as water (given the high water volume fraction of polyacrylamide gel), k = 0.5918 we find ΔT=0.02 °K in SIFTER (at the fractionation gel or z = -0.00023), and ΔT = 6.18 °K in the slab gel (at the location of the sample in the slab gel, or z = 0). Slab gel schematic created with BioRender.com

With SIFTER, we investigated two well-studied drugs – Jpk and Latrunculin A (LatA) – each having a unique mechanism of action on actin[57,58] (**Figure 2.7**). Understanding Jpk effects on F-actin complexes is confounded by competitive binding with phalloidin and differing observations *in vivo* versus *in vitro*[58]., Jpk binds at the interface of three actin subunits[59] to lower the number of actin subunits needed for a stable multimer for filament elongation, causing disordered aggregates[58]. Still, F-actin complex levels increase in certain cell types with Jpk treatment in the 0.1 - 1.0 μM range as determined by bulk ultracentrifugation[60,61]. With phalloidin staining of Jpk-treated BJ fibroblasts, we qualitatively observe shorter filaments and small aggregates when dosing with 100 nM Jpk. While 100 nM Jpk is below the reported IC_{50} of 555 nM Jpk treatment for 4 hours in breast cancer cells[62], the concentration is high enough to induce decreased phalloidin fluorescence. When phalloidin stained Jpk-treated cells display decreased fluorescence signal, as with the BJ fibroblasts here, it is difficult to discern if competition with phalloidin obscures interpretation (**Figure 2.7a**). SIFTER yields a ~1.6× and 2.1× decrease in median F-actin relative to the control at the 100 and 200 nM Jpk concentrations, respectively (Kruskal-Wallis p-value < 0.0001 with Dunn-Sidak correction for multiple comparisons, **Figure 2.7b-c**). The decrease in F-actin levels from Jpk treatment is not accompanied by increasing G-actin immunoprobe signal. To assess heterogeneity in SIFTER F-actin complex levels across 100s-1000s of individual cells, we calculate the coefficient of quartile variation (*CQV*). The *CQV* is a metric of variance accounting for skewed distributions[63], such as gamma-distributed protein expression[64]:

$$CQV = \frac{Q_3 - Q_1}{Q_3 + Q_1} \qquad (4)$$

where Q_3 is the 75th percentile and Q_1 is the 25th percentile F-actin level. We find $CQV_{\text{DMSO control, BJ}}$ =0.38, $CQV_{\text{Jpk 100 nM, BJ}}$ =0.39 and $CQV_{\text{Jpk 200 nM, BJ}}$ = 0.39 (subscripts refer to the treatment and cell type). Similar *CQV* values with increasing drug concentration indicate the drug effect is relatively consistent across the cell population.

In contrast, LatA sequesters G-actin and reduces both F-actin complex levels and the F_{ratio}, as determined by phalloidin staining, DNAse I staining (of G-actin) and bulk methods[57,65,66], but variation in cell response is unknown. After treatment with 2 μM LatA, we phalloidin-stained U2OS cells and observed decreased F-actin complex fluorescence (**Figure 2.7a**) in agreement with previous findings[66]. As with Jpk, we utilized a high enough LatA drug concentration to induce visible changes in phalloidin fluorescence. To assess variation in cell response to LatA, we benchmarked the distribution of F-actin levels from LatA treatment in SIFTER versus flow cytometry of trypsinized, fixed, and phalloidin-stained U2OS cells. By flow cytometry, we find the median F-actin complex level of DMSO control cells is significantly higher than the LatA treatment median by 1.9× (Mann-Whitney P-value < 0.0001, **Figure 2.7d**, n = 9203 control cells and n = 5114 LatA-treated cells). With SIFTER, we observe the median F-actin complex level in DMSO control cells is significantly higher than the LatA treatment median by 1.5× (Mann-Whitney P-value < 0.0001, n = 911 control cells, and n = 444 LatA-treated cells, **Figure 2.7d-e**). We further found that SIFTER measured a significantly lower log fold change (i.e., smaller increase in DMSO control over LatA) than flow cytometry (Mann-Whitney P-value < 0.0001, **Figure 2.8**). For each of the two techniques, we converted the original data to the log scale, and normalized the LatA measurements by the mean and variance of the DMSO control. During normalization of the flow cytometry data set, sample size was accounted for by a repeated downsampling to match the sample size of SIFTER assay: we subsampled 444 points from 5114 flow cytometry LatA measurements and 911 points from 9203 flow cytometry DMSO control measurements. Next, we normalized the 444 subsampled LatA points, and repeated the subsampling and normalization protocol 100 times. The normalization procedure resulted in 444 SIFTER assay data points reflecting the log fold changes (DMSO control over LatA), and 44400 flow cytometry data points after pooling together the 100 subsamples. A Mann-Whitney test shows the normalized data in flow cytometry assay is significantly higher than for SIFTER assay, with a $p < 0.0001$ and 99% confidence interval of shift in locations being [0.6306, 0.9304]. This indicates that with a 99% high chance, the range [1.88, 2.54] will cover the ratio between the fold change in flow cytometry and the fold change in SIFTER measurement (DMSO control over LatA). Here 1.88=exp(0.6306), 2.54=exp(0.9304). The confidence interval suggests the fold change measured in flow cytometry assay is significantly higher. Thus, SIFTER does not measure as large a decrease in F-actin levels upon LatA treatment as flow cytometry of fixed and phalloidin-stained cells. One reason SIFTER may report smaller decreases in F-actin levels upon LatA treatment (while still maintaining statistical significance) is due to run-to-run variation observed across assay replicates (each replicate shown in **Figure 2.9**).

Unlike Jpk, LatA treatment corresponds with an increase in F-actin *CQV* as $CQV_{\text{LatA, U2OS}} = 0.49$ vs. $CQV_{\text{DMSO control, U2OS}} = 0.32$ by SIFTER (a 1.5× increase) and $CQV_{\text{LatA, U2OS}} = 0.30$ vs. $CQV_{\text{DMSO control, U2OS}} = 0.23$ by flow cytometry (a 1.3× increase). Previously, phalloidin staining revealed a single F-actin complex-phenotype from ~200 sparsely seeded cells treated with 250 nM LatA[67]. Here, the *CQV* increase upon LatA exposure suggests differential cell tolerance to LatA potentially due to the almost 10× higher LatA concentrations utilized here. Thus, SIFTER circumvents competitive binding or cell segmentation challenges to quantify variation in drug

effects on F-actin complexes at the single-cell level. The high $CQV_{\text{LatA, U2OS}}$ from SIFTER prompted us to further investigate cellular variation in response to LatA treatment. It is not currently possible to quantify the variation in the other cytoskeletal protein complexes, IF and MT with flow cytometry, as vimentin and tubulin antibodies would bind both the monomer and protein complexes in the cell. However, with SIFTER, co-detection of protein complexes within the same cell is possible, using antibodies raised against different species, or with a chemical stripping and re-probing approach developed previously[27].

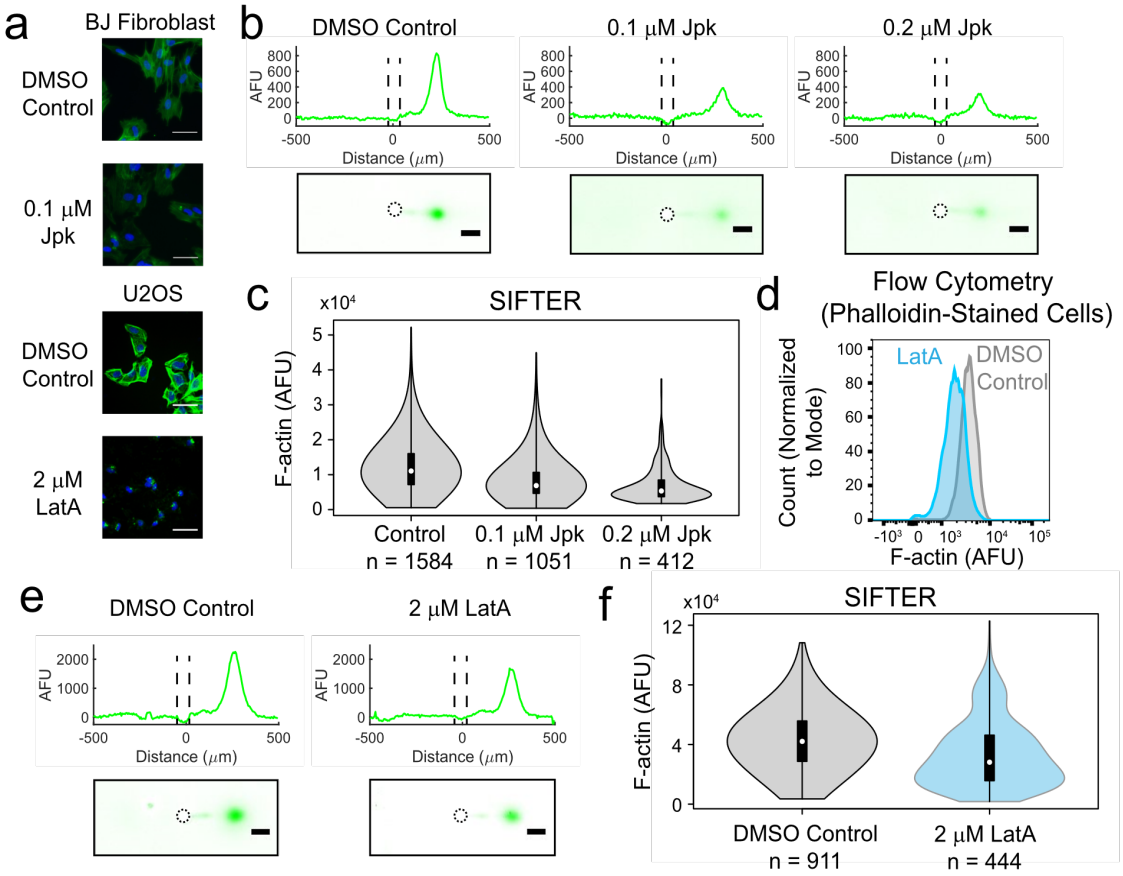

Figure 2.7: SIFTER quantifies cellular heterogeneity in F-actin complex levels, avoiding competitive binding or cell segmentation challenges encountered with phalloidin staining and capturing the cellular variation identified by flow cytometry. (a) False-color fluorescence micrographs of U2OS or BJ fibroblast cells fixed and stained with fluorescent phalloidin (F-actin, green) and Hoechst (nuclear stain, blue) after incubation with Latrunculin A (LatA, 60 min) or Jasplakinolide (Jpk, 120 min). Scale bar is 50 μm. Experiment was repeated for a total of at least two times. (b) False-color fluorescence micrographs and representative intensity profiles from SIFTER on single BJ fibroblast cells treated with the indicated concentration of Jpk. Scale bar is 100 μm. Microwell is outlined with a dashed line in the intensity profile and in the micrograph. (c) Violin plot of F-actin levels quantified from three different SIFTER devices with the indicated total number of single cells. Medians are 11053 for control, 6876 for 100 nM Jpk and 5343 for 200 nM Jpk. Boxplot box edges are at 25th and 75th percentile, middle point is the median, and whiskers extend to minimum and maximum values of the data set. Kruskal-Wallis p-value < 0.0001 with Dunn-Sidak correction

for multiple comparisons. (d) Histograms of F-actin fluorescence with cell count normalized to the mode from flow cytometry measurement of trypsinized and phalloidin-stained U2OS cells. Medians are 3454 for control (n = 9203, gray) and 1858 for LatA (n = 5114, blue). Mann-Whitney U Test p-value < 0.0001. (e) False-color fluorescence micrographs and representative intensity profiles from performing SIFTER on single U2OS cells. Scale bar is 100 μm. Microwell is outlined with a dashed line in the intensity profile and in the micrograph. (f) Violin plot of F-actin levels quantified from four different SIFTER devices with the indicated total number of single cells. Boxplot box edges are at 25th and 75th percentile, middle point is the median, and whiskers extend to minimum and maximum values of the data set. Medians are 42105 for control (n = 911, gray) and 28144 (n = 444, blue) for LatA. Mann-Whitney U test p-value < 0.0001.

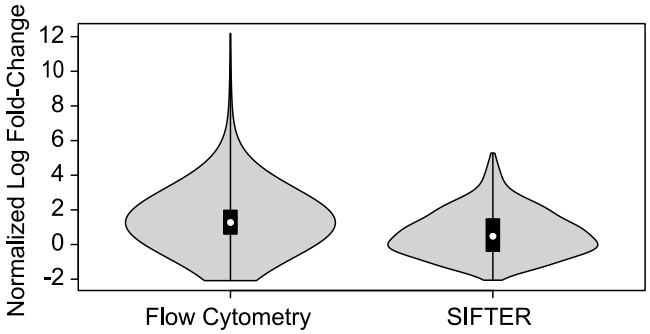

Figure 2.8: Violin plot of the normalized log fold-change distributions in F-actin levels from flow cytometry (of trypsinized, fixed and phalloidin-stained U2OS cells; n = 9203 DMSO control cells and n = 5114 Latrunculin A (LatA)-treated cells from one experiment) and SIFTER (n = 911 DMSO control cells and n = 444 LatA-treated cells from N = 4 SIFTER devices) from Figure 2.7. Boxplot box edges are at 25th and 75th percentile, middle point is the median, and whiskers extend to minimum and maximum values of the data set. Normalization of DMSO control data to LatA data and subsampling results in a distribution with 44000 data points for flow cytometry and 444 data points for SIFTER. Mann-Whitney p-value < 0.0001 and the 99% confidence interval for a shift in locations is [0.6306, 0.9304].

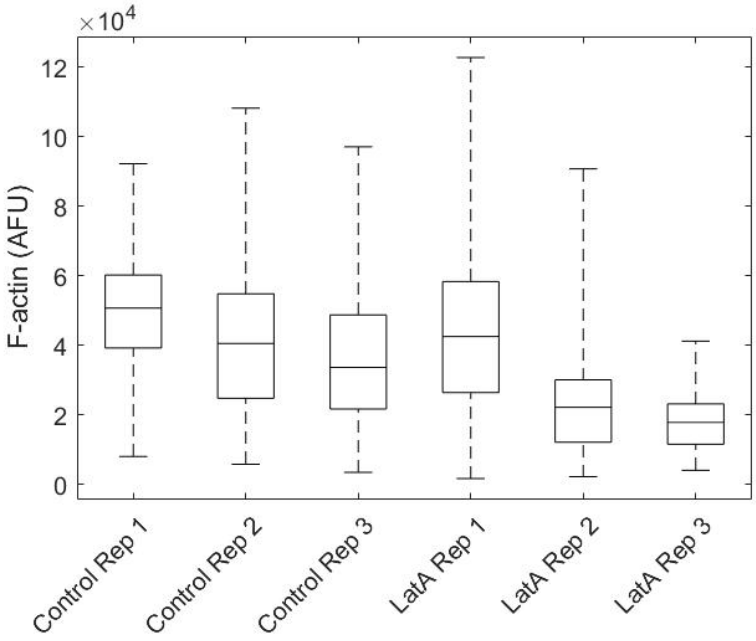

Figure 2.9: Boxplot of F-actin quantified from DMSO Control and Latrunculin A (LatA) replicates (Rep) comprising Figure 2.7F. Kruskal-Wallis p-value < 0.005 for Control Rep 1-3 (n = 286, n = 287 and n = 338, respectively), and for LatA Rep 1-3 (n = 237, n = 97 and n = 110, respectively). Medians for Control Rep 1-3 are: 50749, 40601, and 33728, respectively. The DMSO Control mean median is 41693, and mean median coefficient of variation (CV) = 21%. Medians for LatA Rep 1-3 are: 42581, 22255 and 17885, respectively. The LatA mean median is 27573 and mean median CV = 48%. Boxplot box edges are at 25th and 75th percentile, middle line is the median, and whiskers extend to minimum and maximum values of the data set.

Multiplexed SIFTER uncovers subpopulations of LatA-treated cells

We asked two questions regarding Latrunculin A-induced cellular variation, recognizing that SIFTER could permit measurement of all three major cytoskeletal protein complexes simultaneously. First, we sought to understand if LatA yields differential expression of other cytoskeletal protein complexes. Second, we asked whether LatA induced unique cell subpopulations. The cytoskeletal protein complexes F-actin, microtubules (MT, of α- and β-tubulin subunits), and intermediate filaments (IF, of vimentin or keratin subunits) have both redundant and distinct functions in maintaining cytoskeletal integrity (**Figure 2.10a**). Such redundancy[68] yields increased IF to counteract F-actin destabilization of mesenchymal cells[69] with only 1-h treatment with another Latrunculin, LatB. The counteracting increase in intermediate filament levels occurs because keratin intermediate filament-regulating genes become differentially expressed[69]. Yet, quantification of cytoskeletal changes remains a challenge in single cells by microscopy due to segmentation artifacts and low signal-to-noise ratio from immunohistochemistry and phalloidin staining[70,71].

To understand concerted effects of 1-h LatA drug treatment on F-actin, MT, and IF, we performed same-cell, target-multiplexed SIFTER (**Figure 2.10b** and **Figure 2.11**). We assess the expression relationships between the three protein complexes in the DMSO vehicle control cells (n = 201 single cells) by Spearman rank correlation, and obtain $\rho = 0.70$ for MT vs. F-actin, $\rho = 0.72$ for F-

actin vs. IF, and ρ = 0.59 for MT vs. IF (**Figure 2.12**; $p < 0.0001$ for each correlation). The correlation values suggest coordination of cytoskeletal protein-complex levels across a large proportion of cells. A follow-up agglomerative hierarchical clustering analysis reveals sets of cells with distinct patterns of protein-complex expression (e.g., groups A-D, **Figure 2.10c**).

Next, to elucidate whether any of the potential subpopulations shown in **Figure 2.10c** (e.g., groups A-D) were unique to the LatA-treatment, we adapted the GeneFishing method[72] for CellFishing. Using a group of co-expressed cells as bait, we attempt to fish out other cells from a candidate pool that present a similar protein complex-expression pattern to that of the bait cells. We do this through a semi-supervised clustering approach, coupled with sub-sampling to ensure robust discoveries. Here, groups of LatA-treated cells from hierarchical clustering that appear as unique phenotypes each define a set of bait cells, and the DMSO control cells define the candidate pool. If a group of bait cells does not identify any cells with similar phenotypes in the DMSO control cells, we assume the phenotype is unique to the LatA-treated cell population. We found that bait group A does not fish out DMSO control cells, while groups B-D are examples of baits that do (**Figure 2.10d**). Groups B (~3% of LatA cells), C (~4% of LatA cells) and D (~3% of LatA cells) all fish out DMSO control cells (~0.5%, 2% and 20% of the DMSO control cells, respectively) and thus represent phenotypes not exclusive to LatA treatment. Group B is marked by elevated MT and to a lesser extent, elevated IF compared to the average protein complex expression levels of the LatA-treated cells. Group C is characterized by increased IF. Group D expresses low F-actin, MT, and IF, which was a phenotype observed in a substantial number of both control and LatA cells as displayed in the heat map. Group A (~2% of LatA-treated cells) is characterized by elevated MT in response to F-actin destabilization and is only found in the LatA treatment cells. If MT compensates for F-actin perturbation in subpopulations of cells, such cells may be better equipped to maintain cytoskeletal integrity in response to stress. LatA causes an increase in the percentage of serum-starved fibroblasts expressing mature microtubules (from 40% to 70% of cells after one hour at 0.1 μM)[73], a shift between two cell populations. Here, hierarchical clustering of multiplexed SIFTER reveals distinct subpopulations with unique cytoskeletal composition stratified by expression of all three complexes. For example, IF levels distinguish Groups A and B with similar MT and F-actin levels, **Figure 2.10c-d.** Our results open new questions such as whether increases in MT in LatA-treated cells correspond with changes in transcriptional or translational rates, and subunit stability or MT organization, which warrant further investigation.

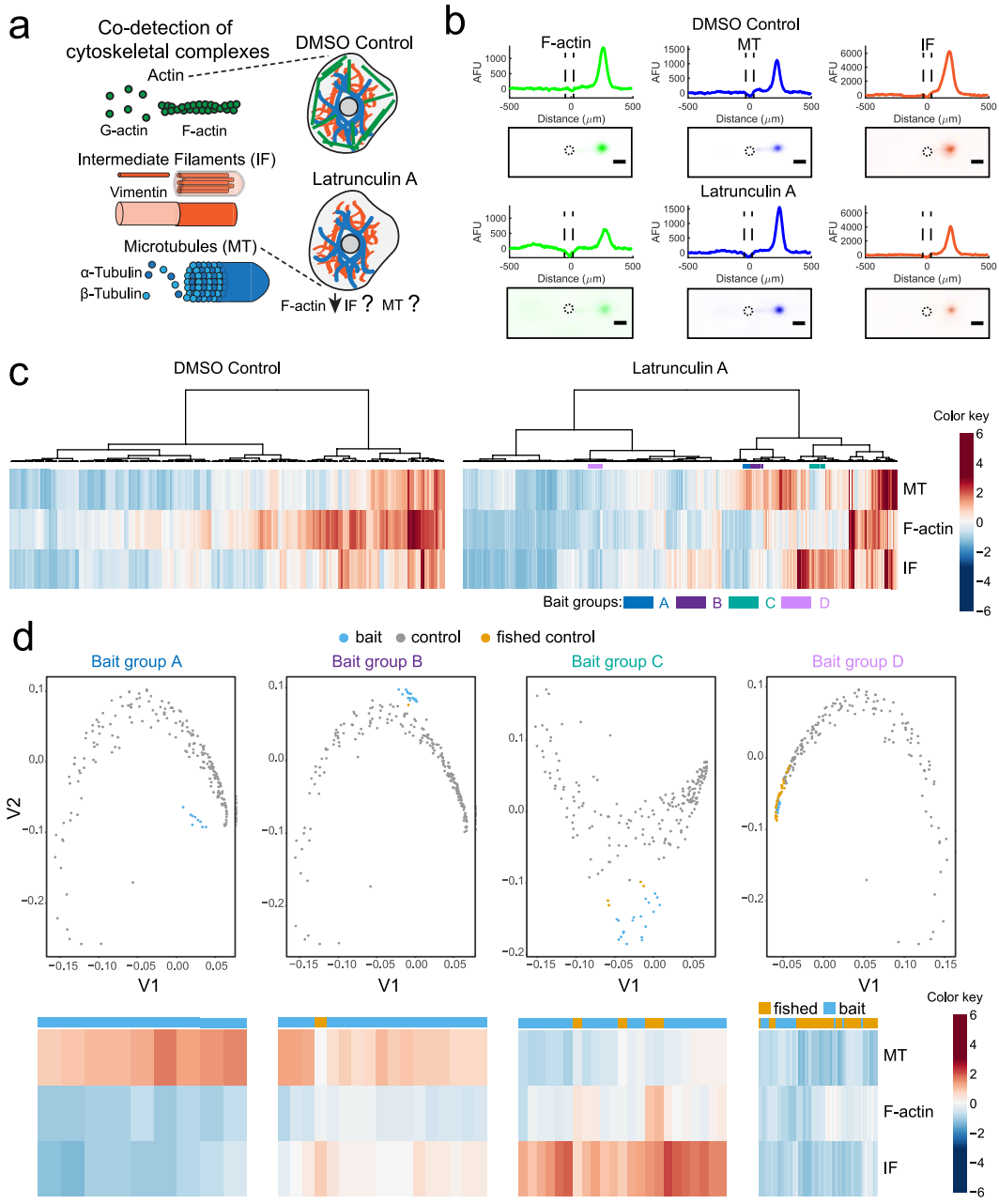

Figure 2.10: Multiplexed SIFTER detects subpopulations of cells with altered cytoskeletal protein complexes in response to F-actin destabilization. a) Schematic of the cell cytoskeleton composed of F-actin, intermediate filaments (IF) and microtubules (MT), and the unknown effects of Latrunculin A (LatA) on IF and MT. (b) Representative false-color fluorescence micrographs and intensity profiles from SIFTER. F-actin (green), MT (blue) and IF (orange) are electrophoresed to the right of the microwell. Protein quantification is performed by peak area integration. Scale bar is 100 μm. Microwell is outlined by a dashed line in the micrographs and intensity profiles. (c) Heat maps with dendrograms from agglomerative hierarchical clustering with Euclidean distance metric and Ward linkage for U2OS cells incubated in DMSO (n = 201 cells, three SIFTER devices) or 2 μM Latrunculin A (LatA, n = 507 cells, four SIFTER devices). Distinct sub-lineages used as bait groups A-D for

CellFishing are shown with colored bars (blue, purple, teal and lavender, respectively). Heatmap is standardized by row (mean at 0, and color gradations at units of standard deviation). (d) Spectral clustering projections and heatmaps depicting LatA treatment bait group cells (blue), DMSO control cells (grey) and fished out DMSO control cells (yellow).

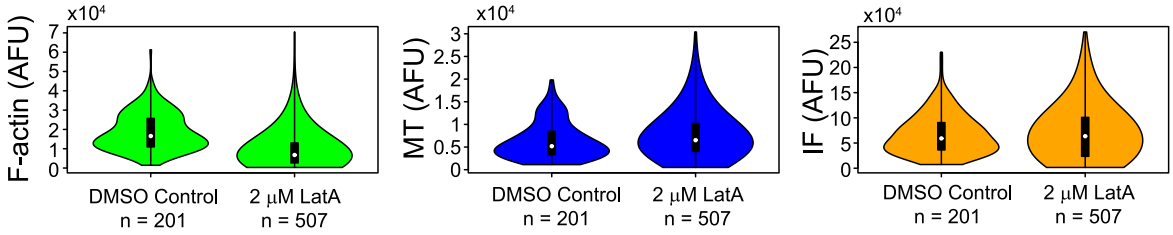

Figure 2.11: Violin plots of F-actin (green), microtubule (MT, blue) and intermediate filament (IF, orange) expression levels with DMSO control or 2 μM LatA treatment. Boxplot box edges are at 25th and 75th percentile, middle point is the median, and whiskers extend to minimum and maximum values of the data set. Mann-Whitney (two-sided test) p-value is significant (*) p-value < 0.0001 for F-actin (DMSO control median = 16573 and LatA median = 6765). Mann-Whitney p-value = 0.0027 for MT (DMSO control median = 5187 and LatA median = 6517). The Mann-Whitney p=0.8917 for IF (DMSO control median = 59137 and LatA median = 63607).

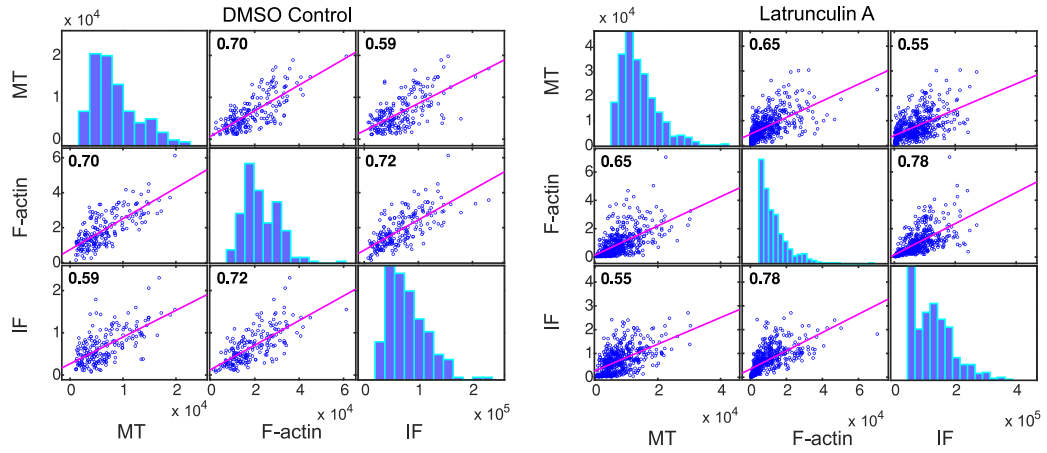

Figure 2.12: Correlation matrices for DMSO control (n = 201 cells) and Latrunculin A treated cells (n = 507 cells) with histograms (blue bars) and scatter plots (blue circles). Protein complexes detected are microtubules (MT), F-actin and intermediate filaments (IF). Spearman ρ are shown in the upper left-hand corner of each scatter plot (p-value < 0.0001 for all correlations). Least-squares reference lines are shown in magenta with the slope equivalent to the correlation coefficient.

Quantifying distributions of total actin and F_{ratio} across cells

To assess actin cellular heterogeneity, we asked: what are the statistical distributions of total actin and F_{ratio} across cells? In order to assess statistical distributions across SIFTER replicates, we needed to measure the cells at a fixed time after preparing the single-cell suspension, as detachment lowers the level of cytoskeletal protein complexes[74–76]. We conducted SIFTER replicates with constant cell handling times and measured the F_{ratio} from each device. The median F_{ratio} values from the three SIFTER replicates were 0.47, 0.42 and 0.46 (n = 275 n = 193 and n = 110 respectively, Kruskal-Wallis p-value = 0.0084; **Figure 2.13**), with a mean median of 0.45 and coefficient of variation of mean median of 5%. The interquartile ranges were 0.15, 0.13, and 0.08, which indicates the distributions overlap substantially with similar medians despite statistically significant run-to-run variation indicated by the p-value < 0.05. In each of three replicates displayed as quantile-quantile (QQ) plots, we found total actin largely follows a gamma distribution, as expected based on transcriptional bursting (**Figure 2.14**)[77]. One of the replicates deviates from the gamma distribution at the highest quantiles, indicating the tail behavior is less well-described by a gamma distribution. We find the F_{ratio} follows a normal distribution across cells by examining the QQ plots (**Figure 2.14**). The normal F_{ratio} distribution measured with SIFTER suggests actin binding proteins stochastically regulate actin polymerization/depolymerization.

Characterizing F_{ratio} requires accurate quantification of the G-actin fraction to calculate the total actin (the denominator of the ratio, F+G). As with any immunoassay, immunoreagents must be screened for each specific application, as sample preparation determines whether the epitope is native, partially denatured, or fully denatured[78] (**Table 2.2**). We found that in cells expressing endogenous (not GFP-fused) actin, some immunoreagents detected depolymerized F- but not G-actin (**Figure 2.15**). The performance of an antibody can vary for antigens under different assay conditions due to the changes in epitope accessibility. Antibodies recognize epitopes generally divided into two categories: linear epitopes and conformational epitopes[101, 102]. In applications where the protein target is denatured during sample preparation, linear epitopes are preferred. In applications where protein targets are present in their native state, conformational epitopes are preferred. In SIFTER, the G-actin subpopulation is immobilized twice: once in native conditions, and once in denaturing conditions. The resultant conformation, secured by the BPMAC-immobilization, can be hypothesized to be a combination of the linear and conformational form. The orientation of the immobilized protein will affect antibody affinity, similar to protein on solid supports in protein microarrays[103,104]. Future work involving the mixing of antibodies against linear and conformational epitopes[12] could potentially recover more G-actin peaks. Of note, a Fab fragment did yield G-actin immunoprobe signal in fibroblasts, while several full-length immunoreagents inconsistently detected G-actin in a subset of cells with F-actin signal. Lack of signal is not likely due to detection sensitivity, as actin is present at millions of copies of protein per cell[13] (while the in-gel immunoprobing limit-of-detection is ~27,000 copies of protein[27]). We instead hypothesize sterics may influence epitope availability. The Fab fragment may bind to native G-actin immobilized to the gel, whereas full-length antibody probes are unable to do so (~3× larger molecular mass). Future investigations will aim to establish a protocol for in-gel monomeric protein denaturation prior to immobilization to ensure the epitope availability is consistent between monomeric and depolymerized protein complex fractions immobilized in the gel.

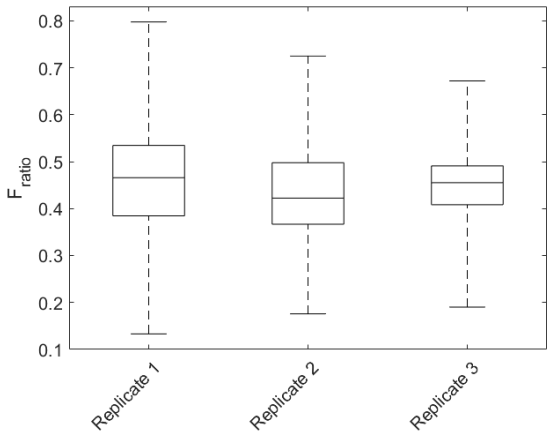

Figure 2.13: Boxplots of F-actin ratio for three SIFTER replicates performed on MDA-MB-231 GFP-actin cells (three different batches of cells with constant 10-minute settling time post-trypsinization performed on the same day). Boxplot box edges are at 25th and 75th percentile, middle line is the median, and whiskers extend to minimum and maximum values of the data set. Replicate 1: n = 275; replicate 2: n = 193; replicate 3: n = 110. Kruskal-Wallis p-value = 0.0084; Dunn-Sidak post-hoc test for multiple comparisons p-values not significant except p = 0.006 for Replicate 1 (median = 0.47) vs. Replicate 2 (median = 0.42).

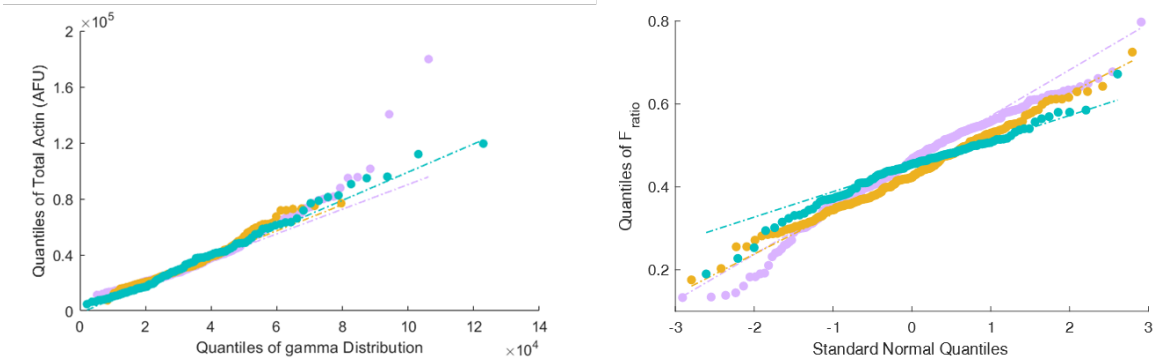

Figure 2.14: Quantile-Quantile (QQ) plots from replicates SIFTER assays in Figure 2.13. (a) Total actin (F+G) for each single cell versus a gamma distribution to each replicate (replicate 1: purple; replicate 2: orange; replicate 3: green). Single-cell total actin for each single cell is indicated with a circle symbol and dashed lines represent the fitted gamma probability density function ($f(x;\alpha,\beta) = \frac{x^{\alpha-1}e^{-\frac{x}{\beta}}}{\beta^{\alpha}(\alpha-1)!}$ for each replicate. Fit parameter α = 4.4, 6.9 and 2.2, and β = 8151, 4846, and 15361 for replicates 1, 2, and 3 respectively. (b) F-actin ratio (F_{ratio}) versus standard normal distribution.

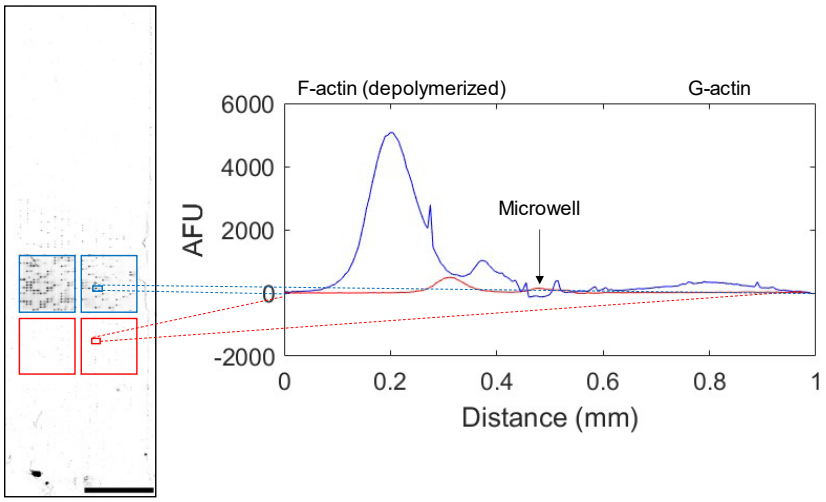

Figure 2.15: Gasket-based antibody screening for full SIFTER fractionation gels. Left: false-color fluorescence micrograph of fractionation gels (BJ fibroblast F and G-actin separations) immunoprobed with different actin antibodies (Abcam Ab200658, blue; Abcam Ab198991, red). Scale bar is 10 mm

Heat shock induces cellular heterogeneity in actin distribution

To assess how a non-chemical stress perturbs (1) the F_{ratio} distribution and (2) F- and G-actin coordination, we apply SIFTER to the study of heat shock. Cytoskeletal reorganization is a hallmark of disease states[5], and protein-complex dysfunction is prominent in aging[79] and during cellular stress[80,81]. Cell stress such as heat shock yields re-organization of F-actin in many, but not all cell types[82]. Indeed, with phalloidin staining, we observed a qualitative decrease in F-actin fluorescence of RFP-Lentiviral transformed MDA-MB-231 GFP-actin cells upon heat shock (**Figure 2.16a**).

For more nuanced characterization of the F_{ratio} distribution not possible with phalloidin staining, SIFTER reports the median F_{ratio} in the heat-shocked cells was similar to control cells (0.53 *vs.* 0.59, respectively; Mann-Whitney p-value < 0.0001, **Figure 2.16b-c**). However, the interquartile range of the F_{ratio} in heat-shocked cells is ~1.5× that of control cells (0.17 *vs.* 0.11). We quantified the skew of the distribution with the Pearson's moment coefficient of skew:

$$\overline{\mu_3} = \varepsilon\left[\left(\frac{X-\mu}{\sigma}\right)^3\right] \quad (5)$$

where ε is the expectation operator, X is the random variable (here, F_{ratio}), μ is the distribution mean and σ is the standard deviation. We find $\overline{\mu_3}$ is -0.40 for the control data set, and -0.38 for the heat-shocked cells (**Figure 2.16d**).

To understand if F- and G-actin levels remain coordinated upon heat shock, we quantified Spearman ρ (for F- and G-actin level correlation). The Spearman ρ decreased from 0.82 for the 49 control cells from one SIFTER device to 0.47 for 131 heat-shocked cells from two SIFTER devices. Across the two heat shock SIFTER devices, $\rho = 0.73$ for device 1 ($n = 22$, $p = 0.0002$) and $\rho = 0.41$ for device 2 ($n = 109$, $p < 0.0001$). We hypothesize heat shock SIFTER device 1 had too few cells that passed analysis quality control to capture the reduced correlation in F- and G-actin upon heat shock observed in device 2. We conclude that F-actin levels alone may not reveal actin cytoskeletal integrity: the Spearman ρ correlation of F- and G-actin also helps uncover differential stress response across the cell population.

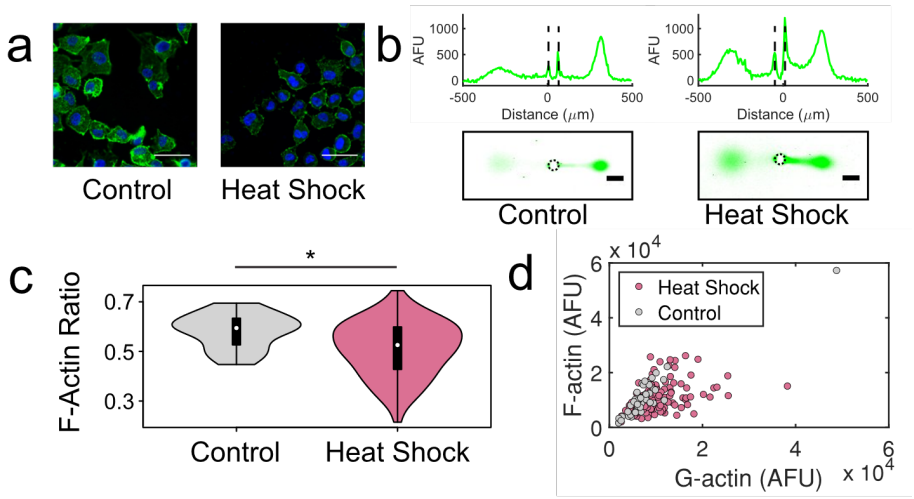

Figure 2.16: SIFTER quantifies actin distribution heterogeneity after heat-shock stress. (a) False-color fluorescence micrographs of adherent MDA-MB-231 GFP-actin cells with RFP-lentiviral transfection that were fixed and stained for F-actin (phalloidin, green) and the nucleus (Hoechst, blue) with heat shock (45 °C for 60 min) or 37 °C control. Scale bar is 50 μm. Experiment was repeated for a total of at least two times. (b) Representative false-color fluorescence micrographs and intensity profiles of GFP-actin PAGE fractionation from the specified single cells. Scale bar is 100 μm. Microwell is outlined by a dashed line in the intensity profiles and micrographs. (c) Violin plots of F-actin ratio (F/F+G) from SIFTER with $n = 49$ for the control (one SIFTER device, gray) and $n = 131$ for the heat shock condition (two SIFTER devices, pink). Median F_{ratio} is 0.59 for control and 0.53 for heat shock. Boxplot box edges are at 25th and 75th percentile, middle point is the median, and whiskers extend to minimum and maximum values of the data set. Mann-Whitney (two-sided test) p-value is significant (*) at $p < 0.0001$. (d) Scatter plot of F versus G-actin for control (gray circles) and heat shock (pink circles). Spearman $\rho = 0.82$ for control ($p < 0.0001$) and $\rho = 0.47$ for heat shock ($p < 0.0001$).

2.5: Discussion

SIFTER maintains multimeric cytoskeletal protein complexes during fractionation to reveal monomer versus protein-complex states in single cells. From perturbation of actin with well-characterized drugs, we find LatA, but not Jpk (at the concentrations tested), results in increased F-actin expression heterogeneity as characterized by increasing *CQV*. To investigate the heterogeneity of LatA-treated cells, we extended SIFTER to multiplexed readout of the three major cytoskeletal protein complexes (F-actin, microtubules, and intermediate filaments) simultaneously in each cell. We identified previously unknown cell subpopulations, such as the cluster with decreased F-actin and potentially compensatory increases in microtubules (Group A) along with intermediate filaments (Group B) upon LatA treatment. Thus, observed heterogeneity in LatA F-actin response corresponds with a spectrum of cytoskeletal integrity in the clonal population of U2OS cells investigated. While some cells increase expression of microtubules, intermediate filaments or both, other cells in the population undergo a complete cytoskeletal collapse. In the clonal population of U2OS osteosarcoma cells investigated here, the origins of differential maintenance of the cytoskeleton are unknown. However, recent single-cell sequencing studies of U2OS cells identified coordinated expression of sets of genes across subsets of cells, including some genes that regulate the cytoskeleton[83]. Determining if MT and IF-regulating genes are differentially expressed in subsets of U2OS cells and immunoprobing for the corresponding proteins along with F-actin, MT and IF in SIFTER could provide mechanistic insight. Partially coordinated regulation of the cytoskeleton raises two further questions: 1) what causes such differential gene expression to regulate the cytoskeleton in certain cells of a clonal population and 2) what is the functional implication of subsets of cells having a more resilient cytoskeleton? For the latter, we consider that the epithelial to mesenchymal transition of metastasis is marked by re-organization of the key cytoskeletal protein complexes[7], and osteosarcoma is known for aggressive metastasis. Consequently, it is intriguing to consider whether cell subpopulations with compensating overexpression of microtubules and intermediate filaments (marked capability to re-organize the cytoskeleton) represent a more mesenchymal-like subtype.

Applying SIFTER to single-cell F_{ratio} assessment, we determined that the F-actin ratio is normally distributed across a cell population. This indicates the possibility that the F-actin ratio could be a metric for assessing whether a population of cells is at an equilibrium state in terms of actin distribution. To investigate a non-chemical stress, we evaluated the impact of heat shock on the F-actin ratio of cells. Though missed by phalloidin staining, SIFTER uncovers potentially marked decrease in the correlation of F- and G-actin upon heat shock. Our results present the possibility that SIFTER presents a more nuanced assessment of actin cytoskeletal integrity than phalloidin staining.

Cellular stresses, be they chemical, heat shock, hypoxia, or oxidative stress, are critical features of cancer biology. Understanding which protein complexes are differentially expressed in drug susceptible versus drug resistant cells, or in subsets of cells that metastasize will be critical to advancing cancer therapies. Thus, SIFTER unlocks the capability to assess single-cell heterogeneity in expression of multimeric protein complexes, with broad applications across biology, potentially including protein complexes unrelated to the cytoskeleton.

The SIFTER assay presently is conducted with a well-characterized F-actin stabilization buffer for cell lysis and maintenance of cytoskeletal protein complexes during electrophoresis. However, no single buffer is ideal for stabilization of all protein complexes, prompting careful optimization of detergent, salt (ionic species and concentration), buffer and pH for immunoprecipitation of specific sets of protein complexes[84]. We have not yet investigated alternative lysis buffers for SIFTER, such as certain immunoprecipitation buffers (e.g., containing 10-100 mM NaCl or KCl). Higher buffer salt concentrations than the F-actin stabilization buffer will increase buffer conductivity and we hypothesize could yield more extensive Joule heating that can dissociate protein complexes. Fabrication of thinner (<500 μm) hydrogel lids for efficient heat dissipation may be needed for PAGE in high salt buffers. Thus, further device or buffer optimization may be required to apply SIFTER to protein complexes beyond the cytoskeletal complexes investigated here.

The range of detectable and separable protein-complex sizes is set by a tradeoff between fractionation and immunoprobing. Denser gels compromise assay detection sensitivity because size-exclusion based partitioning lowers the in-gel antibody probe concentration during the immunoassay[27]. Fractionation in decrosslinkable gel[85] should allow isolation of up to 100s of the known mammalian protein complexes with masses of ~295 kDa or greater in a 12%T gel (~7 or more protein subunits[86], assuming each subunit has the average mammalian protein size of 375 amino acids[87], or mass of ~40 kDa).

Another factor that determines which protein complexes are detectable with SIFTER is assay detection sensitivity. The cytoskeletal protein complexes investigated here are among the most abundant proteins in mammalian cells, often expressed at millions of copies[45]. Utilizing an in-gel immunoassay for readout, we have previously detected down to 27,000 copies of protein in a protein band[88]. As the SIFTER device is an open device design (vs. enclosed microchannels), protein is diffusively lost out of the microwell during cell lysis and out of the fractionation gel during electrophoresis. Such losses typically require proteins to be expressed at median copy number levels for mammalian proteins to be detectable in single-cell western blotting. While diffusive losses during SIFTER electrophoresis will be lower than in single-cell western blotting owing to efficient heat dissipation, protein fractionation inherently splits the amount of protein to be detected into the monomer and protein complex fractions. Thus, SIFTER likely requires proteins to be expressed above median copy numbers for detection.

One major advantage of SIFTER over existing assays for protein complexes[89], such as FRET or proximity labeling, is that SIFTER measures endogenous proteins without requiring cell modifications. Thus, we anticipate SIFTER will be valuable in the measurement of protein complexes from clinical specimens. For example, our group previously introduced isolated circulating tumor cells into a microwell array single-cell western blot device for protein profiling[37]. Circulating tumor cells are known to metastasize. With SIFTER, it would be informative to identify differentially expressed cytoskeletal protein complexes from circulating tumor cells to understand which protein complexes could be targets for small molecular inhibitors towards prevention of metastasis.

For time-sensitive cytoskeletal re-organization or mechano-sensitive protein complexes within the cytoskeleton (e.g., stress fibers and focal adhesions), the fractionation gel functionality can be extended to also serve as a cell culture extracellular matrix. On-chip culture can assay

adherent cells without the perturbation of trypsinization[90]. We anticipate that SIFTER can aid in evaluating snapshots of dynamic processes while cells are still adherent, such as cytoskeletal recovery from acute stress (e.g., heat shock, hypoxia, etc.). In the present study, we trypsinized and gravity settled heat-shocked cells for 10 minutes after the heat shock stress. The amount of time for cytoskeletal recovery from heat shock depends on the duration of the heat shock and cell type, as mouse fibroblasts only partially restore F-actin within 24 hours after 1 hour at 43 °C[82]. For shorter heat shock, or other stresses with faster recovery, growing and then stressing the cells on the SIFTER device will allow us to probe cytoskeletal protein-complex changes immediately after the stress, or at set times during the recovery. For mechano-sensitive cytoskeletal proteins, SIFTER may evaluate single-cell regulation of F-actin, MT, and IF in metastatic cancer cell subpopulations by quantifying dozens of cytoskeletal binding proteins with increased multiplexing by stripping and re-probing[88]. Looking ahead, SIFTER could assist drug screens targeting diverse protein interactions, and fundamental study of cellular stress responses underpinning invasive and heterogeneous cancer cells.

2.6: References

1. De Las Rivas, J. & Fontanillo, C. Protein–Protein Interactions Essentials: Key Concepts to Building and Analyzing Interactome Networks. *PLoS Comput. Biol.* **6**, e1000807 (2010).
2. Condeelis, J. How is actin polymerization nucleated in vivo? *Trends Cell Biol.* **11**, 288–293 (2001).
3. Wegner, A. Treadmilling of actin at physiological salt concentrations. *J. Mol. Biol.* **161**, 607–615 (1982).
4. Masai, J., Ishiwata, S. & Fujime, S. Dynamic light-scattering study on polymerization process of muscle actin. *Biophys. Chem.* **25**, 253–269 (1986).
5. Rao, K. M. K. & Cohen, H. J. Actin cytoskeletal network in aging and cancer. *Mutat. Res.* **256**, 139–148 (1991).
6. Senderowicz, A. M. *et al.* Jasplakinolide's inhibition of the growth of prostate carcinoma cells in vitro with disruption of the actin cytoskeleton. *J. Natl. Cancer Inst.* **87**, 46–51 (1995).
7. Ong, M. S. *et al.* Cytoskeletal proteins in cancer and intracellular stress: A therapeutic perspective. *Cancers (Basel).* **12**, 1–24 (2020).
8. Yuan, B. *et al.* FOXM1 contributes to taxane resistance by regulating UHRF1-controlled cancer cell stemness. *Cell Death Dis.* **9**, (2018).
9. Budnik, B., Levy, E., Harmange, G. & Slavov, N. SCoPE-MS: Mass spectrometry of single mammalian cells quantifies proteome heterogeneity during cell differentiation. *Genome Biol.* **19**, 1–12 (2018).
10. Zhu, Y. *et al.* Nanodroplet processing platform for deep and quantitative proteome profiling of 10 – 100 mammalian cells. *Nat. Commun.* **9**, 882 (2018).
11. Cong, Y. *et al.* Ultrasensitive single-cell proteomics workflow identifies >1000 protein groups per mammalian cell. *Chem. Sci.* **12**, 1001–1006 (2021).
12. Donnelly, D. P. *et al.* Best practices and benchmarks for intact protein analysis for top-down mass spectrometry. *Nat. Methods* **16**, 587–594 (2019).
13. Zhou, M. *et al.* Sensitive Top-Down Proteomics Analysis of a Low Number of Mammalian Cells Using a Nanodroplet Sample Processing Platform. *Anal. Chem.* **92**, 7087–7095 (2020).

14. Leuchowius, K. J., Weibrecht, I., Landegren, U., Gedda, L. & Söderberg, O. Flow cytometric in situ proximity ligation analyses of protein interactions and post-translational modification of the epidermal growth factor receptor family. *Cytom. Part A* **75**, 833–839 (2009).
15. Söderberg, O. *et al.* Direct observation of individual endogenous protein complexes in situ by proximity ligation. *Nat. Methods* **3**, 995–1000 (2006).
16. Roy, R., Hohng, S. & Ha, T. A practical guide to single-molecule FRET. *Nat. Methods* **5**, 507–516 (2008).
17. Kamiyama, D. *et al.* Versatile protein tagging in cells with split fluorescent protein. *Nat. Commun.* **7**, 11046 (2016).
18. Melak, M., Plessner, M. & Grosse, R. Actin visualization at a glance. *J. Cell Sci.* **130**, 525–530 (2017).
19. Riedl, J. *et al.* Lifeact: a versatile marker to visualize F-actin. *Nat. Methods* **5**, 605–7 (2008).
20. Spracklen, A. J., Fagan, T. N., Lovander, K. E. & Tootle, T. L. The pros and cons of common actin labeling tools for visualizing actin dynamics during Drosophila oogenesis. *Dev. Biol.* **393**, 209–226 (2014).
21. Cooper, J. A. Effects of cytochalasin and phalloidin on actin. *J. Cell Biol.* **105**, 1473–1478 (1987).
22. Mcgough, A., Pope, B., Chiu, W. & Weeds, A. Cofilin Changes the Twist of F-Actin: Implications for Actin Filament Dynamics and Cellular Function. *J. Cell Biol.* **138**, 771–781 (1997).
23. dos Remedios, C. G. *et al.* Actin binding proteins: regulation of cytoskeletal microfilaments. *Physiol. Rev.* **83**, 433–73 (2003).
24. Bubb, M. R., Senderowicz, A. M., Sausville, E. A., Duncan, K. L. & Korn, E. D. Jasplakinolide, a cytotoxic natural product, induces actin polymerization and competitively inhibits the binding of phalloidin to F-actin. *J. Biol. Chem.* **269**, 14869–71 (1994).
25. Heacock, C. S. & Bamburg, J. R. The quantitation of G- and F-actin in cultured cells. *Anal. Biochem.* **135**, 22–36 (1983).
26. Yamauchi, K. A. & Herr, A. E. Subcellular western blotting of single cells. *Microsystems Nanoeng.* **3**, 16079 (2017).
27. Kang, C.-C. *et al.* Single cell–resolution western blotting. *Nat. Protoc.* **11**, 1508–1530 (2016).
28. Bray, D. *Cell Movements: From Molecules to Motility*. *Garland Science, 2nd Edition* (2000).
29. Shelden, E. & Wadsworth, P. Observation and quantification of individual microtubule behavior in vivo: Microtubule dynamics are cell-type specific. *J. Cell Biol.* **120**, 935–945 (1993).
30. Bayley, P.M., Sharma, S.K. and Martin, S. R. Microtubule Dynamics in Vitro. in *Microtubules, Modern Cell Biology* (ed. Lloyd, J. S. H. and C. W.) 111–137 (1994).
31. Hookway, C. *et al.* Microtubule-dependent transport and dynamics of vimentin intermediate filaments. *Mol. Biol. Cell* **26**, 1675–1686 (2015).
32. Herrmann, H. & Aebi, U. Intermediate filaments: Structure and assembly. *Cold Spring Harb. Perspect. Biol.* **8**, 1–22 (2016).
33. Cano, M. L., Lauffenburger, D. A. & Zigmond, S. H. Kinetic analysis of F-actin

depolymerization in polymorphonuclear leukocyte lysates indicates that chemoattractant stimulation increases actin filament number without altering the filament length distribution. *J. Cell Biol.* **115**, 677–687 (1991).
34. Bray, D. & Thomas, C. Unpolymerized actin in fibroblasts and brain. *J. Mol. Biol.* **105**, 527–544 (1976).
35. Ujfalusi-Pozsonyi, K. *et al.* The effects of detergents on the polymerization properties of actin. *Cytom. Part A* **77A**, 447–456 (2010).
36. Leaist, D. G. A moving-boundary technique for the measurement of diffusion in liquids. triton X-100 in water. *J. Solution Chem.* **20**, 187–197 (1991).
37. Sinkala, E. *et al.* Profiling protein expression in circulating tumour cells using microfluidic western blotting. *Nat. Commun.* **8**, 14622 (2017).
38. Heinz, L. S. *et al.* Strong fascin expression promotes metastasis independent of its F-actin bundling activity. *Oncotarget* **8**, 110077–110091 (2017).
39. Bao, M., Xie, J., Piruska, A. & Huck, W. T. S. 3D microniches reveal the importance of cell size and shape. *Nat. Commun.* **8**, 1–12 (2017).
40. Rodbard, D., Kapadiia, G. & Chrambach, A. Pore gradient electrophoresis. *Anal. Biochem.* **157**, 135–157 (1971).
41. Wittig, I., Beckhaus, T., Wumaier, Z., Karas, M. & Schägger, H. Mass estimation of native proteins by blue native electrophoresis: Principles and practical hints. *Mol. Cell. Proteomics* **9**, 2149–2161 (2010).
42. Kumari, A., Kesarwani, S., Javoor, M. G., Vinothkumar, K. R. & Sirajuddin, M. Structural insights into filament recognition by cellular actin markers. *EMBO J.* **e104006**, 1–13 (2020).
43. Pollard, T. D. & Cooper, J. A. Actin, a central player in cell shape and movement. *Science (80-.).* **326**, 1208–1212 (2009).
44. Cano, M. L., Cassimeris, L., Fechheimer, M. & Zigmond, S. H. Mechanisms Responsible for F-actin Stabilization after Lysis of Polymorphonuclear Leukocytes. *J. Cell Biol.* **116**, 1123–1134 (1992).
45. Li, J. J., Bickel, P. J. & Biggin, M. D. System wide analyses have underestimated protein abundances and the importance of transcription in mammals. *PeerJ* **2**, e270 (2014).
46. Turi, A. Lu, R.C. Lin, P.-C. Effect of heat on the microtubule disassembly and its relationship to body temperatures. *Biochem. Biophys. Res. Commun.* **100**, 584–590 (1981).
47. Wendel, H. & Dancker, P. Kinetics of actin depolymerization: influence of ions, temperature, age of F-actin, cytochalasin B and phalloidin. *Biochim. Biophys. Acta - Protein Struct. Mol. Enzymol.* **873**, 387–396 (1986).
48. Coss, R. A. & Linnemans, W. A. M. The effects of hyperthermia on the cytoskeleton: A review. *Int. J. Hyperth.* **12**, 173–196 (1996).
49. Cifuentes, A. & Poppe, H. Rectangular capillary electrophoresis: Some theoretical considerations. *Chromatographia* **39**, 391–404 (1994).
50. Borejdo, J. & Burlacu, S. Distribution of actin filament lengths and their orientation measured by gel electrophoresis in capillaries. *J. Muscle Res. Cell Motil.* **12**, 394–407 (1991).
51. Dickinson, A. J., Armistead, P. M. & Allbritton, N. L. Automated Capillary Electrophoresis System for Fast Single-Cell Analysis. *Anal. Chem.* **85**, 4797–4804 (2013).

52. Ouimet, C. M. *et al.* Protein cross-linking capillary electrophoresis at increased throughput for a range of protein-protein interactions. *Analyst* **143**, 1805–1812 (2018).
53. Fife, C. M., McCarroll, J. A. & Kavallaris, M. Movers and shakers: Cell cytoskeleton in cancer metastasis. *British Journal of Pharmacology* **171**, 5507–5523 (2014).
54. Wang, S. *et al.* Actin stabilizing compounds show specific biological effects due to their binding mode. *Sci. Rep.* **9**, 1–17 (2019).
55. Zonderland, J., Wieringa, P. & Moroni, L. A quantitative method to analyse F-actin distribution in cells. *MethodsX* **6**, 2562–2569 (2019).
56. Leuchowius, K. J., Weibrecht, I. & Söderberg, O. In situ proximity ligation assay for microscopy and flow cytometry. *Curr. Protoc. Cytom.* **56**, 9.36.1-9.36.15 (2011).
57. Coué, M., Brenner, S. L., Spector, I. & Korn, E. D. Inhibition of actin polymerization by latrunculin A. *FEBS Lett.* **213**, 316–318 (1987).
58. Bubb, M. R., Spector, I., Beyer, B. B. & Fosen, K. M. Effects of jasplakinolide on the kinetics of actin polymerization. An explanation for certain in vivo observations. *J. Biol. Chem.* **275**, 5163–5170 (2000).
59. Heidecker, M., Yan-Marriott, Y. & Marriott, G. Proximity Relationships and Structural Dynamics of the Phalloidin Binding Site of Actin Filaments in Solution and on Single Actin Filaments on Heavy Meromyosin. *Biochemistry* **34**, 11017–11025 (1995).
60. Diamond, M. I. *et al.* Subcellular localization and Ser-137 phosphorylation regulate tumor-suppressive activity of profilin-1. *J. Biol. Chem.* **290**, 9075–86 (2015).
61. Kiuchi, T., Nagai, T., Ohashi, K. & Mizuno, K. Measurements of spatiotemporal changes in G-actin concentration reveal its effect on stimulus-induced actin assembly and lamellipodium extension. *J. Cell Biol.* **193**, 365–80 (2011).
62. Ali, R. *et al.* Jasplakinolide Attenuates Cell Migration by Impeding Alpha - 1 - syntrophin Protein Phosphorylation in Breast Cancer Cells. *Protein J.* **40**, 234–244 (2021).
63. Bonett, D. G. Confidence interval for a coefficient of quartile variation. *Comput. Stat. Data Anal.* **50**, 2953–2957 (2006).
64. Taniguchi, Y. *et al.* Quantifying *E. coli* proteome and transcriptome with single-molecule sensitivity in single cells. *Science* **329**, 533–8 (2010).
65. Lyubchenko, T. a, Wurth, G. a & Zweifach, A. The actin cytoskeleton and cytotoxic T lymphocytes: evidence for multiple roles that could affect granule exocytosis-dependent target cell killing. *J. Physiol.* **547**, 835–847 (2003).
66. Vindin, H., Bischof, L., Gunning, P. & Stehn, J. Validation of an algorithm to quantify changes in actin cytoskeletal organization. *J. Biomol. Screen.* **19**, 354–368 (2014).
67. Bryce, N. S. *et al.* High-Content Imaging of Unbiased Chemical Perturbations Reveals that the Phenotypic Plasticity of the Actin Cytoskeleton Is Constrained. *Cell Syst.* **9**, 496–507 (2019).
68. Huber, F., Boire, A., López, M. P. & Koenderink, G. H. Cytoskeletal crosstalk: When three different personalities team up. *Curr. Opin. Cell Biol.* **32**, 39–47 (2015).
69. Chang, T. H. *et al.* The effects of actin cytoskeleton perturbation on keratin intermediate filament formation in mesenchymal stem/stromal cells. *Biomaterials* **35**, 3934–3944 (2014).
70. Sum, C. S. *et al.* Establishing a High-content Analysis Method for Tubulin Polymerization to Evaluate Both the Stabilizing and Destabilizing Activities of Compounds. *Curr. Chem. Genomics Transl. Med.* **8**, 16–26 (2014).

71. Xiao, X., Geyer, V. F., Bowne-Anderson, H., Howard, J. & Sbalzarini, I. F. Automatic optimal filament segmentation with sub-pixel accuracy using generalized linear models and B-spline level-sets. *Med. Image Anal.* **32**, 157–172 (2016).
72. Liu, K. *et al.* GeneFishing to reconstruct context specific portraits of biological processes. *Proc. Natl. Acad. Sci. U. S. A.* **116**, 18943–18950 (2019).
73. Bartolini, F., Ramalingam, N. & Gundersen, G. G. Actin-capping protein promotes microtubule stability by antagonizing the actin activity of mDia1. *Mol. Biol. Cell* **23**, 4032–4040 (2012).
74. Bereiter-Hahn, J., Luck, M., Miebach, T., Stelzer, H. K. & Voth, M. Spreading of trypsinized cells: Cytoskeletal dynamics and energy requirements. *J. Cell Sci.* **96**, 171–188 (1990).
75. Knowles, G. C. & McCulloch, C. A. Simultaneous localization and quantification of relative G and F actin content: optimization of fluorescence labeling methods. *J. Histochem. Cytochem.* **40**, 1605–12 (1992).
76. Clark, E. A., King, W. G., Brugge, J. S., Symons, M. & Hynes, R. O. Integrin-mediated signals regulated by members of the rho family of gtpases. *J. Cell Biol.* **142**, 573–586 (1998).
77. Cai, L., Friedman, N. & Xie, X. S. Stochastic protein expression in individual cells at the single molecule level. *Nature* **440**, 358–62 (2006).
78. Uhlen, M. *et al.* A proposal for validation of antibodies. *Nat. Methods* **13**, 823–827 (2016).
79. Lai, W. F. & Wong, W. T. Roles of the actin cytoskeleton in aging and age-associated diseases. *Ageing Res. Rev.* **58**, 101021 (2020).
80. Baird, N. A. *et al.* HSF-1-mediated cytoskeletal integrity determines thermotolerance and life span. *Science* **346**, 360–3 (2014).
81. Higuchi-Sanabria, R. *et al.* Spatial regulation of the actin cytoskeleton by HSF-1 during aging. *Mol. Biol. Cell* **29**, 2522–2527 (2018).
82. Gavrilova, L. P., Korpacheva, I. I., Semushina, S. G. & Yashin, V. A. Heat shock induces simultaneous rearrangements of all known cytoskeletal filaments in normal interphase fibroblasts. *Cell Tiss. Biol.* **7**, 54–63 (2013).
83. Chapman, A. A. R., Lee, D. F., Cai, W., Ma, W. & Li, X. Correlated Gene Modules Uncovered by Single-Cell Transcriptomics with High Detectability and Accuracy. *bioRxiv* 1–58 (2020).
84. Conlon, F. L. *et al.* Immunoisolation of protein complexes from Xenopus. *Methods Mol. Biol.* **917**, 369–390 (2012).
85. Duncombe, T. A. *et al.* Hydrogel Pore-Size Modulation for Enhanced Single-Cell Western Blotting. *Adv. Mater.* **28**, 327–334 (2016).
86. Drew, K. *et al.* Integration of over 9,000 mass spectrometry experiments builds a global map of human protein complexes. *Mol. Syst. Biol.* **13**, 1–21 (2017).
87. Brocchieri, L. & Karlin, S. Protein length in eukaryotic and prokaryotic proteomes. *Nucleic Acids Res.* **33**, 3390–3400 (2005).
88. Hughes, A. J. *et al.* Single-cell western blotting. *Nat Methods* **11**, 749–755 (2014).
89. Arter, W. E., Levin, A., Krainer, G. & Knowles, T. P. J. Microfluidic approaches for the analysis of protein–protein interactions in solution. *Biophys. Rev.* **12**, 575–585 (2020).
90. Zhang, Y., Naguro, I. & Herr, A. E. In Situ Single-Cell Western Blot on Adherent Cell Culture. *Angew. Chemie - Int. Ed.* **131**, 14067–14072 (2019).

91. Lee, J. P., Kassianidou, E., MacDonald, J. I., Francis, M. B. & Kumar, S. N-terminal specific conjugation of extracellular matrix proteins to 2-pyridinecarboxaldehyde functionalized polyacrylamide hydrogels. *Biomaterials* **102**, 268–276 (2016).
92. Zhang, X. *et al.* Actin Stabilization by Jasplakinolide Affects the Function of Bone Marrow-Derived Late Endothelial Progenitor Cells. *PLoS One* **7**, (2012).
93. Vlassakis, J., Hansen, L.L. & Herr, A.E. SIFTER: Electrophoretic complex fractionation protocol. *Prot. Exch.* https://doi.org/10.21203/rs.3.pex-1582/v1 (2021).
94. Cramer, L. P., Briggs, L. J. & Dawe, H. R. Use of fluorescently labelled deoxyribonuclease I to spatially measure G-actin levels in migrating and non-migrating cells. *Cell Motil. Cytoskeleton* **51**, 27–38 (2002).
95. Scrucca, L., Fop, M., Murphy, T. B. & Raftery, A. E. Mclust 5: Clustering, classification and density estimation using Gaussian finite mixture models. *R J.* **8**, 289–317 (2016).
96. Vlassakis, J. *et al.* Measuring expression heterogeneity of single-cell cytoskeletal protein complexes. *Github.* https://doi.org/10.5281/zenodo.5091209 (2021).
97. Caudron, N., Valiron, O., Usson, Y., Valiron, P. & Job, D. A reassessment of the factors affecting microtubule assembly and disassembly in vitro. *J. Mol. Biol.* **297**, 211–220 (2000).
98. Nöding, B., Herrmann, H. & Köster, S. Direct Observation of Subunit Exchange along Mature Vimentin Intermediate Filaments. *Biophys. J.* **107**, 2923–2931 (2014)
99. Battaglia, R. A., Kabiraj, P., Willcockson, H. H., Lian, M. & Snider, N. T. Isolation of intermediate filament proteins from multiple mouse tissues to study aging-associated post-translational modifications. *J. Vis. Exp.* **2017**, 1–8 (2017).
100. Fourest-Lieuvin, A. Purification of tubulin from limited volumes of cultured cells. *Protein Expr. Purif.* **45**, 183–190 (2006).
101. Forsström, B. *et al.* Dissecting antibodies with regards to linear and conformational epitopes. *PLoS One* **10**, e0121673 (2015).
102. Zhao, Y. & Chait, B. T. Protein Epitope Mapping By Mass Spectrometry. *Anal. Chem.* **66**, 3723–3726 (1994).
103. Wang, J. *et al.* A versatile protein microarray platform enabling antibody profiling against denatured proteins. *Proteomics - Clin. Appl.* **7**, 378–383 (2013).
104. Liu, Y. & Yu, J. Oriented immobilization of proteins on solid supports for use in biosensors and biochips: a review. *Microchim. Acta* **183**, 1–19 (2016).

Chapter 3: Single-cell measure of protein response to microenvironment stiffness with coupled PDMS-polyacrylamide layers

3.1: Abstract

Dysfunctional crosstalk between the cell and the microenvironment plays a significant role in the development of cancer. Yet, the link between environmental stiffness and resultant proteomic state of the cell is unclear. Here, we demonstrate an integrated assay to culture single cells on a tunable substrate for subsequent proteomic analysis of individual cells. We utilize a sandwich approach with two separate sides for the independent tuning of the mechanical stimulus and analytical components. PDMS layers of various crosslinker concentrations are demonstrated to promote cell adhesion and morphology changes across a range of substrate stiffnesses after ECM-protein decoration. We validate the use of the tunable substrate to investigate the effect of substrate stiffness on the global cytoskeletal protein response with multiplexed target detection by coupling the tunable substrate with the analytical power of the single-cell western blot. We develop a concurrent detection scheme for simultaneous quantification of >6 cytoskeletal proteins. With this platform, morphological information of single cells can be mapped to their proteomic state. This high-throughput, single-cell platform can recapitulate relevant biological ECM, critical to the accurate assessment of quantitative proteomic response.

3.2: Introduction

Cell-matrix interactions are important for various cellular processes including differentiation and transduction, cell behavior, development, and migration [1]. Cell adhesion to surrounding extracellular matrix (ECM) induces the generation of intracellular contraction forces and distinct gene expression that matches the mechanical properties of the environment [2], [3]. Increasing evidence suggest that appropriate substrate stiffness can give rise to specific cellular responses [4]. For example, osteocytes change their morphology and gene expression profile in response to mechanical changes in their environment [5]. Stem cell fate decision is influenced by the microenvironment in which they reside [6], [7]. Engineered cardiac tissue regulate mitochondrial function in response to ECM elasticity and tissue architecture [8], and the force and patterns of myocyte contraction and mechanical interactions are directly linked to the substate stiffness [9]–[11]. Furthermore, it has recently become clear that the dysfunctional crosstalk between the cell and its external microenvironment plays a significant role in the development of cancer [3], [12]–[14]. Yet, force sensing and cellular adaptation to the mechanical microenvironment is far from understood [15].

To interrogate the link between the stiffness of the extracellular matrix (ECM) and cell responses, new tools for precise interrogation and manipulation of this relationship are needed. Often, cells are evaluated *in vitro* on materials that are many orders of magnitude stiffer than biologically relevant, or the cells have been manipulated during sample preparation steps. To this end, microcontact printing is commonly used in combination with immunocytochemistry for mechanobiology research [16]. In this application, cells are adhered to polydimethylsiloxane (PDMS), common because of the material's optical transparency, flexibility, chemical non-toxicity, and bio-compatibility properties, and evaluated by immunofluorescence stains or

morphological characteristics [17] [18]. While PDMS can be functionalized with ECM proteins to mimic a biologically relevant interface, the use of fluorescently labeled antibodies limits the multiplexing capability to interrogate many biochemical targets [15], and the throughput of the method is constrained [19]. Alternative methods are often limited in throughput [20]. To understand how substrate stiffness changes influence cellular behavior, a high-throughput, single-cell method is needed. Single cell western blotting permits the highly multiplexed detection of protein targets but requires trypsinization and disruption of coordinated cells prior to introduction onto the chip [21].

Here, we introduce a two-layer chip for the short-term culture and end-point proteomic evaluation of single cells in a high-throughput platform. Integration of the single cell western blot in concert with on-chip culture allows the interrogation of >6 proteins from 10-100s of single cells in parallel [22]. A sandwich chip architecture permits the independent tuning of the extracellular microenvironment substrate and the separation matrix used for the sieving-based protein detection. One side consists of PDMS, which can be tuned to achieve varying substrate stiffnesses and enables mimicry of a cell's natural microenvironment. The other side consists of a polyacrylamide gel sieving matrix that forms the arrayed microwells and is used for the western blot analysis of proteins. Optimized pore size permits concurrent detection of multiple protein with the same secondary antibody based on calculated separation resolution. Overall, this method can be used to quantitatively evaluate relevant cytoskeletal proteins and their correlation to cellular morphology and substrate stiffnesses on a single-cell level. To show the wide-ranging potential of this method for future mechanobiology studies, we report on the formulation and testing of microdevices with elastic moduli of 'soft' and 'stiff' substrates, and validation of electrophoresis and size-based separation of protein targets. This high throughput platform allows for improved control of the cell culture microenvironment in conjunction with a precise, single-cell resolution proteomic assay.

3.3: Materials and methods

Chemicals: 40% T, 34% C acrylamide/bis-acrylamide (29:1) (#A7802), Tetramethyl ethylenediamine (TEMED, #T9281), N-N-N'-N'- ammonium persulfate (APS, A3678), (3-aminopropyl)trimethoxysilane (#281778), sodium deoxycholate (NaDOC, #D6750), sodium dodecyl sulfate (SDS, #L3771), Pluronic F-127 (#P2443), fibronectin bovine plasma (#F4759), bovine serum albumin (BSA, #A7030), Triton X-100 (#X100) and urea (#U5378) were acquired from Sigma Aldrich. Phosphate buffered saline (#45001−130) was purchased from VWR. Tris glycine (10X, #1610734) buffer was obtained from Bio-Rad Laboratories. N-[3-[(3-Benzoylphenyl)- formamido] propyl] methacrylamide (BPMAC) was synthesized by PharmAgra Laboratories. SU-8 3050 photoresist was purchased from MicroChem. Polydimethylsilozane (PDMS) Sylgard 184 was purchased from Dow Corning. Tris Buffered Saline with Tween 20 (TBST, #9997S) was procured from Cell Signaling Technology.

Rhodamine-fibronectin (Rh-FN, FNR01) was acquired from Cytoskeleton Inc. Information on used antibodies is provided in **Figure 3.1.**

Table 3.1: Primary antibodies validated for use in the PDMA-PAG device for the global evaluation of cytoskeletal state in single cells. Certain targets were validated with multiple antibodies and appear multiple times in the table. For host species, Rb = rabbit, and Ms = mouse.

Target	Size (kDa)	Product name	Manufacture	Host Species
Lamin A/C	60-70	MAB-636	Invitrogen	Ms
Actin	42	Ab200658	Abcam	Rb
B-tubulin	55	Ab6046	Abcam	Rb
Vimentin	57	AB8978	Abcam	Ms
Paxillin	68	AHO0492	Invitrogen	Ms
CD44	90	156-3C11	Cell Signaling Technology	Ms
Actinin	100	D6F6	Cell Signaling Technology	Rb
Vinculin	127	Ab219646	Abcam	Rb
Vinculin	127	E1E9V	Cell Signaling Technology	Rb

Fabrication of the microwell SU-8 master: The polyacrylamide microwell and microcontact printing molds were fabricated on 2-inch silicon wafers by spin-coating SU-8 3050 photoresist to generate features 40 um in height as described elsewhere [23]. In short, the wafer masters were created using standard SU-8 soft lithography with photomasks created in AutoCAD and printed onto Mylar positive masks (CAD/Art services). The mask includes 50 μm diameter wells spaced 500 μm apart with 1 mm separation lane. The microcontact printing mask is the same as the microwell mask. Wafers were coated with (3-aminopropyl)trimethoxysilane by vaporization of the silane solution in a vacuumed chamber for 30 minutes to prevent gel and PDMS sticking.

PDMS-coated substrates: PDMS substrates of varying rigidities were prepared by varying the mass ratio of elastomer base to curing agent of SYLGARD 184 PDMS [8], [24]. Here, mass ratios of 10:1, 20:1, and 40:1 were tested. To achieve a thin layer of PDMS on a glass slide backing, a standard spin coating method was used. First, microscope slides were cleaned with acetone for 15 minutes and dried with nitrogen steam. Slides were baked at 150C for 15 minutes prior to PDMS coating to dehydrate after cleaning. The silicone elastomer base was mixed with the curing agent at the various mass ratios, degassed for 1 hour under house vacuum, and spin coated at 4000 rpms for 1 minute (600 rpm/s acceleration) to obtain 50 μm thick PDMS layers as assessed by contact profilometer [25]. Crosslinking/curing of the elastomer was carried out at 60 C overnight. The PDMS stamps for microcontact printing were prepared by casting PDMS at a 10:1 ratio onto a silicon wafer with 40 um feature height. PDMS was cured at 80C for 2 hours. The stamps were peeled off the mold and rinsed in PBS thrice and dried with nitrogen stream. The mold is designed with round islands, defining the configuration that the fibroblasts will take.

Microcontact printing: To promote cell attachment with defined geometries, PDMS substrates were inked with fibronectin (FN) by stamp-off microcontact printing [26], [27]. Stamp-off PDMS stamps were cast on wafers identical to those used to generate the PAG, cleaned for 5 minutes in pure ethanol and rinsed in water before use. Stamps were used twice before discarding. PDMS substrates were inked with 20 μg/ml fibronectin (25% rhodamine-labeling) for 1 hour at room temperature. Protein solutions were prepared in PBS. Excess ink was

removed, and the stamp was washed and dried by nitrogen stream. Prior to stamp-off, the PDMS stamps were cleaned by UV Oxygen Cleaner for 7 minutes. Conformational contact was made between the PDMS stamp and the PDMS substrate, removing fibronectin from the substrate where contact is made. The PDMS substrate with the fibronectin islands was treated with a 0.2% w/v solution of pluronic F-127 in PBS for 1 hour at room temperature to prevent fibroblasts from attaching to non-FN-coated portions of the PDMS slide [28] [29].

Cell culture: All cell lines were authenticated by short tandem repeat profiling by the UC Berkeley Cell Culture facility and tested negative for mycoplasma. BJ fibroblast cell line were cultured in T25 flasks using DMEM-GlutaMAX medium (gibco, #10566-016) supplemented with 10% fetal bovine serum (Gemini, #100-106), 1% pen strep (gibco, #15140-122), and 1% MEM Non-Essential Amino Acids (gibco, #11140-050) until confluence reached 80%. MCF7-tGFP cell line were cultured in T25 flasks using RPMI medium supplemented with 10% fetal bovine serum and 1% pen strep. All cultures were maintained at 37C under humidified 5% CO2 atmosphere. Cells at 80% confluency were trypsinized with 0.05% trypsin-EDTA solution, centrifuged at 800 rpm for 3 minutes, resuspended in either fresh media or PBS and 200 uL solution introduced immediately onto a chip or PDMS substrate at a concentration of ~50,000 cells/mL to achieve single-cell settling onto the fibronectin islands. Cells adhered to the ECM pattern at 37 °C for 30 minutes and the chip was washed in 1X PBS thrice and submerged in fresh media in a 4-well plate. Cells were cultured on-chip overnight (12-18 hours). Limited cell proliferation on PDMS substrates decrease odds of cell division during overnight culture [30] and maintains single-cell samples in the microwells, while allowing for the recovery of receptor proteins. Cell spreading in microwells of BJ fibroblasts was visualized after transduction of a BacMAM GFP control (Invitrogen, #B10383), introduced at 200 MOI.

Protein separation: 2X RIPA-like **(**5% SDS, 2.5% NaDOC, 0.5% Triton X-100, and 1X Tris-glycine in distilled water) was supplemented with 6M urea as the bifunctional lysis and electrophoresis buffer. Polyacrylamide gels (8%T and 3.3% C with 3 mM BPMAC incorporated) were polymerized onto silanized glass microscope slides with SU-8 molds with micro posts as described elsewhere [23]. Extra thick wicking paper (Bio-Rad, #1703969, cut to 2 x 5 cm rectangles) and polyacrylamide gels were incubated in 2X RIPA + 6M urea buffer for 10 minutes before beginning the experiments.

For non-adherent cells, a second microwell polyacrylamide slides was used in place of the PDMS slide to constrain movement of the cells. For cells cultured on the PDMS substrate, the PDMS substrate was brought contact with a lysis buffer-containing polyacrylamide gel in the arrangement of a sandwich. The polyacrylamide gel was aligned with the PDMS slide containing cells and applied within a custom 3D-printed electrophoresis chamber. Wicking paper was placed on the flanks of the sandwich, and lead electrodes were placed onto the wicks. The cell lysis is initiated upon application of the polyacrylamide gel and proceeded for 20 seconds before the electric field was applied (50 V/cm, 150V). Proteins were blotted, or bound to the polyacrylamide gel, by UV-induced covalent immobilization to the BPMAC incorporated in the gel (100% power, 45 s). The sandwich was removed from the electrophoresis chamber and the sandwich separated: The PDMS substrate was discarded, and the polyacrylamide gel is washed for 1 hour in 1X TBST prior to immunoprobing.

Antibody probing and imaging: Immunoprobing was performed as previously described [31]. In short, gels were incubated with 25 uL of 1:10 dilution of the primary antibodies 2% BSA-TBST for 2 hours. Gels were washed 2 x for 30 minutes in 1X TBST. Secondary antibodies at 1:20 dilution in 2% BSA-TBST were applied for 1 hour, and the gel washing is repeated as after the primary incubation. Gels were dried in a nitrogen stream and imaged with a laser microarray scanner (Genepix 4300A, Molecular devices). For multiplexed analysis with the same antibody species, secondary antibody was used at a 1:10 dilution.

Images were analyzed as described elsewhere [32] using MATLAB R2022a. Summarized, images were segmented into intensity profiles for each separation lane (region of interest, ROI). Each intensity profile is fit to a gaussian and checked against quality control parameters ($R2 > 0.7$, $SNR > 3$) and user-based inspection. The area-under-the-curve is calculated on a background-subtracted profile to extract the protein abundance for each signal.

Fluorescence imaging of cells in microwells, lysis, and electrophoresis: Imaging of time-dependent processes was done via time-lapse epifluorescence microscope on an Olympus IX50 inverted epifluorescence microscope connected to a CCD camera (Photometrics Coolsnap HQ2) and controlled with Metamorph software (Molecular Devices). Imaging was performed with a 10 X magnification objective (Olympus UPlan FLN, NA 0.45) and 800 ms exposure with 1 s intervals for timelapse images.

AFM measurements: Samples of PDMS of various stiffnesses were prepared on glass slides as above. Atomic force microscope (AFM, NanoSurf CORE) was used to perform indentation measurements. AppNANO FORT probe (Pyramidal/Rectangular Silicon) was used, with nominal spring constant of 1.6 n/M and frequency of 61.0 kHz. For all stiffnesses, elastic moduli were determined from the unloading part of the curve [33]. The AtomicJ program was used to extract the Young's Modulus from the measured displacement curves [34]. Samples were indented in air with ~ 1100 indents at 10 different areas on the surface for each sample.

3.4: Results

Assay design principles

To boost the information content from mechanobiological assays, we coupled a tunable matrix with a polyacrylamide gel for proteomic measurement. The cell phenotype (shape, diameter, etc.) can be monitored during culture on a desired (and variable) stiffness substrate, with endpoint intracellular signaling state readout. We leveraged arrayed microscale design for parallel, single-cell analysis of 10s-100s of single cells (**Figure 3.1A**). The assay consists of two separate layers, that are brought together to form a closed system at the time of analysis. The substrate, made of PDMS, can be turned across a range of physiologically relevant stiffnesses. Cell growth and adhesion to the PDMS ECM is controlled by fibronectin islands patterned onto the PDMS by microcontact printing techniques (**Figure 3.1B**) [35]. Mechanochemical feedback for cell-ECM adhesion include the recruitment and activation of cytoskeleton-regulating proteins that in turn regulate force-generating machinery [36]. Focal adhesion contacts involving transmembrane adhesion proteins connect the cell and the substrate coated with ECM [36] (**Figure 3.1C).** Focal adhesion proteins form complexes with internal players such as paxillin and vinculin [37]. Vinculin has been shown to crosslinking several adhesion adapter proteins to the actin

cytoskeleton upon activation [38]. Through a range of signaling cascades, including the RhoA/ROCK pathway, extracellular signals are converted to intracellular signal, propagating to the cytoskeleton for morphological response to the stimulus, and to the nucleus for genetic programing response [39]–[41]. Thus, cell behavior and fate is controlled on the single-cell level by spatial, chemical and mechanical factors [42]. Single-cell resolution is necessary to detect rate subpopulations that diverge from normal cellular function upon mechanical stress.

On-chip culture coupled to a single-cell western blot style assay can elucidate the effect of mechanical cellular stressors on protein expression levels with single-cell resolution. The PDMS-polyacrylamide (PAG) device is used in five assay steps (**Figure 3.1D**). First, single cells are settled onto fibronectin islands patterned onto a tunable PDMS substrate [43]. Cells are cultured overnight to allow the formation of focal adhesions. The analytical layer consists of a micropatterned PAG cast on a microscope slide. The micropattern includes microwells to aid in the injection of protein into the polyacrylamide sieving matrix after lysis. At the time of analysis, the analytical layer is saturated with bifunctional lysis and electrophoresis buffer. The buffer-laden PAG is used first to deliver lysis buffer to the cultured cells, and then becomes the membrane in which proteins are first separated and then captured. Cells are lysed on-chip when the analytical layer and the substrate layer are combined into a closed system (lysis, 20 seconds). Polyacrylamide gel electrophoresis (PAGE, 45 seconds) is performed between the two layers. Proteins are immobilized (blotted) using a covalent reaction to benzophenone methacrylamide, incorporated into the gel backbone during production. Lastly, the two layers are separated, and the analytical layer is kept for in-gel immunoprobing. Specific antibodies are used to specifically detect proteins of interest within the gel. Here, BJ fibroblast were used. BJ fibroblast cell line has been shown to respond well to the mechanical stimulus of the substrates [44] [45], including actin organization [46][47], polarization [48]. The PDMS-PAG device can be imaged prior to cell lysis (**Figure 3.1E**) to extract cellular morphology information. This can be linked to proteomic data (**Figure 3.1F**) from the protein array. The planar array permits facile buffer introduction and sample handling for 10s to 100s of simultaneous single-cell measurements.

By decoupling the ECM and analytical layer, the stiffness properties of the former can be tuned without affecting the immunoprobing efficiency of the latter. This makes the platform widely applicable. The polyacrylamide pore size can be turned for optimal separation resolution of the proteins of interest. Larger proteins can be resolved with larger pore sizes, and smaller proteins can be resolved with smaller pore sizes. Gradient pore sizes as previously published could further increase the protein size dynamic range of this measurement technique [49]. Similarly, the size and geometry of the fibronectin islands can be altered by simple lithography techniques.

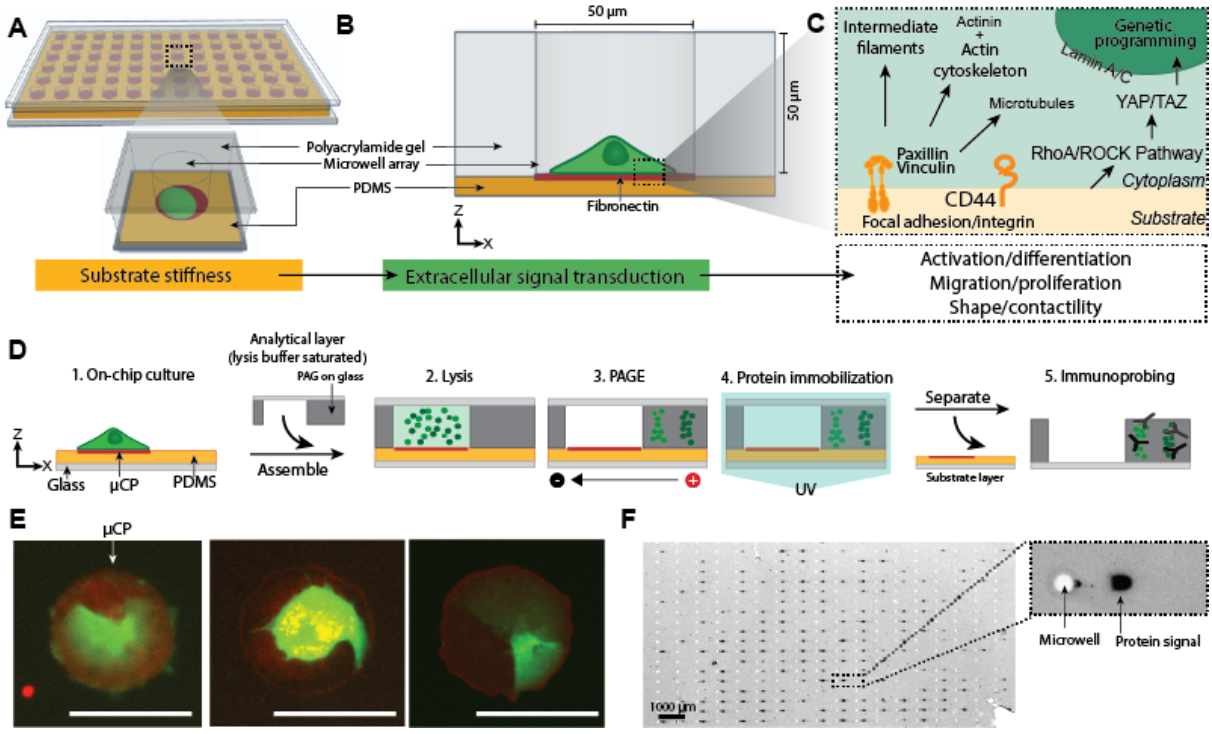

Figure 3.1: Single-cell, 2D culture for downstream multiplexed evaluation of cytoskeletal proteins with PDMS-PAG sandwich device. (A) Arrayed culture of cells on tunable PDMS substrates is combined with the analytical layer for single-cell proteomic evaluation. The two sides are brought into contact after cell culture for protein analysis of adherent cells. (**B**) Cross sectional schematic of a single cell. A cell is adhering to the PDMS via a fibronectin island. Once cultured, the microwell layer is added to ensure high local concentrations during the biological assay step. (**C**) Simplified diagram of key protein species implicated in mechano-sensing and cytoskeletal rearrangement. Conversion of extracellular to intracellular signal of substrate stiffness. Focal adhesion sites propagate ECM stiffness cues. Downstream activation and rearrangement of cytoskeletal proteins, the RhoA/ROCK pathway, and more aid in the propagation of signal. Substrate stiffness influences a range of cellular behavior, including activation, migration, and shape. **(D)** Assay workflow, starting with on-chip cell culture and ending with PAGE. Step 1: Cells are imaged to extract morphological information. Step 2: A bifunctional lysis and electrophoresis buffer is introduced by the addition of the analytical layer. Cells are lysed for 30 seconds. Step 3: an electric protein is applied for 45 seconds to drive polyacrylamide gel electrophoresis (PAGE). Step 4: Proteins are covalently immobilized in the polyacrylamide gel via UV-activation of benzophenone moiety. Step 5: Gels are washed and immunoprobed or targets of interest. Individual protein peaks are then quantified. (**E**) Representative false-color micrographs of adherent BJ fibroblast (green) after overnight culture (t = 16 hours) on fibronectin islands (red) prior to electrophoretic analysis. Scale bar = 50 µm. (**F**) Immunoassay results: Representative false-color micrograph of a subset of the arrayed chip and intensity profile of a single BJ Fibroblast cell highlighted. Gel was immunoprobed for β-tubulin after 30 seconds of lysis and 15 seconds of electrophoresis. Scale bar = 1000 µm.

Characterization of the PDMS substrate

Fibronectin-decorated PDMS permits cell adhesion and spreading for overnight culture. For this assay, cell confinement is also defined by the micropattern geometry [29], [50], [51]. The use of a flat PDMS substrate makes the PDMA-PAG device compatible with widely used microcontact printing methods. Compared to conventional microcontact printing, the stamp-off microcontact printing method produces sparce protein patterns (**Figure 3.2A**) [27]. A topographically flat stamp with microstructures is used to remove protein ink from a decorated surface, eliminating the risk of stamp collapse or feature deformation, even for patterns such as this with small, sparse features [52]. The stiffness of PDMS is a product of the component ratio, curing time, and curing temperature. By altering the base:curing agent ratio, PDMS can achieve a stiffness range from 88.56 ± 17.01 kPa (40:1, soft) to 2703 ± 313.7 kPa (10:1, stiff), as measured by AFM (**Figure 3.2B**). PDMS has been reported to have thickness-dependent mechanical properties, thought more pronounced at thicknesses much greater than those used here [53].

We evaluated the variation of stamp-off microcontact printing efficiency between stiff and soft PDMS substrates. The micropattern diameter, geometry and protein concentration was kept constant. Assuming perfect transfer of pattern, we would expect the area of fibronectin islands to be 1963.5 μm^2. We observed islands on the stiff substrate to be slightly larger than expected (mean = 2641 ± 204.8 $\mu m^{2,}$ n = 922), and islands on the soft substrate were comparable to expected size (mean =1906 ± 432.7 μm^2, n = 596). The soft substrate had greater standard deviations, suggesting greater island-to-island variation. Comparing the fluorescence intensity of the protein islands, we again observed statically significant differences between the two substates. Soft substrates has 140% fluorescence compared to the stiff substrate (2221 ± 761.8 AFU, n = 980 for stiff substrates; 3098 ± 1034 AFU, n = 557 for soft substrates). For stamp-off microcontact printing techniques, we hypothesized that the dictating factor to successful patterning is the conditions and surface properties of the substrate material. Here, the disparity in size and protein intensity showed differential protein adsorption and patterning fidelity across the two substrates. Differences in fluorescence intensity (corresponding to amount of fibronectin on the surface) can be corrected by increasing the initial concentration of fibronectin inked onto the substrate surface prior to stamp removal.

We show that coating the PDMS with the glycoprotein fibronectin allowed cell adhesion and differential morphologies depending on substrate stiffness. We assessed cell area of adhered cells after 16 hours of cultures (**Figure 3.2D**). It was found cells cultured on stiff substrates were significantly larger in area than those cultured on soft substrate. Cells cultured on stiff substrates often took on a size and shape matching the fibronectin islands. In comparison, cells cultured on soft substrates rarely exceeded more than half of the fibronectin island area. Our results and observed behavior of fibroblast on PDMS substrates cooperate previous finings of cells that attach on rigid substrates can extend more processes due to the increased focal adhesion complexes, whereas cells on softer matrices have weather interactions [54] [55].

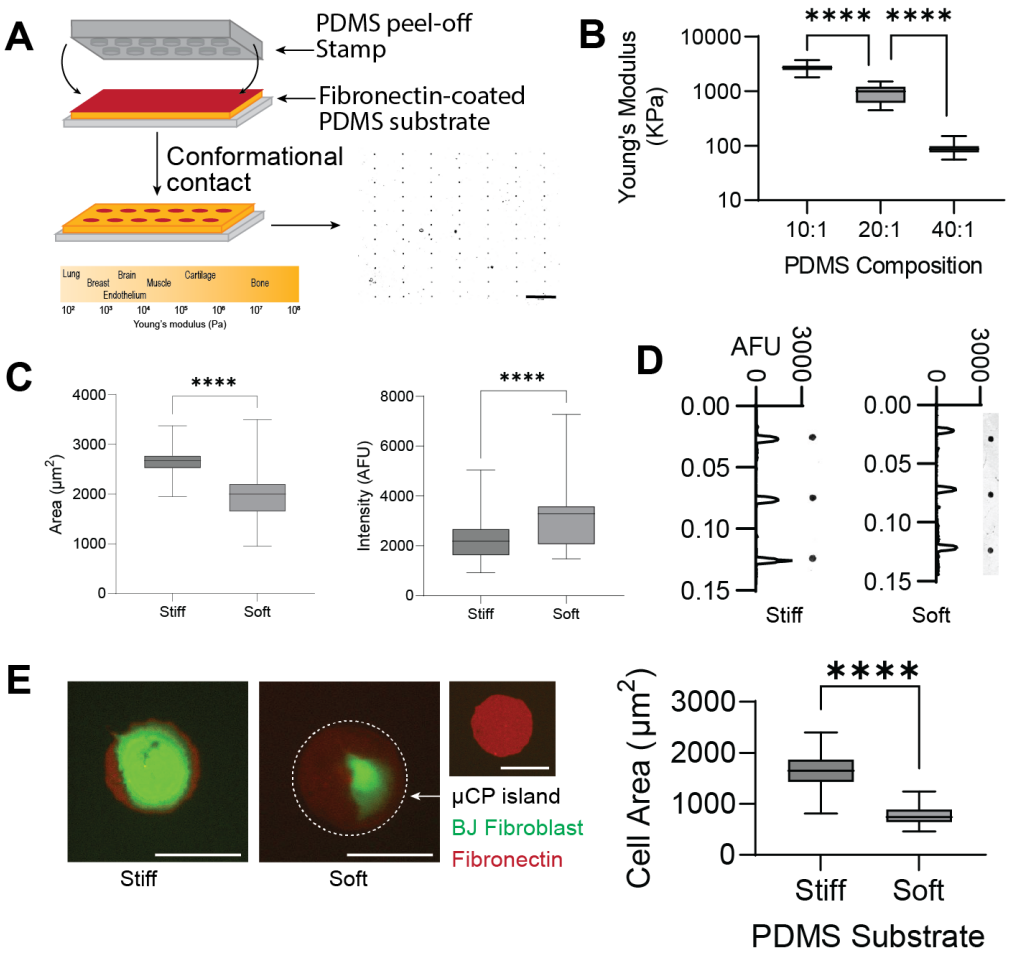

Figure 3.2: PDMS as the adhesive substrate layer for overnight culture. (A) Stamp-off microcontact printing (μCP) generates patterned protein islands by removing the fibronectin from non-pattern areas by a PDMS peel-off stamp. Conformational contact between the coated substrate and the stamp removes fibronectin from undesired areas, leaving μCP islands. Representative false-color micrograph of a subset of the arrayed 10:1 PDMS chip after patterning. Scale bar = 1 mm. **(B)** Increasing the fraction of PDMS base to curing agent correlates to a decrease in material stiffness as measured by AFM indentation (n = 1000, N = 3 devices). **(C)** Left, area of μCP islands for stiff (n = 1075) and soft (n = 601) PDMS substrates. Right, fluorescent intensity of the μCP islands for stiff (n = 1075) and soft (n = 601) PDMS substrates ($P < 0.0001$). Disparity in size and protein intensity shows differential protein adsorption and patterning fidelity across the substrate stiffness. **(D)** Representative fluorescence micrographs and corresponding intensity profile of protein pattern on stiff (left) and soft (right) substrates. **(E)** Cells cultured on stiff material take on a larger cell shape. Left, false-color representative micrographs of BJ fibroblasts cultured on stiff and soft substrates after 16-hour culture. Green = GPF transduction control, Red = fibronectin μCP island. Island highlighted with white dotted line. Scale bar = 50 μm. Right, area of cells cultured on stiff (n = 35) and soft (n = 41) substrates.

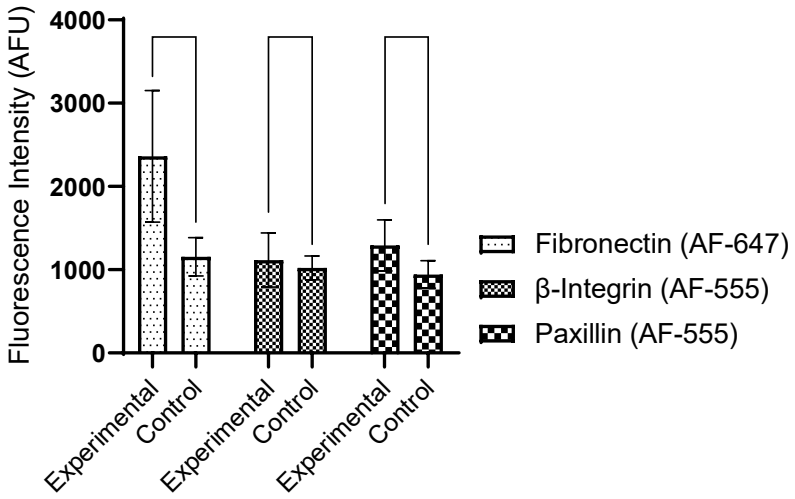

Figure 3.3: Prescence of focal adhesion proteins on fibronectin islands after cell culture and lysis. Experimental condition indicates fully fabricated devices that have been used for culturing and electrophoresis. The control condition indicates fully fabricated devices only. Separate devices were used for each protein species (graph shows pooled data across 2 devices for each condition). Legend indicates secondary antibodies Alexa Fluor (AF) conjugation. All pairwise t-tests $P < 0.0001$. $N > 250$ for all samples.

For accurate analysis of proteins during the analytical stage of the assay, all protein must be released from the cell upon lysis. Previously, integrin signal has been documented to stay at the site of focal adhesion formation and be excluded from electrophoretic injection [56]. We investigated the presence of focal adhesion proteins on the microcontact printed islands post-lysis. Residual protein would affect the quantitative analysis of those proteins based on their injection alone.

To quantify the amount focal adhesion proteins remaining at the site of cell culture, we compared the abundances of proteins in a control condition (micropatterned and blocked device) with the experimental condition (complete assay, including on-chip lysis and electrophoresis). All PDMS substrates were immunoprobed with either fibronectin and paxillin, or fibronectin and mouse anti-β-integrin (Abcam, ab30394). Each substrate was immunoprobed with 50 µL of solution. Primary antibodies were diluted to 1:10, and secondary antibodies to 1:20.

We found that the difference in fibronectin abundance is statistically significant ($P < 0.0001$) from the experimental condition to the control (**Figure 3.3**). Similarly, the difference in β-integrin and paxillin protein abundances between the control and experimental conditions are also statistically significant ($P<0.0001$). For these two proteins, the signal in the control case corresponds to passively absorbed protein onto the PDMS. No integrin or paxillin protein was present for these assays. Thus, when accounting for background adsorption, fibronectin has a two-fold increase in signal while integrin and paxillin have less than 10% difference. Based on this, detection of intracellular proteins, as opposed to those directly participating in cell-ECM anchoring, might be more suited for low abundance proteins.

Validation of electrophoresis in composite PDMS-PAG device

To avoid slippage between the two layers of the assay when combined in the 'sandwich' format, large liquid amounts were eliminated. Instead, a semi-dry approach was used during electrophoresis. Here, the analytical layer and substrate layers were brought together with alignment between the fibronectin islands and the microwells. Once in contact, the sandwich was placed between wicks previously soaked in lysis/electrophoresis buffer. Graphite electrodes were placed on top of the wicks to complete the circuit **(Figure 3.4A**). By limiting the fluid content of the system, we decreased the electrophoretic cross-sectional area. In turn, the heat dissipation is increased, and joule heating is decreased. This permits higher voltages during electrophoresis. The buffer-laden microwell gel provided the connection between the electrodes and the buffering ions for electrophoresis. The PAG carries ~ 50 uL of bifunctional lysis/EP buffer.

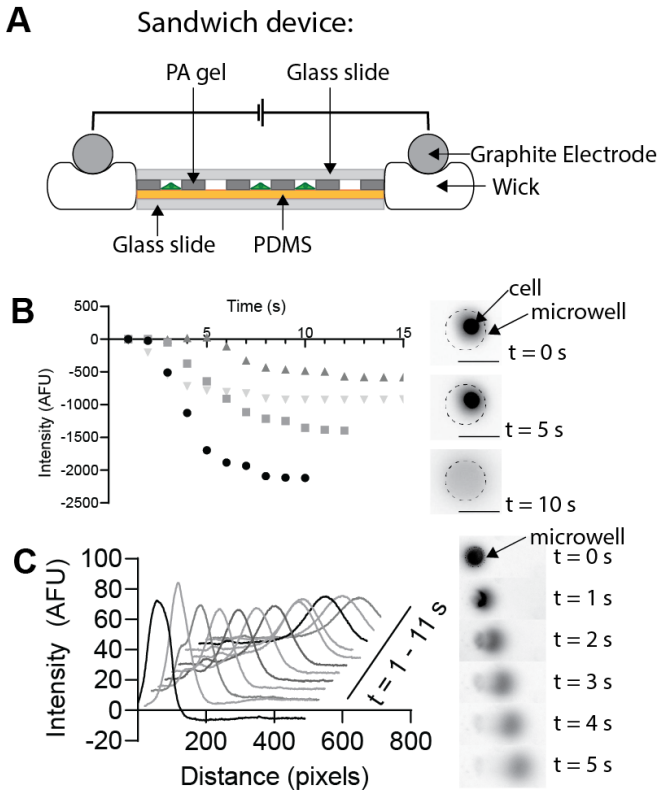

Figure 3.4: Enclosed sandwich device permits rapid lysis and electrophoresis. (A) Schematic of the closed, sandwich configuration. The analytical and substrate layers are sandwiched against each other such that the sandwich has glass on both exterior sides. Lysis-sodden wicks are placed adjacent to the sandwich for wick contact. **(B)** Lysis of fluorescent MCF7 GFP cell line with 2X RIPA buffer is complete within 10 seconds (n = 4), where t = 0 signifies when lysis buffer-laden microwell gel is applied atop of cells. Representative, false-color fluorescent micrographs show fluorescent cell content diffusing from cellular compartment into the microwell space for n = 4 cells. Fluorescence intensity is normalized to cell starting fluorescence. **(C)** Representative intensity profiles and micrographs of injection of fluorescent proteins from MCF7 GFP cells during initial stages of electrophoresis (E-field = 150 V).

Cell lysis and optimization of cell lysis duration was completed with MCF-7 GFP cells for easy monitoring. Cells were shown to lyse within 10 seconds of lysis introduction (**Figure 3.4B**). To validate injection of protein material in the semi-dry sandwich layout, we directly observed the injection of GFP-expressing protein material from MCF-7 cells. Within 10 s of PAGE, the fluorescent protein band completely injected 410 µm into the polyacrylamide gel (**Figure 3.4C**).

We compared the migration distances and peak shapes from the closed system with those from the open system as a means for characterization. Here, the open system consists of the gel layer only and sufficient lysis buffer to submerge the device [31]. Both systems were used to lyse and electrophorese BJ fibroblast cells. After UV-immobilization of protein, gels were immunoprobed with anti-actin antibodies. Electromigration in the closed system was reduced compared to the open system (**Figure 3.5A**) (distance = 137.6 ± 39.07 µm (n = 164) for closed system; distance = 565.4 ± 19.38 µm (n = 466) for open system). We hypothesize this is due to the limited ionic buffer capacity of the small lysis buffer volume. Upon adjustment of PAGE duration for comparable injection distance (20 s for the open system, 65 s for the closed system) (**Figure 3.5B-C**), differences in measured single-cell protein abundance for actin after immunoprobing were negligible (2.81e4 ± 1.88e4 (n = 96) for the closed system; 2.45e4 ± 1.04e4 AFUs (n = 252) for the open system. P = 0.023, unpaired T-Test). However, band-broadening factors were more dominant in the closed system.

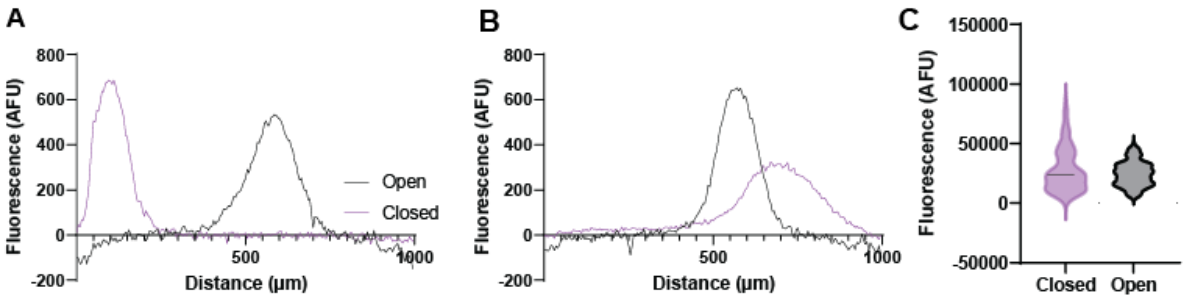

Figure 3.5: Closed sandwich electrophoresis results in comparable quantification of protein with slower migration. (**A**) Representative concentration profiles of separated actin protein after 20s lysis, 25 s electrophoresis from BJ fibroblasts in the open (black) and closed (purple) system. Migration in the closed system is reduced due to low ion concentration. **(B)**. Representative concentration profiles of separated actin from single BJ fibroblast. The analyte distribution is shown after 20 s for the open system (black) and 65 seconds for the closed system (purple) (E-field = 150V, 20 s lysis). **(C)** Actin abundance as quantified by the area-under-the-curve at the conditions from subpanel B. P = 0.023

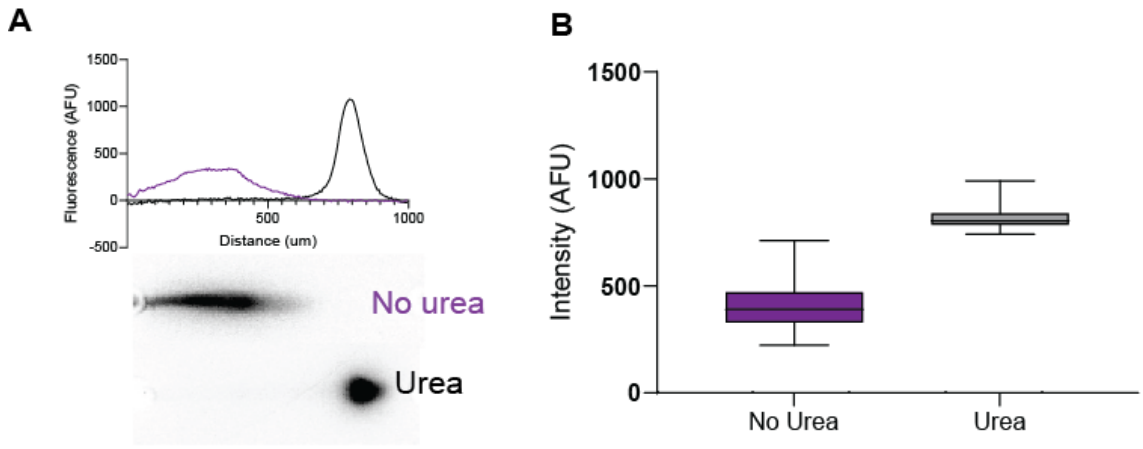

Figure 3.6: 6 M urea decreases peak width, improving separation resolution in the closed system. (A) Concentration profiles and representative epifluorescence micrographs of immunoprobed actin signal from single BJ fibroblast in the closed system in 2X RIPA and 2X + 6M urea buffer after 20 s lysis 40 s electrophoresis (E = 150 V). Separation lanes are 1000 µm in length (**B**) Boxplot of actin expression levels (intensity, AFU) from BJ fibroblasts with (grey) and without (purple) urea additive to the 2X RIPA buffer. Unpaired T-test p-value is significant (p-value < 0.0001). N = 262 and 153 for 'no urea' and 'urea' conditions, respectively.

To increase the separation resolution of the assay, narrow peak widths are desired. The introduction of 6M urea in the 2X RIPA buffer decreased peak width in the closed assay setup (**Figure 3.6A**). Without urea, actin injected 405 ± 93.8 µm into the polyacrylamide gel, with peak width of 110 ± 21.1 µm (n = 262). The addition of 6M urea significantly decreased band broadening (injection dispersion) without increasing the conductivity of the bifunctional lysis/EP 2X RIPA buffer (1.98 ± 0.0153 mS/cm for 2X RIPA buffer, and 1.47 ± 0.0153 mS/cm for 2X RIPA + 6M urea). With the addition of urea, actin injected 820 ± 48.5 µm into the polyacrylamide gel, with peak width of 49.1 ± 13.3 µm (n = 153). With the addition of urea, the measured fluorescence intensity post-immunoprobing is significantly greater for the system with urea (P<0000.1, unpaired T-Test) (**Figure 3.6B**). The average actin signal measured without urea from single cells was 405.0 ± 93.76 (n = 262). The average actin single measured with urea from single cells was 820.3 ± 48.53 (n = 153). The greater AFU for the same housekeeping protein suggests that the closed system with urea has a lower limit of detection that is twice improved compared to the closed system without urea, allowing for the detection of less abundant proteins.

Multiplexing by concurrent immunoprobing

To evaluate global protein response to substrate manipulation, multiplexed protein detection is desired. By leveraging the tunable feature of the analytical PAG layer, appropriate pore size and electrophoresis settings can be achieved to separate proteins in the ~40-125 molecular weight range **(Figure 3.7A**). Here, we sized 8 protein targets ranging from 42 kDa to 117 kDa in molecular mass from suspension cells in the closed assay system. As expected, we observed a linear trend between electromigration distance and the logarithmic value of the molecular mass

(**Figure 3.7B**). The 8 protein targets yield the relationship $y = -1504 * x + 3265$ (R^2 = 0.923), where $x = \log_{10} MW$. Optimization yields complete use of the 1 mm separation lane for the separation of actin (peak location = 859.1 ± 51.52 μm (n = 134) to vinculin (peak location = 206.3 ± 32.58 μm (n = 103)). With good separation resolution, as the result of minimized peak width and increased peak separation, antibodies from the same species can be combined and immunoprobed concurrently with the same secondary antibody (**Figure 3.7C)**. For example, primary antibodies against actin and actinin (**Figure 3.7C**, **purple trace)** can be combined for simultaneous probing regardless of host species. In addition to the molecular specificity from the immunoreagent, spatial separation yields additional target specificity.

The distance between protein peaks (Δx) and protein band width (4σ) impacts separation resolution [57]. Separation resolution can be mathematically summarized as:

$$R_s = \frac{\Delta x}{\frac{1}{2}(4\sigma_1 + 4\sigma_2)}$$

where Δx is the peak-to-peak displacement and the peak width is 4σ (σ, standard deviation of a Gaussian fit to a protein peak). When R_s >1.5, two targets are baseline-resolved and thus detectable. We calculate pairs of antibodies that have sufficient separation resolution for concurrent probing as proof of concept. Actin and actinin has a reported separation resolution of 4.88 ± 0.91 (n = 134). Similarly, β-tubulin and vinculin has a reported separation resolution of 3.34 ± 0.71 (n = 61). Lastly, vimentin and lamin A/C have a separation resolution of 1.18 ± 0.65 (n = 40). Depending on the quality of the antibody and the cellular abundance of the protein, the separation resolution of 1.18 might be sufficient for certain applications. Based on these results, antibodies can be pooled and immunoprobed concurrently. This enables higher order of multiplexing than competing assays.

Concurrent immunoprobing enables single-cell comparisons of cytoskeletal proteins. We observed that actin and actinin expression levels correlated well (R^2= 0.98), whereas actin and paxillin expression levels did not correlate as well (R^2= 0.37) for single cells. The high degree of correlation between actin and actinin can be explained by actinins role as an actin-binding protein. Actinin has been reported to function as a cross-linker for F-actin filaments [58], [59].

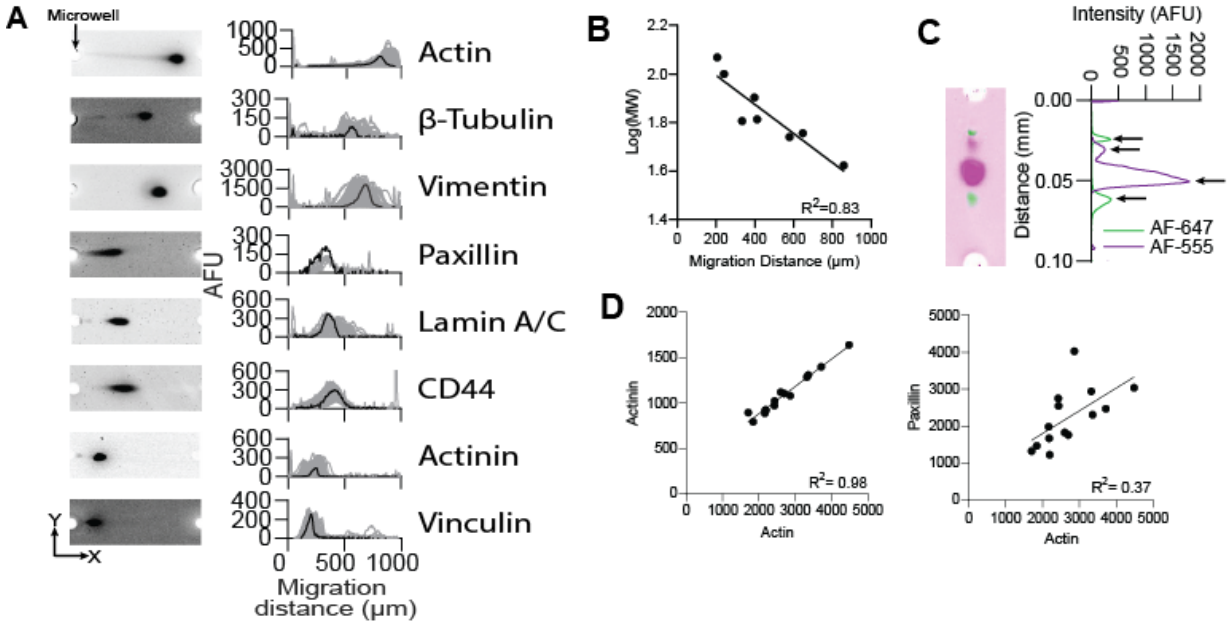

Figure 3.7: Concurrent probing detects proteins integral to stiffness sensing by separation-based multiplexing. (A) Representative false-color fluorescence micrographs and intensity profiles from separations of BJ fibroblasts with the closed, sandwich system. The 8 proteins were immunoprobed individually. Actin, 42 kDa (n = 134); beta-tubulin, 55 kDa (n = 61); Vimentin, 57 kDa (n = 144); Paxillin, 64 kDa (n = 5); Lamin A/C, 40 kDa (n = 40); CD44, 80 kDa (n = 29); Actinin, 100 kDa (n = 188); Vinculin, 117 kDa (n =103). Intensity profiles show traces of all separations in gray. **(B)** Relationship between electromigration distance and the logarithm value of molecular mass of 8 protein targets from lysed BJ fibroblasts in 8%T polyacrylamide gel. Line represents linear fit (R^2 = 0.835). **(C)** Representative false-color micrographs and intensity profiles of single-cell separation and concurrent probing for 4 proteins in 2 fluorescent channels. AF-647 secondary antibody (green) binds primary antibodies for actin and actinin, and AF-555 secondary antibody (purple) binds primary antibodies for paxillin and vimentin. **(D)** Scatter plot of actin vs actinin (left) and actin vs paxillin (right) for n = 14 single cells, with R^2 = 0.98 and 0.37, respectively. Line represents linear regression.

3.5: Conclusion

In summary, we present a method to quantitively evaluate cytoskeletal and focal adhesion protein abundance in response to various substrate stiffnesses in a high-throughput, single-cell sandwich assay. By combining a tunable substrate with the polyacrylamide gel used for size-based separation, we demonstrate preliminary work towards the measurement of signal-transducing molecules that participate in cytoskeletal organization in a quantitative, highly multiplexed fashion from adherent cells. We developed a two-layer assay with a fibronectin decorated PDMS side for cell culture and a microwell stippled PAG for protein sieving, capture and immunoprobing. This two-layer chip architecture permits the independent tuning of the extracellular microenvironment substrate and the separation matrix used for the concurrent

multiplexed detection of proteins. Imaging of the substrate layer prior to protein analysis enables the coupling of fundamental cell phenotype metrics with intracellular protein abundances. Due to the capture of proteins within the PAG after separation, concurrent probing (or a stripping and reprobing protocol, as reported elsewhere [60]) enables multiplexing beyond conventional immunocytochemistry methods. Next steps include marrying the individually tuned assay functions characterized here for the acquisition of phenotype and proteomic data from cells cultured on a range of stiffnesses.

The decoupled essay design allows for alternative matrix materials beyond PDMS. Matrigel, polyacrylamide, agarose, and other biomaterials can replace the PDMS layer, permitting the interrogation of cells response to a larger range of stiffnesses with the same device [63]. Lastly, the implementation of this assay for the detection of protein complexes (native electrophoresis buffer) compared to denatured conditions (in the presence of SDS, as presented here) can elucidate some of the binding events in the integrin clusters, integrin-actin linkers and the biochemical events that activate the formation of each [38].

Looking ahead, we anticipate that platforms such as this can aid in identifying new biomolecules involved in cancer development. Tissue stiffness increases in cases of fibrosis and cancer [61], [62]. Identifying aberrant single-cell behavior or unique protein phenotypes after mechano-stimulation can elucidate new drug targets by revealing new proteomic profiles of subpopulations of cells previously unstudied.

3.6: References

[1] A. N. Horvath, C. N. Holenstein, U. Silvan, and J. G. Snedeker, “The Protein Mat(ters) - Revealing biologically relevant mechaniacl contribution of collagen and fibronecin coated micropatterns,” *J Chem Inf Model*, vol. 53, no. 1, pp. 1689–1699, 2019, doi: 10.1017/CBO9781107415324.004.

[2] M. Gupta, L. Kocgozlu, B. R. Sarangi, F. Margadant, M. Ashraf, and B. Ladoux, *Micropillar substrates: A tool for studying cell mechanobiology*, vol. 125. Elsevier Ltd, 2015. doi: 10.1016/bs.mcb.2014.10.009.

[3] C. Rianna, M. Radmacher, and S. Kumar, “Direct Evidence that Tumor Cells Soften when Navigating Confined Spaces.,” *Mol Biol Cell*, p. mbcE19100588, 2020, doi: 10.1091/mbc.E19-10-0588.

[4] S. Nemir and J. L. West, “Synthetic materials in the study of cell response to substrate rigidity,” *Ann Biomed Eng*, vol. 38, no. 1, pp. 2–20, 2010, doi: 10.1007/s10439-009-9811-1.

[5] C. A. Mullen, T. J. Vaughan, K. L. Billiar, and L. M. McNamara, “The effect of substrate stiffness, thickness, and cross-linking density on osteogenic cell behavior,” *Biophys J*, vol. 108, no. 7, pp. 1604–1612, 2015, doi: 10.1016/j.bpj.2015.02.022.

[6] D. Li, J. Zhou, F. Chowdhury, J. Cheng, N. Wang, and F. Wang, “Role of mechanical factors in fate decisions of stem cells,” *Bone*, vol. 23, no. 1, pp. 1–7, 2008, doi: 10.1038/jid.2014.371.

[7] A. J. Engler, S. Sen, H. L. Sweeney, and D. E. Discher, “Matrix Elasticity Directs Stem Cell Lineage Specification,” *Cell*, vol. 126, no. 4, pp. 677–689, 2006, doi: 10.1016/j.cell.2006.06.044.

[8] D. M. Lyra-Leite *et al.*, “Mitochondrial function in engineered cardiac tissues is regulated by extracellular matrix elasticity and tissue alignment,” *Am J Physiol Heart Circ Physiol*, vol. 313, no. 4, pp. 757–767, 2017, doi: 10.1152/ajpheart.00290.2017.
[9] D. T. Nguyen, N. Nagarajan, and P. Zorlutuna, “Effect of Substrate Stiffness on Mechanical Coupling and Force Propagation at the Infarct Boundary,” *Biophys J*, vol. 115, no. 10, pp. 1966–1980, 2018, doi: 10.1016/j.bpj.2018.08.050.
[10] X. Tang, P. Bajaj, R. Bashir, and T. A. Saif, “How far cardiac cells can see each other mechanically,” *Soft Matter*, vol. 7, no. 13, pp. 6151–6158, 2011, doi: 10.1039/c0sm01453b.
[11] A. J. Engler *et al.*, “Embryonic cardiomyocytes beat best on a matrix with heart-like elasticity: Scar-like rigidity inhibits beating,” *J Cell Sci*, vol. 121, no. 22, pp. 3794–3802, 2008, doi: 10.1242/jcs.029678.
[12] S. Kumar, “Cell-extracellular matrix mechanobiology in cancer,” *Comprehensive Biophysics*, vol. 7, pp. 142–167, 2012, doi: 10.1016/B978-0-12-374920-8.00712-8.
[13] T. R. Cox, “The matrix in cancer,” *Nat Rev Cancer*, vol. 21, pp. 217–238, 2021, doi: 10.1038/s41568-020-00329-7.
[14] H. H. Lin *et al.*, “Mechanical phenotype of cancer cells: Cell softening and loss of stiffness sensing,” *Oncotarget*, vol. 6, no. 25, pp. 20946–20958, 2015, doi: 10.18632/oncotarget.4173.
[15] K. A. Jansen, D. M. Donato, H. E. Balcioglu, T. Schmidt, E. H. J. Danen, and G. H. Koenderink, “A guide to mechanobiology: Where biology and physics meet,” *Biochim Biophys Acta Mol Cell Res*, vol. 1853, no. 11, pp. 3043–3052, 2015, doi: 10.1016/j.bbamcr.2015.05.007.
[16] S. Hu, T. H. Chen, Y. Zhao, Z. Wang, and R. H. W. Lam, “Protein-Substrate Adhesion in Microcontact Printing Regulates Cell Behavior,” *Langmuir*, vol. 34, no. 4, pp. 1750–1759, 2018, doi: 10.1021/acs.langmuir.7b02935.
[17] L. Trichet *et al.*, “Evidence of a large-scale mechanosensing mechanism for cellular adaptation to substrate stiffness,” *Proc Natl Acad Sci U S A*, vol. 109, no. 18, pp. 6933–6938, 2012, doi: 10.1073/pnas.1117810109.
[18] S. Torino, B. Corrado, M. Iodice, and G. Coppola, “Pdms-based microfluidic devices for cell culture,” *Inventions*, vol. 3, no. 3, pp. 1–14, 2018, doi: 10.3390/inventions3030065.
[19] D. Mohammed *et al.*, “Innovative tools for mechanobiology: Unraveling outside-in and inside-out mechanotransduction,” *Front Bioeng Biotechnol*, vol. 7, no. JUL, 2019, doi: 10.3389/fbioe.2019.00162.
[20] D. Mitrossilis *et al.*, “Single-cell response to stiffness exhibits muscle-like behavior,” *Proc Natl Acad Sci U S A*, vol. 106, no. 43, pp. 18243–18248, 2009, doi: 10.1073/pnas.0903994106.
[21] Y. Zhang, I. Naguro, and A. E. Herr, “In Situ Single-Cell Western Blot on Adherent Cell Culture,” *Angewandte Chemie - International Edition*, vol. 58, no. 39, pp. 13929–13934, Sep. 2019, doi: 10.1002/anie.201906920.
[22] A. J. Hughes, D. P. Spelke, Z. Xu, C.-C. Kang, D. V Schaffer, and A. E. Herr, “Single-cell western blotting,” *Nat Methods*, vol. 11, no. 7, pp. 455–464, 2014.
[23] C.-C. Kang, K. A. Yamauchi, J. Vlassakis, E. Sinkala, T. A. Duncombe, and A. E. Herr, “Single cell-resolution western blotting,” *Nat Protoc*, vol. 11, no. 8, pp. 1508–1530, 2016.

[24] E. Jastrzebska *et al.*, “Biological characterization of the modified poly(dimethylsiloxane) surfaces based on cell attachment and toxicity assays,” *Biomicrofluidics*, vol. 12, no. 4, pp. 1–14, 2018, doi: 10.1063/1.5035176.
[25] S. Vichare, S. Sen, and M. M. Inamdar, “Cellular mechanoadaptation to substrate mechanical properties: Contributions of substrate stiffness and thickness to cell stiffness measurements using AFM,” *Soft Matter*, vol. 10, no. 8, pp. 1174–1181, 2014, doi: 10.1039/c3sm51786a.
[26] S. Hu, T. H. Chen, Y. Zhao, Z. Wang, and R. H. W. Lam, “Protein-Substrate Adhesion in Microcontact Printing Regulates Cell Behavior,” *Langmuir*, vol. 34, no. 4, pp. 1750–1759, Jan. 2018, doi: 10.1021/acs.langmuir.7b02935.
[27] R. A. Desai, N. M. Rodriguez, and C. S. Chen, “‘Stamp-off’ to micropattern sparse, multicomponent features,” in *Methods in Cell Biology*, vol. 119, Academic Press Inc., 2014, pp. 3–16. doi: 10.1016/B978-0-12-416742-1.00001-9.
[28] W. J. Adams, T. Pong, N. A. Geisse, S. P. Sheehy, B. Diop-Frimpong, and K. K. Parker, “Engineering design of a cardiac myocyte,” in *Journal of Computer-Aided Materials Design*, Apr. 2007, vol. 14, no. 1, pp. 19–29. doi: 10.1007/s10820-006-9045-6.
[29] S. Weng and J. Fu, “Synergistic regulation of cell function by matrix rigidity and adhesive pattern,” *Biomaterials*, vol. 32, no. 36, pp. 9584–9593, Dec. 2011, doi: 10.1016/j.biomaterials.2011.09.006.
[30] S. Halldorsson, E. Lucumi, R. Gómez-sjöberg, and R. M. T. Fleming, “Advantages and challenges of micro fluidic cell culture in polydimethylsiloxane devices,” *Biosensors and Bioelectronic*, vol. 63, pp. 218–231, 2015, doi: 10.1016/j.bios.2014.07.029.
[31] A. J. Hughes, D. P. Spelke, Z. Xu, C. C. Kang, D. v. Schaffer, and A. E. Herr, “Single-cell western blotting,” *Nat Methods*, vol. 11, no. 7, pp. 749–755, 2014, doi: 10.1038/nmeth.2992.
[32] J. Vlassakis, K. A. Yamauchi, and A. E. Herr, “Summit: Automated Analysis of Arrayed Single-Cell Gel Electrophoresis,” *SLAS Technol*, vol. 26, no. 6, pp. 637–649, Dec. 2021, doi: 10.1177/24726303211036869.
[33] M. E. Moustafa, V. S. Gadepalli, A. A. Elmak, W. Lee, R. R. Rao, and V. K. Yadavalli, “Large area micropatterning of cells on polydimethylsiloxane surfaces,” *J Biol Eng*, vol. 8, no. 1, Oct. 2014, doi: 10.1186/1754-1611-8-24.
[34] P. Hermanowicz, M. Sarna, K. Burda, and H. Gabryś, “AtomicJ: An open source software for analysis of force curves,” *Review of Scientific Instruments*, vol. 85, no. 6, p. 063703, Jun. 2014, doi: 10.1063/1.4881683.
[35] A. J. S. Ribeiro, A. K. Denisin, R. E. Wilson, and B. L. Pruitt, “For whom the cells pull: hydrogel and micropost devices for measuring traction forces,” *Methods*, pp. 1–40, 2019.
[36] K. A. Jansen, P. Atherton, and C. Ballestrem, “Mechanotransduction at the cell-matrix interface,” *Semin Cell Dev Biol*, vol. 71, pp. 75–83, 2017, doi: 10.1016/j.semcdb.2017.07.027.
[37] C. Argentati *et al.*, “Insight into mechanobiology: How stem cells feel mechanical forces and orchestrate biological functions,” *Int J Mol Sci*, vol. 20, no. 21, 2019, doi: 10.3390/ijms20215337.
[38] Z. Jahed, H. Shams, M. Mehrbod, and M. R. K. Mofrad, *Mechanotransduction pathways linking the extracellular matrix to the nucleus*, 1st ed., vol. 310. Elsevier Inc., 2014. doi: 10.1016/B978-0-12-800180-6.00005-0.

[39] B. Yi, Q. Xu, and W. Liu, “An overview of substrate stiffness guided cellular response and its applications in tissue regeneration,” *Bioact Mater*, vol. 15, pp. 82–102, Sep. 2022, doi: 10.1016/J.BIOACTMAT.2021.12.005.
[40] K. E. Scott, S. I. Fraley, and P. Rangamani, “A spatial model of YAP/TAZ signaling reveals how stiffness, dimensionality, and shape contribute to emergent outcomes,” *Proc Natl Acad Sci U S A*, vol. 118, no. 20, p. e2021571118, May 2021, doi: 10.1073/PNAS.2021571118/SUPPL_FILE/PNAS.2021571118.SAPP.PDF.
[41] P. A. Janmey, D. A. Fletcher, and C. A. Reinhart-King, “Stiffness sensing by cells,” *Physiol Rev*, vol. 100, no. 2, pp. 695–724, Apr. 2020,
[42] P. A. Janmey, J. P. Winer, M. E. Murray, and Q. Wen, “The hard life of soft cells,” *Cell Motil Cytoskeleton*, vol. 66, no. 8, pp. 597–605, 2009, doi: 10.1002/cm.20382.
[43] M. E. Moustafa, V. S. Gadepalli, A. A. Elmak, W. Lee, R. R. Rao, and V. K. Yadavalli, “Large area micropatterning of cells on polydimethylsiloxane surfaces,” *J Biol Eng*, vol. 8, no. 1, pp. 1–10, 2014, doi: 10.1186/1754-1611-8-24.
[44] E. Hadjipanayi, V. Mudera, and R. A. Brown, “Close dependence of fibroblast proliferation on collagen scaffold matrix stiffness,” *J Tissue Eng Regen Med*, vol. 3, pp. 77–84, 2009.
[45] R. A. Scott, K. G. Robinson, K. L. Kiick, and R. E. Akins, “Human Adventitial Fibroblast Phenotype Depends on the Progression of Changes in Substrate Stiffness,” *Adv Healthc Mater*, vol. 9, no. 8, pp. 1–12, 2020, doi: 10.1002/adhm.201901593.
[46] B. L. Doss *et al.*, “Cell response to substrate rigidity is regulated by active and passive cytoskeletal stress,” *Proc Natl Acad Sci U S A*, vol. 117, no. 23, pp. 12817–12825, 2020, doi: 10.1073/pnas.1917555117.
[47] M. Ochsner, M. Textor, V. Vogel, and M. L. Smith, “Dimensionality controls cytoskeleton assembly and metabolism of fibroblast cells in response to rigidity and shape,” *PLoS One*, vol. 5, no. 3, pp. 25–27, 2010, doi: 10.1371/journal.pone.0009445.
[48] M. Prager-Khoutorsky *et al.*, “Fibroblast polarization is a matrix-rigidity-dependent process controlled by focal adhesion mechanosensing,” *Nat Cell Biol*, vol. 13, no. 12, pp. 1457–1465, 2011, doi: 10.1038/ncb2370.
[49] C. T. Lo, D. J. Throckmorton, A. K. Singh, and A. E. Herr, “Photopolymerized diffusion-defined polyacrylamide gradient gels for on-chip protein sizing,” *Lab Chip*, vol. 8, no. 8, pp. 1273–1279, Jul. 2008, doi: 10.1039/B804485F.
[50] S. Kumar and A. Pathak, “Transforming potential and matrix stiffness co-regulate confinement sensitivity of tumor cell migration,” *Integrative Biology (United Kingdom)*, vol. 5, no. 8, pp. 1067–1075, 2013, doi: 10.1039/c3ib40017d.
[51] O. Iendaltseva, V. v. Orlova, C. L. Mummery, E. H. J. Danen, and T. Schmidt, “Fibronectin Patches as Anchoring Points for Force Sensing and Transmission in Human Induced Pluripotent Stem Cell-Derived Pericytes,” *Stem Cell Reports*, vol. 14, no. 6, pp. 1107–1122, Jun. 2020, doi: 10.1016/j.stemcr.2020.05.001.
[52] D. Qin, Y. Xia, and G. M. Whitesides, “Soft lithography for micro- and nanoscale patterning,” *Nat Protoc*, vol. 5, no. 3, pp. 491–502, Mar. 2010, doi: 10.1038/nprot.2009.234.
[53] M. Liu, J. Sun, Y. Sun, C. Bock, and Q. Chen, “Thickness-dependent mechanical properties of polydimethylsiloxane membranes,” *Journal of Micromechanics and Microengineering*, vol. 19, no. 3, 2009, doi: 10.1088/0960-1317/19/3/035028.

[54] S. Y. Chou, C. M. Cheng, and P. R. LeDuc, "Composite polymer systems with control of local substrate elasticity and their effect on cytoskeletal and morphological characteristics of adherent cells," *Biomaterials*, vol. 30, no. 18, pp. 3136–3142, 2009, doi: 10.1016/j.biomaterials.2009.02.037.
[55] P. A. Janmey, D. A. Fletcher, and C. A. Reinhart-King, "Stiffness Sensing by Cells," *Physiol Rev*, vol. 100, no. 2, pp. 695–724, 2020, doi: 10.1152/physrev.00013.2019.
[56] E. J. Su and A. E. Herr, "Electrophoretic cytometry of adherent cells," *Lab Chip*, vol. 17, no. 24, pp. 4312–4323, Dec. 2017, doi: 10.1039/c7lc01012e.
[57] C. C. Kang, K. A. Yamauchi, J. Vlassakis, E. Sinkala, T. A. Duncombe, and A. E. Herr, "Single cell-resolution western blotting," *Nat Protoc*, vol. 11, no. 8, pp. 1508–1530, Aug. 2016, doi: 10.1038/nprot.2016.089.
[58] A. C. H. Murphy and P. W. Young, "The actinin family of actin cross-linking proteins - A genetic perspective," *Cell Biosci*, vol. 5, no. 1, pp. 1–9, Aug. 2015, doi: 10.1186/S13578-015-0029-7/TABLES/1.
[59] C. M. Hampton, D. W. Taylor, and K. A. Taylor, "Novel structures for α-actinin: F-actin interactions and their implications for actin-membrane attachment and tension sensing in the cytoskeleton," *J Mol Biol*, vol. 368, no. 1, p. 92, Apr. 2007, doi: 10.1016/J.JMB.2007.01.071.
[60] A. Gopal and A. E. Herr, "Multiplexed in-gel microfluidic immunoassays: characterizing protein target loss during reprobing of benzophenone-modified hydrogels," *Sci Rep*, vol. 9, no. 1, Dec. 2019, doi: 10.1038/S41598-019-51849-8.
[61] I. Levental *et al.*, "A simple indentation device for measuring micrometer-scale tissue stiffness," *Journal of Physics: Condensed Matter*, vol. 22, no. 19, p. 194120, Apr. 2010, doi: 10.1088/0953-8984/22/19/194120.
[62] M. Yin *et al.*, "Assessment of Hepatic Fibrosis With Magnetic Resonance Elastography," *Clinical Gastroenterology and Hepatology*, vol. 5, no. 10, pp. 1207-1213.e2, Oct. 2007, doi: 10.1016/J.CGH.2007.06.012.
[63] P. Y. Wang, W. B. Tsai, and N. H. Voelcker, "Screening of rat mesenchymal stem cell behaviour on polydimethylsiloxane stiffness gradients," *Acta Biomater*, vol. 8, no. 2, pp. 519–530, 2012, doi: 10.1016/j.actbio.2011.09.030.

Chapter 4: Mitigation of non-Gaussian injection profiles in open electro-separations

4.1: Introduction

Microscale systems for single-cell proteome measurements include various electrophoresis (EP) methods. Common to these systems is the injection of the biomolecular analyte into the analytic medium [1]–[3]. Once the biomolecular analyte is separated within the matrix, it is detected by a range of methods, such as laser-induced fluorescence or absorbance detection [4]. Under ideal conditions, the injected sample will form a Gaussian concentration profile, stemming from the molecular diffusion of analyte particles during electrophoretic separations [5]. This model can be expanded to 2D Gaussian shape with equal widths in two dimensions. Thus, common analysis schemes of analyte injections, bands, and signal use parametric methods of Gaussian models. For the quantification of protein expression, a Gaussian curve is fit to the intensity profile and integral analysis (i.e., area-under-the-curve analysis) reports the protein abundance [6], [7].

In addition to diffusion, dispersion can contribute to band shape. Dispersion is a compound parameter combining contributions from modes of flow, modes of mass transport, mobile phase viscosity, solute size, and friction. In electrophoretic separations, separation-degrading band broadening is a transport phenomenon of diffusion, channel geometry, Joule heating, adsorption, and electromigration [8]–[10]. Poor agreement between analyte signal, whether protein or DNA, with Gaussian concentration profile results in poor separation resolution. Broad, overlapping signal bands are difficult to deconvolve due decreased stacking effects [11]. Controlling band broadening factors generates efficient and effective separation during electrophoresis.

Non-Gaussian analyte bands are evident under certain conditions in both bulk and microscale assays. For example, the extraction of proteins from single circulating tumor cells using open-microfluidic electrophoretic separations show cell-to-cell heterogeneity in protein injection and signal shape, deviating from the Gaussian ideal [12]. In DNA separation assays, such as the COMET assay, DNA is extracted from agarose-embedded cells, generating comet-like streaks upon application of an electric field [13]–[15]. Assays utilizing stepwise solubility, such as the microscale, subcellular western blot (DDF) [16], but also bulk assays, such as native polyacrylamide gel electrophoresis [17]–[20], often have analyte distributions that deviates from the idealized Gaussian shape. Existing remedial approaches to band broadening include: 1) injection of a sample plug [8], [21], 2) efficient dissipation of Joule heating during applied electric field [22], [23], 3) elimination of turns in channel-based devices [24], and 4) accounting for signal skew in data analysis [25].

Here, we investigated remedial means to injection dispersion in open microfluidic devices. We have observed intrapopulation variation in the magnitude of injection dispersion across devices designed for parallel interrogation of 100s of cells simultaneously. In these cases, we often see a split in the population of injections with dispersion phenotype and those without. We hypothesized dispersion to stem from incomplete solubilization of. To combat non-Gaussian peaks across the device and improve resolution efficiency within a finite separation distance, we studied the effect of temperature and lysis conditions on injection efficiency using the single-cell western blotting platforms as model systems. For assays that have fixed buffer composition, we

increased temperature to mitigate injection dispersion. For assays that do not have fixed buffer composition, we increased the detergent concentration. In both cases, injection dispersion heterogeneity decreased as the solubility of the analyte concentration increased. We hypothesized that protein state contributes significantly to band broadening in the single-cell western blot.

4.2: Results

Mitigating non-Gaussian peaks with increased detergent in cases with variable buffer composition

In situations where the extraction of protein from the cellular compartment is the target, increased detergent concentration can improve solubilization of biomolecules. We investigated the effect of increasing detergent concentration on band shape and injection dispersion in the single-cell western blot format.

We hypothesized that intrapopulation heterogeneity in cell solubility contributing to injection dispersion phenotypes could be combatted with increased detergent concentration. Cell-to-cell variations in lysis-hardiness have been reported previously and would manifest as intrapopulation variation in injection dispersion magnitude and contribute to biological sources of variation [12], [26]. Ionic detergent such as sodium dodecyl sulfate (SDS) and sodium deoxycholate (Na-DOC) solubilize the membrane and denature proteins. In comparison, non-ionic detergents and increased lysis duration is expected to enhance membrane solubilization [27]–[29]. A contributing factor to injection dispersion is poorly denatured or solubilized proteins. Insoluble proteins migrate slower than their soluble counterparts, resulting in band broadening. While increasing the temperature also enhances solubilization and denaturation, elevated temperatures also increase the diffusive losses of single-cell proteins out of the open microwell [12], [30].

To evaluate the effect of increased detergent concentration, we used the single-cell western blot platform as a model system [31]. An 8%T polyacrylamide gel with 50 µm diameter microwells were used to evaluate the migration patterns of housekeeping proteins. U-2 OS cells, derived from a differentiated osteosarcoma, were settled into the microwells at a concentration of 10^5 cells/mL, optimized to achieve single-cell well occupancy. Cells were lysed on-chip with either 1X or 2X RIPA buffer, functioning as both the lysis and electrophoresis buffer. Here, the 1X RIPA buffer consists of 1X Tris-Glycine, 0.5% SDS, 0.25% Na-DOC, and 0.1% Triton X-100 in deionized water. 2X RIPA contains 1% SDS and 0.5% Na-DOC. The buffers were heated to 55C prior to use. 15 mL of buffer was applied to the microwell gel and allowed to diffuse into the open microwells for lysis. Cell lysis proceeded for 20 seconds before an electric field was applied at 40 V/cm (E_{field} = 240V) for 20 seconds. Proteins were immediately photo-captured inside the gel by UV-immobilization via an incorporated benzophenone moiety in the polyacrylamide gel backbone during fabrication. Gels were rinsed in 1X TBST and then immunoprobed with protein-specific primary antibodies at a 1:10 dilution for 2 hours. After 1 hour of washing with buffer exchanged every 30 minutes, the gels were subjected to fluorescent secondary antibody at a 1:20 dilution for 1 hour. The washing process was repeated, and the gels were dried. Fluorescence intensity was recorded by a laser array scanner with filters suitable for the reporters on the secondary antibody. We used AlexaFluor-647. Due to antibody shortage and

supply chain issues during the COVID19 pandemic, this study compares actin (in the 2X RIPA condition) with β-tubulin (in the 1X RIPA condition). Both proteins participate in quaternary protein complexes in the cytoskeleton. While their migration distances cannot be compared due to differences in molecular weight (actin = 42 kDa, β-tubulin = 55 kDa), we hypothesize that their solubility and injection patterns are comparable due to their similar protein structure and location within the cell. Gel images were analyzed with previously published pipeline [25].

In cases with injection dispersion, a skewed peak function was used for fitting rather than the Gaussian protein profile (**Figure 4.1**). The density function of the skew normal distribution is given by [32], [33]:

$$f(x) = 2\phi(x)\Phi(\alpha x) \quad \text{Eq. 1}$$

Where $\phi(x)$ is the density function of a standard normal/Gaussian distribution and $\Phi(\alpha x)$ is the cumulative distribution function. Here α is the shape (or asymmetry) parameter. When α = 0, skew is absent, and the function is a standard normal density function. As the absolute value of α increases, the skewness of the distribution increases. A negative α means that the density left-skewed.

Separations from the mild detergent condition displayed consistent injection dispersion within the population. In the mild detergent condition, the protein band broadening reduces separation efficiency. Due to the skew in signal shape in the mild detergent condition, with an average α of -0.3 (n = 142), the peak width is greater than that of the high detergent condition. In the case of 1X RIPA, the calculated peak width was 108.3 ± 31.05 μm (n = 263) (**Figure 4.2**). In 2X RIPA, the peak width was 50.22 ± 6.285 μm (n = 171). Doubling the detergent concentration narrowed the protein band width to half of mild detergent condition ($P < 0.001$). In addition, with 2X RIPA, cell-to-cell differences in peak width decrease, as evident in magnitude of the standard deviation. This results in greater throughput per chip and more robust single-cell separations. In summary, increasing the detergent concentration improves separation performance by reducing peak width of analyte signal.

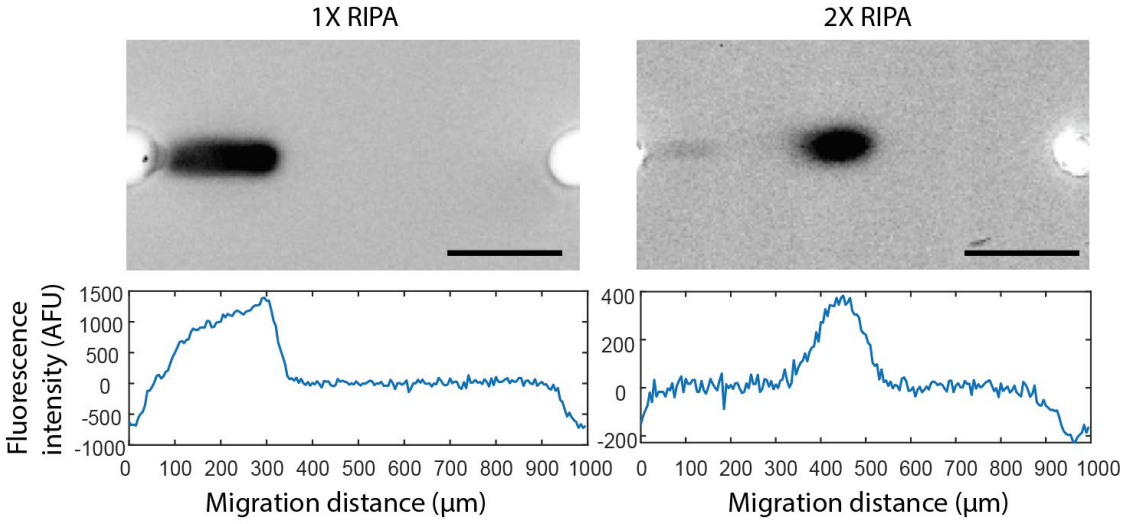

Figure 4.1: Without sufficient detergent to solubilize proteins, injection dispersion dominates protein band shape. Representative false-color fluorescence micrograph of skewed Gaussian peak (left, 1X RIPA) and Gaussian peak (right, 2X RIPA) and intensity profile for the corresponding separation region. Protein in 1X RIPA separation is β-Tubulin (55 kDa) and protein in 2X RIPA separation is actin (42 kDa). Used here for comparison due to antibody shortage, both proteins are cytoskeletal proteins participating in multimeric complexes within the cytosolic compartment of cells. Scale bars are 250 µm.

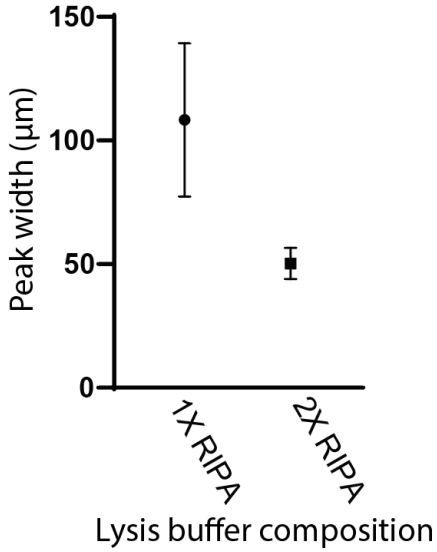

Figure 4.2: Increasing the detergent concentration decreases signal peak width and intrapopulation injection heterogeneity. Peak width (in µm) for immunoprobed β-Tubulin (1X RIPA) and actin (2X RIPA) after 20 seconds of lysis and 20 seconds of electrophoresis in the standard single-cell western blot setup. Samples pooled from 2 devices for each condition, with total n = 263 and n = 171 for 1X RIPA and 2X RIPA, respectively. $P < 0.001$.

Mitigating non-Gaussian peaks with heat in cases with fixed buffer composition

Lysis buffers composition is often fixed for assays with high analytical selectivity, such as SIFTER and DDF. In DDF, nuclear and cytoskeletal protein localization is determined by stepwise lysis of the cell [16]. In SIFTER, protein complex and monomer populations are quantified by stepwise disruption of filaments [34]. In both cases, the lysis buffer composition has been optimized for specific molecular targets. The additional analytical sensitivity of both assays is reliant on selective and sequential lysis. Thus, the addition of supplementary chemical agents to eliminate injection dispersion would disrupt the biological function of the assay.

Instead, increased temperature can be used to decrease band broadening. Temperature variations is a common utility to improve performance and speed up electrophoretic separations. A 5 °C temperature change can produce a 0.1 unit change in pH and >25% change in observable mobility of analytes [35]. At elevated temperatures, buffer viscosity is also reduced, leading to significant reduction in analysis time. In addition, the critical micelle concentration aggregation number and the solubility of detergents are highly dependent on temperature. Thus, higher temperatures contribute to keeping the analyte biomolecule denatured, necessary for predictable analyte migration in an electrophoretic assay [36], [37]. Failure to completely solubilize all proteins in the sample will result in streaking along the direction of injection as conferred mobility is inconsistent. We hypothesized that at high temperatures, enhanced solubilization of samples and increased solubility of salts decrease band broadening in assays where buffer components cannot be altered.

To evaluate the impact of higher temperatures on single-cell separations with fixed lysis buffers, SIFTER devices were run at room temperature and at elevated temperature, and the resultant protein signal was analyzed. We implemented a PID-controlled heater that monitors and manages a constant temperature at a setpoint. The comprehensive protocol has been described elsewhere [34]. In short, MDA-MB-231 cells were settled into microwells in an 8%T polyacrylamide gel, functionalized with a UV-reactive BPMA moiety. Cells were lysed in complex-stabilizing buffer, and the monomers are separated from the cell lysate by electrophoresis. Size-exclusion of maintained protein complexes in the microwell permits the spatial separation of monomers and complexes by electrophoretic migration. The monomer subpopulation is immobilized by UV and BPMAC capture. A second, complete lysis of the cells precedes a second electrophoresis step and UV capture of the complex subpopulation in a spatially separate region from the monomeric population. In total, these steps results in assay output characterized by a signal peak on one side of the microwell corresponding to the monomeric analyte fraction (globular actin, or G-actin), and a separate signal peak on the other side of the microwell for the (now-dissociated) multimeric analyte fraction (filamentous actin, or F-actin). For high temperature runs, a PID heater was applied to the underside of the gel-containing glass slide for the duration of lysis and electrophoresis. PID heater was set to keep gels at a 55 °C. For low temperature runs, the same setup was used at room temperature without powering the PID heater. For both, gels were immunoprobed with anti-actin antibodies and imaged by laser array scanner. Analysis was carried out as explained elsewhere [25]. All runs were executed in triplicates. We classified a single-cell separation as being with injection dispersion if there the protein signal did not reach near-baseline near the microwell (**Figure 4.3**).

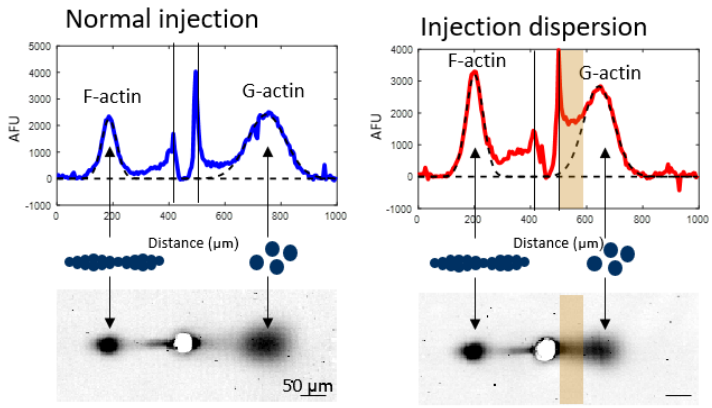

Figure 4.3: Representative phenotypes of cell-to-cell differences in injection patterns within a single SIFTER device. Micrographs and intensity profiles for single-cell, SIFTER separations of normal injection (left) and injection dispersion (right). Gels were immunoprobed for actin, with actin from F-actin on the left of the microwell, and G-actin on the right. G-actin separations inconsistently contain injection dispersion, evident as signal between the microwell and the gel (highlighted in gold). Scale bar = 50 µm.

All analyzed lanes for both temperature conditions were categorized as either having injection dispersion or no injection dispersion (normal) (**Figure 4.3**). These subpopulations were analyzed and compared to investigate the effect of temperature on injection dispersion.

In the SIFTER assay, injection dispersion is most commonly visible on the G-actin side of the separation. This corresponds to the electrophoretic injection done under mild (i.e., native) lysis conditions to maintain protein filament structure of the F-actin. As such, we analyzed the G-actin signal intensity in isolation to evaluate the effect of temperature. Importantly, both gaussian and non-gaussian injection profiles are observed for G-actin within a single device. Each device yields 100s of single-cell separations, separated into respective separation lanes. The presence of both phenotypes on a single device suggests remedial approaches should target biological sources of variation rather than technical sources of variation.

With room temperature electrophoresis, 45.9% of the analyzed lanes (each representing a single-cell electrophoretic fractionation) were found to have injection dispersion (n = 242). In comparison with the PID heater fixing the system temperature at 55 °C, only 12.9% of analyzed the lanes had injection dispersion (n = 380). The increased sample size might be the result of more separation lanes passing the quality-control steps of the data analysis pipeline due to properly injected signal [25]. To quantify the injection dispersion heterogeneity within a population, we looked at the G-actin abundance (AFU), as quantified by the area-under-the-curve for the Gaussian and non-Gaussian peaks (**Figure 4.4A)** We find that the injection dispersion subpopulation for both temperature conditions had greater G-actin signal than the injections without dispersion (**Figure 4.4B**). However, the difference between the reported values for the G-actin abundance for the two subpopulations of the heated system is negligible ($P < 0.001$).

Another way to increase the solubility of the protein is to increase the lysis time. We increased the lysis time from 45 s to 55 s. This was a second approach for confirmation of solubility contributing significantly to injection dispersion in the SIFER assay. All assays were run at room temperature. With 45 s lysis, 45.9% of cells expressed injection dispersion (n = 242). With 55 s lysis, 38.9% of cells expressed injection dispersion (n = 154). Like the case with the heater, we find that the injection dispersion population for both conditions had greater G-actin signal than the single-cell injections without dispersion. In this case, the difference between the reported values for the G-actin abundance for the two subpopulations is statistically significant ($P = 0.036$) (**Figure 4.4C**). Increasing lysis time did not appear to significantly improve solubility of proteins to mitigate biological sources of technical variation.

While increasing the lysis time and increasing the temperature of the separation both decreased the number of cells with injection dispersion, we recommend using heat whenever possible. In addition to having the most robust remedial effects on injection dispersion profiles, the run-to-run variation also decreased (**Figure 4.5**). Three separate devices were compared for each of the conditions. The run-to-run variation for the room-temperature devices was statistically significant ($P = 0.008$), while it as not statistically significant for the heated devices ($P < 0.001$). For room-temperature devices, biological variation inhibits device pooling to achieve greater sample sizes, often necessary for single-cell statistical methods. By improving reproducibility from device-to-device while keeping dispersion count low, the number of cells analyzed per chip increased with heat ($n = 126.7 \pm 21.39$ cells for heated devices, and $n = 75.67 \pm 49.14$ for room-temperature devices) In addition to run-to-run variation, the room-temperature devices had greater interquartile ranges (IQR) than the heated device. IQRs for room-temperature devices were 2.213e4, 4.290e4, 2.565e4 AFU. IQRs for heated devices were 1.543e4, 1.032e4, and 1.790e4 AFU.

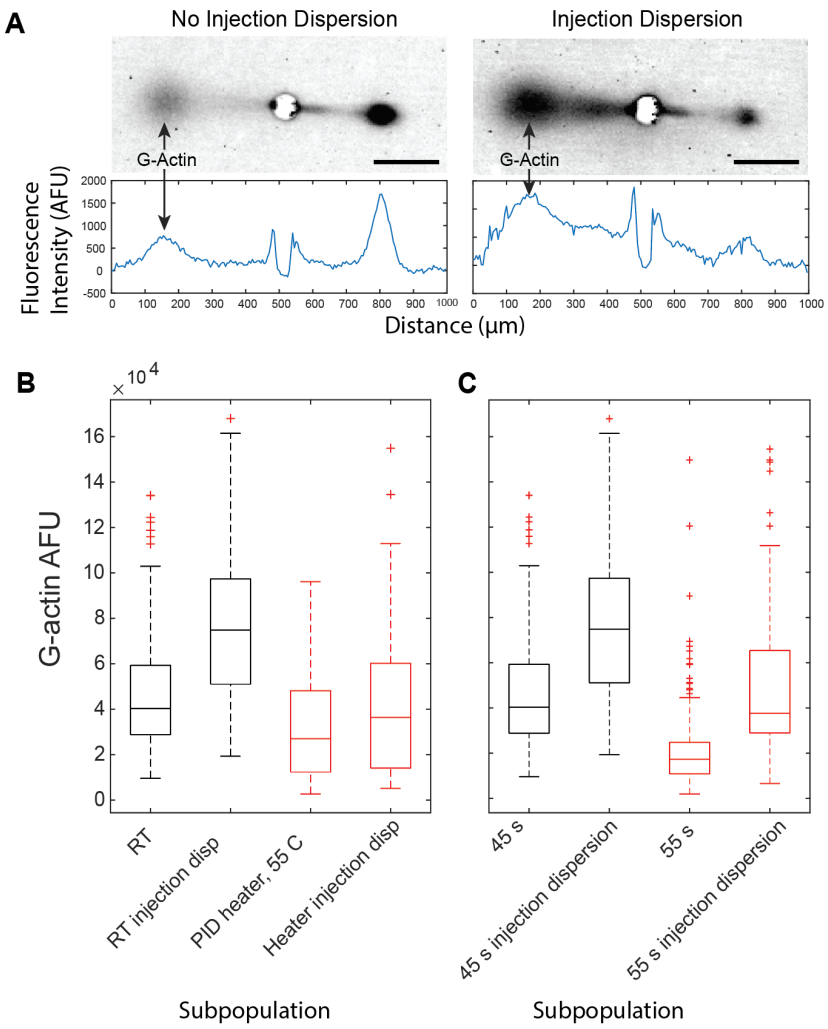

Figure 4.4: Increasing solubility of protein by heated lysis or longer lysis improved performance of the SIFTER assay. (A) Intensity profile of actin bi-directional separation with G-actin peaks on the left of each well, and F-actin on the right. Standard Gaussian injection (left) and injection with dispersion (right) occur on the same device, suggesting cell-to-cell heterogeneity. Intensity profile shows non-baseline signal between the microwell and the G-actin signal, indicative of the injection dispersion phenotype. Scale bar = 200 μm. **(B)** Implementation of PID heater (red) to make the lysis temperature 55 °C decreased the analytical difference between injection dispersion (injection disp) and standard injection subpopulations. RT = Room temperature, disp = injection dispersion. **(C)** Increasing the lysis time from 45 s to 55 s at room temperature did not affect the difference between the reported G-actin abundance of the injection dispersion and standard subpopulations

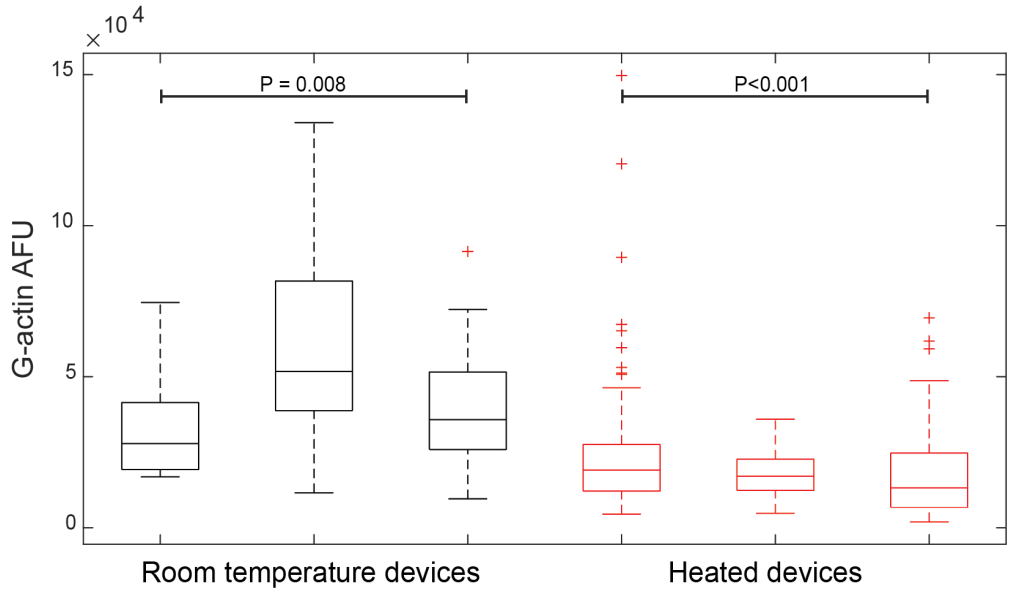

Figure 4.5: Run-to-run variation is improved with fixed lysis temperature at 55 °C by PID heater. Boxplot of three devices run on the same day from the same starting cell population with room temperature (black, N = 9, 53, 69) and heated (red, N = 128, 111, 92) devices. Y-axis is the area-under-the-curve for the signal peak corresponding to G-actin.

4.3: Conclusion

For the development of high-performance electrophoretic systems of small starting sample volume, minimizing dispersion positively impacts separation resolution and limit of detection. Electrophoretic band broadening is due to a sum of various factors, with different factors dominating each assay. This study focused on deviations from the idealized Gaussian shape because of incomplete solubility schemes. We evaluated means of limiting injection dispersion from single-cell samples. We found that increasing the temperature of lysis and electrophoresis drastically reduced the number of single-cell injections with dispersion on a single device. It also improved the reproducibility of the assay by decreasing run-to-run variation. Similarly, increasing the ionic detergent concentration decreased peak width and mitigated cell-to-cell injection phenotypes that lead to low sample sizes.

For electrophoretic cytometry readouts that result in 2D images of the analytes (such as those reported here), additional features can be extracted beyond protein abundance quantification. For example, the presence of injection dispersion could be an indicator of a specific chemical and biophysical interactions not dealt with by the employed sample preparation method. Cell-to-cell differences in solubility as evident by band broadening could be indicative of a solubilization-resistant subpopulation with biological phenotype of interest [38]. We anticipate that future work may shed light on metrics of injection dispersion for sample preparation optimization or insight into especially robust sample types [12].

4.4: References

[1] R. Bharadwaj, J. G. Santiago, and B. Mohammadi, "Design and optimization of on-chip capillary electrophoresis," *Electrophoresis*, vol. 23, no. 16, pp. 2729–2744, Aug. 2002, doi: 10.1002/1522-2683(200208)23:16

[2] E. Grushka, R. M. McCormick, and J. J. Kirkland, "Effect of Temperature Gradients on the Efficiency of Capillary Zone Electrophoresis Separations," 1989

[3] J. H. Knox, "Thermal Effects and Band Spreading in Capillary Electro-Separation," *Chromatographia*, vol. 26, pp. 329–337, 1988.

[4] K. E. Oldenburg, X. Xi, and J. v. Sweedler, "High resolution multichannel fluorescence detection for capillary electrophoresis Application to multicomponent analysis," *J Chromatogr A*, vol. 788, no. 1–2, pp. 173–183, Nov. 1997, doi: 10.1016/S0021-9673(97)00713-9.

[5] P. C. Wankat, "Unified separation science. By J. Calvin Giddings, Wiley, New York, 320 pp., 1991," *AIChE Journal*, vol. 38, no. 8, pp. 1303–1303, Aug. 1992, doi: 10.1002/AIC.690380818.

[6] M. Gassmann, B. Grenacher, B. Rohde, and J. Vogel, "Quantifying Western blots: Pitfalls of densitometry," *Electrophoresis*, vol. 30, no. 11, pp. 1845–1855, Jun. 2009, doi: 10.1002/ELPS.200800720.

[7] T. A. J. Butler, J. W. Paul, E.-C. Chan, R. Smith, and J. M. Tolosa, "Misleading Westerns: Common Quantification Mistakes in Western Blot Densitometry and Proposed Corrective Measures," 2019, doi: 10.1155/2019/5214821.

[8] S. Datta and S. Ghosal, "Characterizing dispersion in microfluidic channels," *Lab on a Chip*, vol. 9, no. 17. Royal Society of Chemistry, pp. 2537–2550, 2009. doi: 10.1039/b822948c.

[9] Z. Chen and S. Ghosal, "Electromigration Dispersion in Capillary Electrophoresis," *Bull Math Biol*, vol. 74, no. 2, pp. 346–355, Feb. 2012, doi: 10.1007/s11538-011-9708-7.

[10] S. Whitaker, "Diffusion and Dispersion in Porous Media," 1967.

[11] A. J. Pfeiffer, T. Mukherjee, and S. Hauan, "Design and optimization of compact microscale electrophoretic separation systems," *Ind Eng Chem Res*, vol. 43, no. 14, pp. 3539–3553, Jul. 2004, doi: 10.1021/IE034071T/ASSET/IMAGES/LARGE/IE034071TF00026.JPEG.

[12] E. Sinkala *et al.*, "Profiling protein expression in circulating tumour cells using microfluidic western blotting," *Nat Commun*, vol. 8, Mar. 2017, doi: 10.1038/ncomms14622.

[13] O. Östling and K. J. Johanson, "Bleomycin, in Contrast to Gamma Irradiation, Induces Extreme Variation of DNA Strand Breakage from Cell to Cell," *http://dx.doi.org/10.1080/09553008714552201*, vol. 52, no. 5, pp. 683–691, 2009, doi: 10.1080/09553008714552201.

[14] O. Ostling and K. J. Johanson, "Microelectrophoretic study of radiation-induced DNA damages in individual mammalian cells," *Biochem Biophys Res Commun*, vol. 123, no. 1, pp. 291–298, Aug. 1984, doi: 10.1016/0006-291X(84)90411-X.

[15] M. Klaude, S. Eriksson, J. Nygren, and G. Ahnström, "The comet assay: Mechanisms and technical considerations," *Mutation Research - DNA Repair*, vol. 363, no. 2, pp. 89–96, Jun. 1996, doi: 10.1016/0921-8777(95)00063-1.

[16] K. A. Yamauchi and A. E. Herr, “Subcellular western blotting of single cells,” *Microsystems & Nanoengineering 2017 3:1*, vol. 3, no. 1, pp. 1–9, Feb. 2017, doi: 10.1038/micronano.2016.79.
[17] I. Wittig and H. Schägger, “Features and applications of blue-native and clear-native electrophoresis,” *Proteomics*, vol. 8, no. 19. pp. 3974–3990, Oct. 2008. doi: 10.1002/pmic.200800017.
[18] I. Wittig, H. P. Braun, and H. Schägger, “Blue native PAGE,” *Nat Protoc*, vol. 1, no. 1, pp. 418–428, Jun. 2006, doi: 10.1038/nprot.2006.62.
[19] I. Wittig, T. Beckhaus, Z. Wumaier, M. Karas, and H. Schägger, “Mass estimation of native proteins by blue native electrophoresis: Principles and practical hints,” *Molecular and Cellular Proteomics*, vol. 9, no. 10, pp. 2149–2161, Oct. 2010, doi: 10.1074/mcp.M900526-MCP200.
[20] M. M. Camacho-Carvcajal, B. Wollscheid, R. Aebersold, V. Steimle, and W. W. A. Schamel, “Two-dimensional Blue Native/SDS gel electrophoresiss of multi-protein complexes from whole cellular lysates: A proteomics approach,” *Molecular and Cellular Proteomics*, vol. 3, no. 2, pp. 176–182, Feb. 2004, doi: 10.1074/mcp.T300010-MCP200.
[21] Q. Pan and A. E. Herr, “Geometry-induced injection dispersion in single-cell protein electrophoresis,” *Anal Chim Acta*, vol. 1000, pp. 214–222, Feb. 2018, doi: 10.1016/j.aca.2017.11.049.
[22] J. Vlassakis and A. E. Herr, “Joule Heating-Induced Dispersion in Open Microfluidic Electrophoretic Cytometry,” *Anal Chem*, vol. 89, no. 23, pp. 12787–12796, Dec. 2017, doi: 10.1021/acs.analchem.7b03096.
[23] Y. Wang, Q. Lin, and T. Mukherjee, “A model for Joule heating-induced dispersion in microchip electrophoresis,” *Lab Chip*, vol. 4, no. 6, pp. 625–631, 2004, doi: 10.1039/b406752e.
[24] A. J. Pfeiffer, T. Mukherjee, and S. Hauan, “Computer-Aided Synthesis of Microscale Electrophoretic Separation Systems in Confined Areas,” *American Society of Mechanical Engineers, Micro-Electromechanical Systems Division Publication (MEMS)*, vol. 5, pp. 15–24, May 2008, doi: 10.1115/IMECE2003-41289.
[25] J. Vlassakis, K. A. Yamauchi, and A. E. Herr, “Summit: Automated Analysis of Arrayed Single-Cell Gel Electrophoresis,” *SLAS Technol*, vol. 26, no. 6, pp. 637–649, Dec. 2021, doi: 10.1177/24726303211036869.
[26] L. T. Furcht and G. Wendelschafer-Crabb, “Trypsin-induced coordinate alterations in cell shape, cytoskeleton, and intrinsic membrane structure of contact-inhibited cells,” *Exp Cell Res*, vol. 114, no. 1, pp. 1–14, Jun. 1978, doi: 10.1016/0014-4827(78)90029-0.
[27] W. H. J. Westerhuis, J. N. Sturgis, and R. A. Niederman, “Reevaluation of the electrophoretic migration behavior of soluble globular proteins in the native and detergent-denatured states in polyacrylamide gels,” *Anal Biochem*, vol. 284, no. 1, pp. 143–152, Aug. 2000, doi: 10.1006/abio.2000.4684.
[28] D. Linke, “Chapter 34 Detergents: An Overview,” *Methods Enzymol*, vol. 463, no. C, pp. 603–617, Jan. 2009, doi: 10.1016/S0076-6879(09)63034-2.
[29] B. T. Arachea, Z. Sun, N. Potente, R. Malik, D. Isailovic, and R. E. Viola, “Detergent selection for enhanced extraction of membrane proteins,” *Protein Expr Purif*, vol. 86, no. 1, pp. 12–20, Nov. 2012, doi: 10.1016/J.PEP.2012.08.016.
[30] C. C. Kang, J. M. G. Lin, Z. Xu, S. Kumar, and A. E. Herr, “Single-cell western blotting after whole-cell imaging to assess cancer chemotherapeutic response,” *Anal Chem*, vol.

86, no. 20, pp. 10429–10436, Oct. 2014, doi: 10.1021/AC502932T/SUPPL_FILE/AC502932T_SI_001.PDF.
[31] A. J. Hughes, D. P. Spelke, Z. Xu, C. C. Kang, D. v. Schaffer, and A. E. Herr, "Single-cell western blotting," *Nat Methods*, vol. 11, no. 7, pp. 749–755, 2014, doi: 10.1038/nmeth.2992.
[32] S. Shah, S. Chakraborty, P. J. Hazarika, and M. M. Ali, "The Generalized-Alpha-Beta-Skew-Normal Distribution: Properties and Applications," Oct. 2019, doi: 10.48550/arxiv.1910.09192.
[33] E. Mahmoudi, H. Jafari, and R. Meshkat, "Alpha-Skew Generalized Normal Distribution and its Applications," *Applications and Applied Mathematics: An International Journal (AAM)*, vol. 14, no. 2, Dec. 2019
[34] J. Vlassakis *et al.*, "Measuring expression heterogeneity of single-cell cytoskeletal protein complexes," *Nature Communications 2021 12:1*, vol. 12, no. 1, pp. 1–14, Aug. 2021, doi: 10.1038/s41467-021-25212-3.
[35] A. Rogacs and J. G. Santiago, "Temperature effects on electrophoresis," *Anal Chem*, vol. 85, no. 10, pp. 5103–5113, May 2013, doi: 10.1021/ac400447k.
[36] C. Filep and A. Guttman, "Electromigration Dispersion in Sodium Dodecyl Sulfate Capillary Gel Electrophoresis of Proteins," *Anal Chem*, Sep. 2022,
[37] C. Filep and A. Guttman, "The Effect of Temperature in Sodium Dodecyl Sulfate Capillary Gel Electrophoresis of Protein Therapeutics," *Anal Chem*, vol. 92, no. 5, pp. 4023–4028, Mar. 2020,
[38] L. T. Furcht' and G. Wendelschafer-Crabb', "TRYPSIN-INDUCED COORDINATE ALTERATIONS IN CELL SHAPE, CYTOSKELETON, AND INTRINSIC MEMBRANE STRUCTURE OF CONTACT-INHIBITED CELLS."

Chapter 5: Formation of large-area, PDMS-polyacrylamide composite devices

5.1: Introduction

Development of novel device geometries and materials facilitate new functionality in microscale separation assays. The field of capillary electrophoresis (CE) has transformed as new technologies enabling novel geometry and materials have been invented. In CE systems, an electric field is applied to a microchannel or capillary to separate chemical or biological samples [1]. CE has undergone a transformation with microchip platforms replacing the original capillary formfactor [2]–[4]. In the new device designs, microchannels are embedded within materials such as glass or silicon substrates. Advantages of microfluidic CE includes fast analysis, high throughput, and integration capabilities with other microfluidic techniques [5], [6].

In addition to new geometries, CE has also benefitted from novel materials [7]. Often, glass is used as the supporting substrate for separation-based technologies. The optical clarity and well-characterized surface properties make glass a favored substrate. However, glass is often unsuitable for rapid prototyping of new devices and requires specialized equipment for etching processes. As an alternative to glass, polydimethylsiloxane (PDMS) has many of the same optical characteristics and is amenable to rapid prototyping, versatile geometries, and low-cost replication [8]–[10]. CE is carried out in free-flow buffer or polymer solutions, such as linear polyacrylamide [11] or within a gel matrix. A sieving gel functions as a non-convective medium and mitigates diffusional and convective problems within the channel. Conventionally, agarose or polyacrylamide gel (PAG) is cast inside the capillary or microchannel as a non-convective medium [12].

Like the innovation in CE techniques, new device designs and materials are necessary for other device geometries and improvements in the field of microscale separations. Open microfluidic offer facile loading of materials and samples, but have large surface areas that are partially open to the air. Whether for open- or closed-devices, the formation of PAG-PDMS devices is essential for innovation within the microscale separation field.

Thus, robust methods of generating devices with a combination of PDMS and polyacrylamide gel materials are desired. PAG-PDMS devices are to challenging to fabricate because PDMS is highly permeable to oxygen and thus poorly suited for radical polymerization of the gels [13]–[16]. Furthermore, for robust microfluidic devices, it is desired that the two materials are attached covalently. Material discontinuities can exacerbate sample injection and convection within the device.

To form robust PDMS-polyacrylamide gel (PDMS-PAG) microdevices, two conditions must be met: 1) Oxygen must be depleted to permit polymerization of the PAG, and 2) Material connections must be made between PDMS and PAG. Previously, the UV-reactive benzophenone (BP) species was identified as capable of satisfying both criteria [17]–[21]. For the first criterion, BP acts as an oxygen scavenger at sufficiently high concentrations upon UV exposure. BP will continue to do so until oxygen is depleted and PDMS radicalization through hydrogen abstraction can start (step 2). For the second criterion, composite polyacrylamide-silicone

substates can be formed by incorporating interpenetrating networks of polyacrylamide hydrogens onto the silicone membrane. Benzophenone participates in graft photopolymerization surface modification schemes to attach functional groups to the PDMS surface via covalent bonding, using ultraviolet light as an energy source [22]. UV irradiation is combined with a photoinitiator to generate free radicals and create sites for graft polymerization from the otherwise chemically inert PDMS surface and to handle electron chain transfer during polymerization of the PAG. The use of BP to create PDMS-PAG composite devices has previously been reported for the formation of featureless gels [23] and gels inside of PDMS channels for use in CE. Yet, the application of this method for the formation of larger geometries and open microfluidic device configurations is unclear. Here, we focus on the formation of a PAG on top of PDMS. In this case, oxygen is more readily available, the design has a larger surface area, and the PDMS-PAG bond is exposed.

We sought a strategy for permanent generation of PDMS-PAG interfaces. Specifically, large-area interfaces that contain microfeature patterns in the PAG layer, such as those used for single-cell western blotting [24], [25]. We report the development of a method for polymerizing polyacrylamide atop PDMS substrates for two-layer device geometries for microscale electrophoretic separations. To overcome oxygen inhibition of gel polymerization, we introduce benzophenone into the PDMS. During polymerization by UV, benzophenone forms radicals that scavenge available oxygen. We evaluate both photomask and micro-mold means of establishing microwell geometries in the polyacrylamide gel for downstream implementation for separation science. We characterize the sieving performance of the resulting PDMS-polyacrylamide open device from single cells. The methods shared in this chapter preface innovation in two-layer device layouts for array- and microwell-based systems.

5.2: Methods

SU-8 wafer: The SU-8 wafer used to fabricate micro-patterned gels were fabricated as previously published [25], [26]. The microwells were designed to be 50 µm in diameter and 50 µm in height. The well spacing was 1 mm along the separation axis and 0.5 mm in the transverse axis. The silicon wafer was treated with dicholoromethylsilane prior to use. Mylar masks for both SU-8 wafer and photopatterned gel geometries were printed by Artnet Pro.

PDMS substrate: Standard glass slides were cleaned with methanol and dried for 2 minutes at 200 °C. A ~75-100 µm layer of 10:1 base:curing agent polydimethylsiloxane (PDMS) was cast on the cleaned slides by spin coating (2500 rpm for 1 minute, 600 rpm/s acceleration). PDMS was cured overnight at 80 °C. Before use, PDMS substrates were cleaned with water and dried with N_2 stream. PDMS substrates were stored in a sealed container for up to 3 months. Before use, PDMS substrates were scored and broken into half-microscope slides, with final dimensions of 1 x 1.5 inches.

To functionalize the PDMS with benzophenone (BP), we prepared a solution of 10% (w/v) benzophenone dissolved in acetone solution and incubated a PDMS-coated microscope slide in the solution for 30 minutes. The substrate was washed in pure methanol and then deionized water, before being dried with nitrogen stream [27].

PAG gel formation: For photopolymerization, the polyacrylamide gel precursor contained 8%T acrylamide/bis-acrylamide, 3 mM BPMAC with 0.2% VA-086 in water. This is considered the 'standard' UV polymerized gel type and was used for device fabrication unless stated otherwise. The polyacrylamide gels were polymerized by ultraviolet light (λ = 365 nm, 20 mW/cm^2) after degassing and sonication to remove air from the solution. For chemical polymerization, the VA-086 crosslinker was replaced by 0.8% APS and 0.5% TEMED, and gels allowed to polymerize for 15 minutes. Degassing steps were consistent regardless of method and gel formula used.

Composite device formation: For featureless gels, the precursor was introduced between a hydrophobic glass slab (treated with GelSlick) and the PDMS substrate. For gels with microscale wells, the precursor was introduced between either a SU-8 mold and the PDMS substrate (for physical mold patterning) or between a hydrophobic glass slab with a photomask containing the pattern for the microfeatures and the PDMS substrate. After polymerization, the unpolymerized PA is washed from the wells for 10 minutes in 1X PBS.

Protein decoration of PAG-PDMS device: After preparation of the BP-containing PDMS substreeate as described above, the PDMS was incubated with 6 μg/mL solution of rhodamine-fibronectin, unless stated otherwise. The PDMS substate was washed in deionized water trice and dried with nitrogen stream prior to imaging and subsequent PAG decoration by UV. The fluorescence rhodamine signal was quantified. Here, fluorescence intensity positively correlates to fibronectin concentration.

scWB operation: Single-cell western blot (scWB) protocol was executed as per previously published with, with minimal changes to the protocol [25]. In short, BJ fibroblast cells suspended in phosphate-buffered saline (PBS) were pipetted on top of the device and cells allowed to settle into the microwells for 10 minutes by gravity before washing. 1 mL of PBS was applied to each edge of the device to remove excess cell, leaving only the cells in the microwells. The device was transferred to a 3D printed electrophoresis chamber. The cells were lysed in-well with 2X RIPA buffer for 20 seconds, and size-based electrophoretic separation was executed at 40 V/cm for 25 seconds. Devices were rinsed overnight in 1X TBST. For immunoprobing, the gels were probed according to standard protocols for actin and CD44. In short, primary antibody solution was introduced at a 1:10 stock dilution and incubated for 2 hours. After being washed in 1X TBST twice, secondary antibody solution was introduced at 1:20 stock dilution for 1 hr. The devices were washed, dried, and imaged with a microarray scanner.

5.3: Results

Generation of large-area composite devices with PAG atop PDMS

Two-layer composite devices of polyacrylamide and PDMS enable new microfluid chip configurations. In agreement with expectations, we observed even a thin layer of PDMS (~75 μm height) contains enough O_2 to prevent polymerization of polyacrylamide, even with extended polymerization times, regardless of polymerization scheme. Both photo- and chemical-polymerization was tested. Thus, to enable polymerization of polyacrylamide, reactive oxygen species must either be removed from the environment or scavenged and eliminated as a reactive partner by abstraction. For the former method, polymerization can be carried out in an inert gas environment. We tested the process of casting polyacrylamide gels on PDMS inside a nitrogen

environment. The PDMS substrate was stored in the nitrogen environment for 10 minutes prior to polymerization to evacuate oxygen species from the bulk material. Using chemical polymerization, 8%T gel was polymerized between the PDMS and a glass slide for 15 minutes. We observed polymerization of the gel within 10 minutes of chemical initiation when the O_2 is purged and replaced with nitrogen, and no polymerization in the oxygen environment. However, as the PDMS regains its bulk hydrophobic characteristics and O_2 permeates the material, the two layers delaminate. To produce robust, composite devices, the two layers should form an interpenetrating network.

Previously, benzophenone (BP) has been used to graft polyacrylamide to PDMS [27]. In addition to scavenging oxygen species and permitting polymerization, BP also grafts the polyacrylamide to the PDMS. To form a composite network of acrylamide and silicone, the silicone is impregnated with the UV-reactive BP and a polyacrylamide gel is subsequently UV-polymerized onto the surface [28], [29]. This has been demonstrated in other geometries and in small-area thin films, with geometries in the range of 10 - 1000s μm [23], [30]. However, to be compatible with open microfluidic devices, this method must be optimized for use in geometries with greater surface area. Large area PDMS-PAG structures are challenging as the oxygen sink along the PDMS surface is constantly replenished by fresh oxygen diffusing in from the surrounding, both by diffusion through the bulk PDMS as well as through the monomer solution. With the larger surface area (compared to enclosed microchannels of CE), establishing oxygen depletion and PAG polymerization requires tuning of BP protocols. In addition, the additional surface area of such geometries compared to the microchannel complicates the surface forces and heat transfer rates of the system.

To establish a protocol for generating a PDMS-PAG layered device, we started by testing the bonding of feature-less polyacrylamide on top of PDMS. PDMS substrates were incubated with benzophenone prior to use. Polyacrylamide gel precursor is introduced between the PDMS substrate, and a secondary glass slab treated with GelSlick to facilitate gel release post-polymerization. The gel polymerized and benzophenone was activated by UV simultaneously. We observed polymerization starting at 30 seconds and no polymerization in the negative control (no benzophenone). Optimal polymerization dose for a 8%T polyacrylamide gel (0.2% VA-086) was determined to be 2.4e4 J/m^2. Compared to polymerization in channels, which has been reported to be complete at a dose of 7.2e4 – 1.1e5 J/m^2 [31], [32], the planar geometry tested here required significantly lower dose for complete polymerization. At high UV doses, we observed the formation of bubbles inside of the gel, compromising the structural integrity and pore size of the PAG.

Applications in single-cell array and cell culture technology require geometric control of the PAG layer. In single-cell array assays, such as the single-cell western blot and isoelectric focusing systems, cells are settled into microwells within a PAG prior to electrophoretic separation. The two-layer platform introduced here permits microwell designs with PDMS at the base of the well. For cell culture studies, the generation of PAG geometries has been shown to control cell growth in mechanobiology studies [28]. Thus, we expanded on the method above to generate PDMS-PAG structures with patterns and micro-geometries in the PAG. We evaluated two main paths for constructing the composite chips using UV-induced polymerization and patterning by either: 1. Photomask patterning, or 2. Physical mold patterning. Photomask patterning is compatible with the use of UV polymerization of the PAG and activation of the BP.

The generation of small features by UV-polymerization relies on a photomask and is limited by the diffusional limit of activated monomers. In comparison, physical molds are often used with chemical polymerization strategies. Physical mold patterning is superior in its ability to generate high-resolution microscale features. Previously, microwell PAGs have been cast on a SU-8 coated silicon wafer with chemical polymerization [26], [33]. The wafer contains micropillars generated by standard lithography methods.

We found that photopatterning of features by UV-polymerization was limited in the generation of small features in PAG. Using an inversed photomask with microwells of varying sizes (diameter = 30, 50, 100, 200, and 500 μm), PDMS-PAG composite devices were fabricated using the same procedure as summarized above. Here, the polyacrylamide functioned as a negative photoresist: Exposure to UV light crosslinks the polymer. With optimized polymerization strategy, microfeatures with diameters of 100 μm and up were resolvable by brightfield fluorescence microscopy. Thus, the diffusion/diffraction limits of generating small features with UV-polymerization and a photomask is sufficient for >100 μm diameter features.

To achieve smaller feature sizes, we implemented a physical mold alongside UV polymerization. Similar methods have been developed previously to generate microwells in gradient gels established by UV polymerization [34]. Here, we circumvented the use of a glass-SU8 mold by inverting the system to have a standard silicon wafer with the micropattern facing down (**Figure 5.1**), as optical clarity of the system is less crucial because the methods does not require an alignment step. A silicon wafer with micropillar pattern (diameter = 50 μm) was situated on top of the PDMS substrate with the micropillar array facing down. It is important to note that the use of GelSlick is not advised for PDMS-polyacrylamide composite devices, as the product contains a PDMS derivate that we anticipate will crosslink to the PDMS when benzophenone-based conjugation is used. The assembly was exposed to UV for 90 seconds (20 mW/cm2). The assembly was taken apart using a razor blade to pry the gel from the wafer.

We observed large irreproducibility issues with the method once we introduced micron-sized features in the PAG. The PAGs were properly bound to the PDMS and polymerized, but the PAG ripped longitudinally when removed from the wafer (50% success rate, N = 15) (**Figure 5.2A**). The control (no features, cast against a glass slide) polymerized and released from the mold as expected. To mitigate the fabrication failure mode of incomplete gel release from the master mold, we explored a range of protocol parameters, including UV dose, pore size and gel structural integrity, mold coatings, and mold types (**Table 5.1**).

First, we investigated the effect of decreasing the UV dose. Enough UV must be supplied for benzophenone activation and VA-086 crosslinking of polyacrylamide. However, excessive UV exposure could contribute to gel adhesion to the mold and difficulty demolding as the precursor is heated and liquid evaporated. We observed that at exposure times less than 60 seconds, the BP-mediated crosslinking of the PDMS and PAG is incomplete. Below 20 seconds, the polyacrylamide gel does not polymerize. We found that 85 second UV exposure at 20 mW/cm^2 was the optimal condition for both polymerization of the PAG and crosslinking of the PDMS-PAG when using a physical mold to generate microfeatures in the PAG layer.

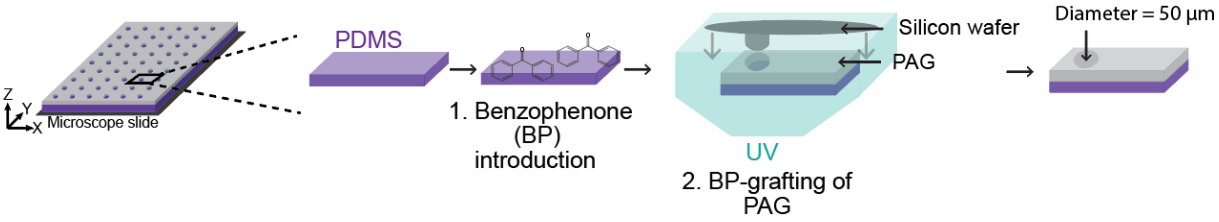

Figure 5.1: Workflow schematic for generation of PDMS-PAG composite devices with <100 µm features with benzophenone grafting, UV-polymerization, and physical mold. A microscope-slide sized composite device was made by casting a gel atop PDMS coated microscope slide. 75 µm PDMS height was used for this study. The main steps the process of creating fused PAG-PDMS devices includes: 1) impregnation of the PDMS with UV-reactive benzophenone, and 2) BP-grafting and polymerization of the PAG onto the PDMS. The PAG precursor was sandwiched between the PDMS substrate and a silicon wafer with the desired geometries in SU-8 facing the PDMS substrate. When using an inverted UV source, the assembly stack included (in the order of bottom-to-top): UV light source, PDMS substrate, PAG precursor, and reversed-oriented silicon wafer. After polymerization, the assembly is disassembled, leaving an array of microfeatures in the PAG layer atop the PDMS.

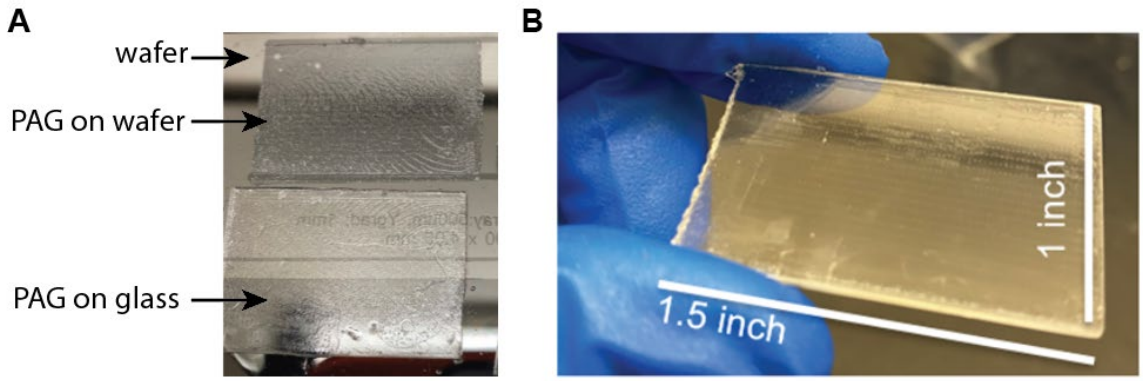

Figure 5.2: Common failure mode of PDMS-PAG devices with microfeatures. A. After polymerization of the gel, we observed the gel to tear lengthwise upon demolding using the same protocol as that to generate featureless PDMS-PAG devices. Representative photograph of failure mode shows half a microscope slide (1.5 x 1 inch) with gel on both the PDMS substrate (bottom) and the SU-8 wafer (top). **B**. Optimized fabrication conditions generate robust two-layer devices 50% of the time. Microwell array is visible in the PAG layer, which is covalently bonded to the base layer of PDMS to create a cohesive device.

Next, we hypothesized that the structural integrity of the PAG section of the two-layer device was compromised to a point of failure with the introduction of the microwell array because of the additional topography and surface area of the microwells. To test this hypothesis, we increased the %T of the gel from 8% to 10%. The improved structural integrity of the gel because of a pore size decrease did not improve the success rate of production. We also incorporated Rhinohide, a commercial polyacrylamide gel strengthener that is recommended for gels subject to multiple handling steps. Rhinohide was incorporated into the gel precursor at a final concentration equal to 20% of the acrylamide amount. Again, no change was observed in the success rate of production. We concluded that the tearing of the PAG is not a result of poor structural integrity of the gel.

Poor device yield was remedied to give ~50% success rate in fabrication with micropatterns in the PAG, with all failure stemming from the single failure mode of PAG splitting during demolding. The best conditions for polymerizing PAG onto PDMS with BP in cases where small features are desired in the PAG were determined to be: an 8%T gel exposed for 85 s with 20 mW/cm^2 UV intensity while in contact with an SU-8 mold created on a silicon wafer by standard lithography methods (**Figure 5.2B**). The SU-8 mold was treated with dichloromethylsilane prior to use. Once formed, the devices are stable for > 3 months when stored dehydrated. This exceeds common requirements for bioassays involving stripping and reprobing [35] and on-chip culture devices, such as organ-on-a-chip and 3D cell culturing [36]–[38].

Table 5.1: Fabrication settings for the generation of large-area, PDMS-PAG devices with microfeatures in the PAG layer. All PAG precursors contain 0.2% VA-086. PDMS substrate (if used), was treated with 10% BP prior to UV-activation. Glass substrates controls were not treated with benzophenone. Fabrication success rate was determined by visual inspection of device generated. A device was deemed unsuccessful if the PAG failed to polymerize, or the PAG was torn longitudinally during demolding. Success rate was calculated based on N > 5.

	Gel %T	**UV Exposure time (20 mW/cm^2)**	**Other**	**Substrate**	**Mold**	**Fabrication success rate**
Features Optimized	8	85	Silanization of mold	PDMS	Su-8 on silicon, micropillars	50%
No features Optimized	8	85	Silanization of mold	PDMS	Glass slab with tape rails	95%
Exposure time	8	15		glass	Su-8 on silicon, micropillars	0% Not polymerized
	8	20		Glass	Su-8 on silicon, micropillars	0% Not polymerized
	8	30		Glass	Su-8 on silicon, micropillars	0%
	8	40		Glass	Su-8 on silicon, micropillars	0%
	8	60		Glass	Su-8 on silicon, micropillars	30%

	8	80		Glass	Su-8 on silicon, micropillars	50%
Structural integrity	12	80	No rhinohide	PDMS	Su-8 on silicon, micropillars	0%
	8	80	Rhinohide	PDMS	Su-8 on silicon, micropillars	0%
	12	80	No rhinohide	glass	Su-8 on silicon, micropillars	0%
	8	80	Rhinohide	glass	Su-8 on silicon, micropillars	0%
Coatings	8	85	BlueSlick of mold	PDMS	Su-8 on silicon, micropillars	0%
	8	85	gelSlick + Silanization	PDMS	Su-8 on silicon, micropillars	0%
	8	85	gelSlick of mold	PDMS	Su-8 on silicon, micropillars	0%
Wafer Substrate (silicon and glass)	8	85	Silanization of mold	glass	Su-8 on glass, micropillars	15%
	8	85	Silanization of mold	PDMS	Su-8 on glass, micropillars	0%

Single-cell electrophoretic separation with PDMS-PAG device

One potential use for this two-layer device geometry is for separation of proteins from single cells situated in the microwells. The underlying PDMS structures can be used for on-chip culture prior to cellular lysis or for the generation of an integrated microchannel delivery system for small molecule drugs or other cellular stimulators. To test the sieving properties of the polyacrylamide gel when joined to PDMS and the effect of the PDMS layer on immunoprobing, we employed the two-layer device for single-cell western blotting (scWB).

We separated protein from single cells and used immunoreagents to specifically detect actin and CD-44 proteins on the two-layer device by immunoblotting. Device fabrication proceeded as described above, using the method with the highest device yield to create devices with 50 μm diameter microwells in the PAG (8%T, 0.5% VA-086) atop the PDMS (**Figure 5.3A-B**).

We found that polyacrylamide gel electrophoresis on PDMS substrates resulted in longer migration distance, corresponding to a faster migration velocity of actin, than on PAG devices without PDMS (average of 648 μm of N = 75 and 584 μm of N = 35, for PDMS-PAG and PAG only devices, respectively) (**Figure 5.3C**). We hypothesize that the greater migration velocity of actin in the PDMS-PAG system stems from inefficient oxygen scavenging from the benzophenone during device polymerization, resulting in the generation of a high-porosity gel.

One the main drawbacks of using PDMS for cell biology is that PDMS can absorb small hydrophobic molecules like biomolecules and drugs from solution [39]. Non-specific adsorption of protein in a scWB-style assay during immunoprobing would result in high background levels and a correspondingly poor limit of detection. Based on literature, a commonly used method for

blocking the adsorption of proteins involves immobilizing hydrophilic and neutrally charged polymers to protect the surface [40]. For example, surface-initiated polymerization (such as that used to graft the PDMS-PAG) produces polymer brushes at the surface. Goda et al. grafted 2-methacryloyloxyethyl phosphorylcholine (MPC) to PDMS by surface-initiated photo-induced radical polymerization using benzophenone as an initiator. They show that the modified PDMS surfaces possessed an excellent surface hydrophilicity and anti-biofouling property [41]. We hypothesized that the polyacrylamide attached at the surface of PDMS would function as polymer brushes to decrease nonspecific absorption of antibody onto the PDMS during immunoprobing. We found that the protein adsorption onto PDMS was 20-fold higher than that onto PDMS-PAG. For scWB, the fluorescence intensity of actin protein signal was significantly higher on the PAG-only device compared to that of the composite device (**Figure 5.3D**). Yet the two devices have comparable signal-to-noise ratios (SNR, SNR_{PAG} = 69, $SNR_{PDMS\text{-}PAG}$ = 58) Here, comparable SNRs permit equal detection of proteins above the background noise level. Thus, the addition of a PDMS substrate layer to the PAG-based scWB assay does not inhibit detection of proteins by on-chip immuno-detection of the target.

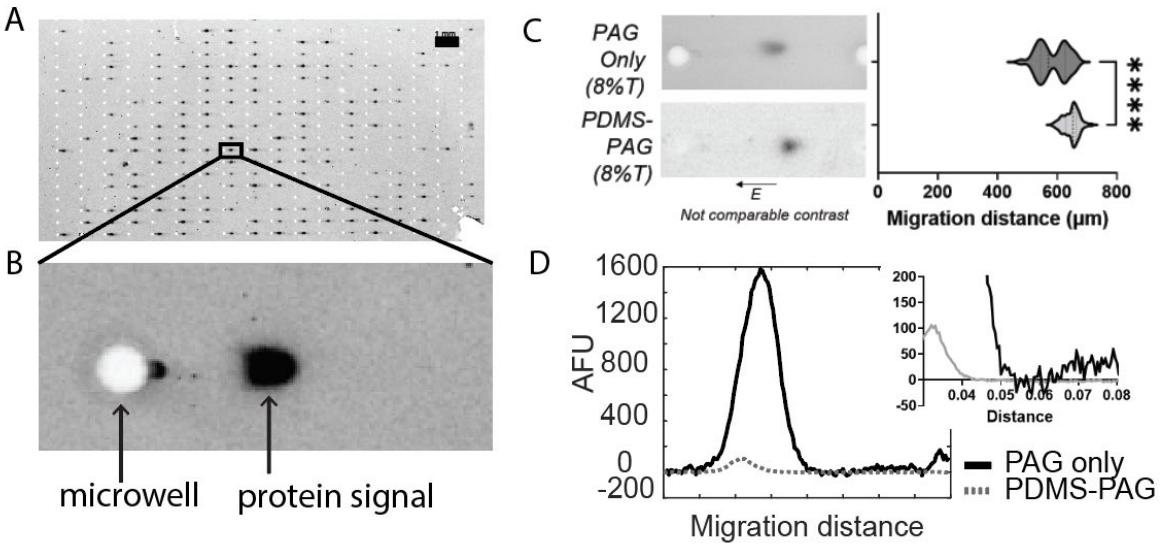

Figure 5.3: Separation of proteins from single cells on PDMS-PAG devices. BJ fibroblast cells were lysed on chip and proteins were separated based on size using electrophoretic sieving within the PAG. (A) false-color micrograph of 25% of the sample slide post-immunoprobing. Scale bar = 50 μm. (B) False-color micrograph of representative CD44 protein abundance for one single-cell separation. The fluorescence intensity of the protein signal correlates to protein abundance. (C) Representative micrographs of actin signal in PAG only (top) and PDMS-PAG (bottom) devices. Violin plot shows significantly different migration distance, with greater actin electrophoretic velocity in the PDMS-PAG device ($P < 0.05$). (D) Intensity profile for actin immunoprobed signal for the PAG (solid line) and PDMS-PAG devices (dotted line) for a representative single-cell separation. Cutout zoom focuses on the signal-to-noise ratio. All separation lanes are 1 mm in length.

Two-step, BP-immobilization of proteins

One desired application of two-layer composite device is for on-chip culture of cells. This includes the interrogation of cell response to material stiffness or the generation of geometrically constrained cultures of cells. Cells can be seeded on either the PDMS layer or polyacrylamide layer depending on desired stress/strain response of the material [42], [43]. However, cells membranes do not directly bind to the surfaces of hydrogels, PDMS devices, or other material surfaces due to material hydrophobicity [40]. Instead, varying types of extracellular matrix (ECM) protein stably bind to specific classes of cell transmembrane proteins and link them to surfaces, triggering cell-surface interactions [44]. Coating the PDMS with the glycoprotein fibronectin or other ECM proteins allows cell adhesion and (with enough time) proliferation [45]. Here, we investigated the active capture of fibronectin by benzophenone as a model protein because of its relevance to ECM studies.

Benzophenone can be used for active capture and immobilization of proteins. Previous work has demonstrated the generation of glass substrates with BP-reactive groups conjugated to it for subsequent protein capture with UV (30 s exposure, 14 mW/cm) [46] [47] [48]. In this work, protein is photo-immobilized onto the PDMS substrate simply by BP as a photochemical linker. We anticipated that fibronectin can participate in the photochemical reaction of BP with sterically accessible side chains of amino acids [49]. The main concern with this double-capture hypothesis was the availability of radicals on the protein to participate as binding partner with the substrate radical after benzophenone activation. Photo-grafting by Norrish Type II initiation systems (i.e. BP) is commonly done in combination with elastomers, graphene oxide, acrylamide, poly(acrylic acid) or other vinyl monomers [50]. These species have double-bonded carbon that participates in the reaction with the elastomer network (methacrylate group) after activation. In comparison, fibronectin does not have any vinyl monomers based on common amino acid structures. Protein radicals are often the result of oxidation of amino acids in the presence of UV light [51]. It is possible to generate a carbon-centered radical by the oxidation of protein backbone in the presence of reactive oxygen species [52] [53]. This radical carbon most closely mimics that of the vinyl monomers and is likely to exists in our system after UV exposure. Additional radicals are possible along the amino acid chains.

We hypothesized that benzophenone can be used to capture fibronectin onto the substrate prior to the introduction of the acrylamide monomer for polyacrylamide grating. We propose the two-step generation of a fibronectin-functionalized PDMS-PAG interface (**Figure 5.4A**). First, silicone is impregnated with UV-reactive BP. Fibronectin is grafted onto surface upon UV-activation and generation of protein radicals. Lastly, aqueous PAG precursor solution is introduced and UV-polymerized onto the surface with secondary round of UV-grafting. Here, Norrish type II reaction is beneficial since BP is not depleted by UV exposure directly but only those molecules which undergo a reaction with a reaction partner are consumed. Therefore, for BP at sufficiently high concentration, depletion effects become negligible (**Figure 5.4B**), and sequential activation and reaction can be achieved.

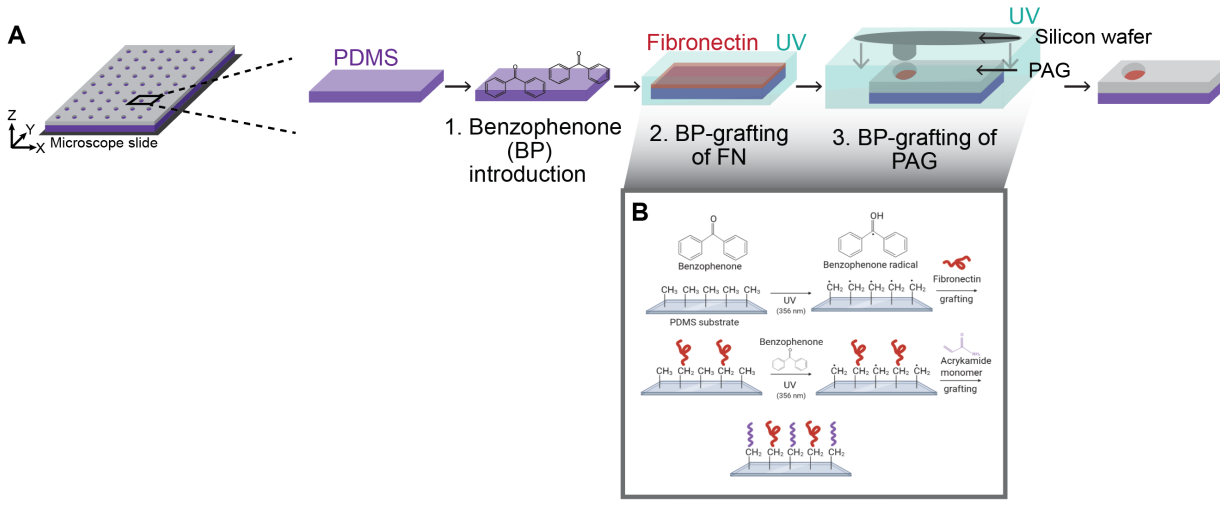

Figure 5.4: Schematic of the proposed workflow for grafting protein and polyacrylamide to PDMS simultaneously. Fibronectin decoration of the PDMS substrate can be done before casting the polyacrylamide layer. We hypothesized that dual functionality can be achieved by stepwise grafting of fibronectin and polyacrylamide onto the PDMS. (**A**) The workflow starts with benzophenone-impregnated PDMS incubated with fibronectin and exposed to UV for capture. The fibronectin solution is removed, and the device washed. The PDMS substrate is then layered with PAG precursor and microfeature mold as described earlier for the subsequent UV-mediated grafting of polyacrylamide onto the same PDMS surface for covalent interface bonds between the two polymers. (**B**) The grating technique utilizes the excess benzophenone to split the reactive benzophenone population in half and allow two sequential captures.

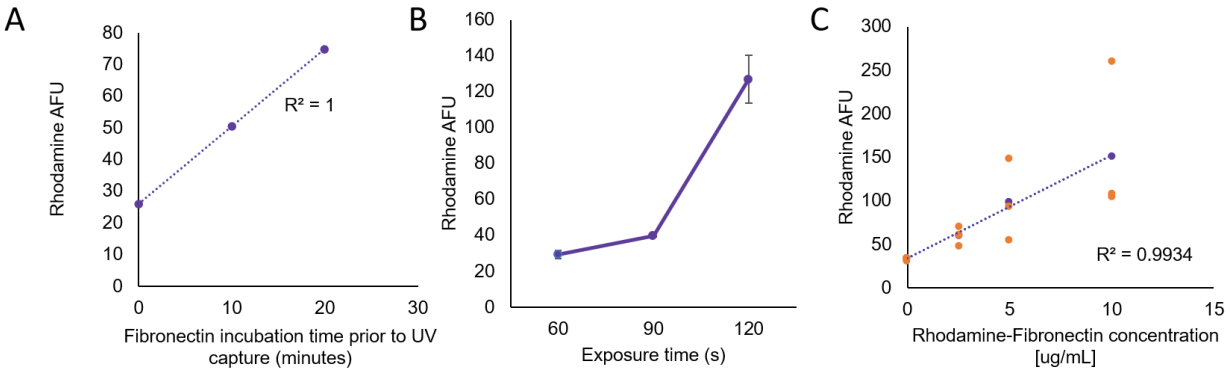

Figure 5.5: Fibronectin decoration of the PDMS substate prior to PAG patterning by benzophenone-medicated grafting is dependent on UV dose, exposure time, and protein concentration. (**A**) fibronectin incubation time prior to UV capture correlates to captured rhodamine-fibronectin (N = 3). (**B**) Immobilized rhodamine-fibronectin concentration increases with increasing UV dose (N = 3). (**C**) Increasing the initial rhodamine-fibronectin concentration causes a matching increase in the captured protein amount (N = 3).

First, we found that the substrate must be incubated with the fibronectin prior to UV capture for detectable signal. A longer incubation period resulted in a brighter signal (**Figure 5.5A**). A brighter signal correlates to higher fibronectin decoration. We hypothesized that more fibronectin molecules diffuse into the PDMS during longer incubation times, enabling more contact with the benzophenone that is embedded in the PDMS. To be linked to the PDMS, the fibronectin must be in proximity to a reactive benzophenone species. Next, we found the fibronectin concentration on the PDMS substate was dependent on UV dose (**Figure 5.5B**). While proteins can be adsorbed onto PDMS nonspecifically due to the material properties, the positive correlation between UV dose and fluorescence suggested that fibronectin is being actively captured in a benzophenone-activated manner. Lastly, at constant UV exposure, captured fibronectin concentration scales with the applied fibronectin concentration (**Figure 5.5C**). This shows that, at the fibronectin concentrations tested here, the concentration of benzophenone from a 10% solution on a ~10 cm^2 PDMS substrate is in excess. All PDMS substrates were used for subsequent PAG polymerization. The polymerization of PAG atop the fibronectin-decorated PDMS proved BP in excess for stepwise grafting of multiple species

5.4: Conclusion

We investigate a method to generate large-surface, bonded PAG and PDMS devices. Large film PDMS-polyacrylamide structures enable new geometries and material combinations of microfluidic devices. We characterized the formation of composite polyacrylamide-silicone substrates with UV-mediated, free-radical polymerization by benzophenone. Large-area substrates (>10 cm^2) with PAG atop of PDMS was created by the formation of composite network of acrylamide and silicone. The protocol was amenable to microscale features in the PAG larger than 100 μm by photopolymerization, and smaller than 100 μm by physical molding. With increasing gel topography, we observed decreasing fabrication success rate. The use of benzophenone to generate a composite device enabled covalent attachment of protein for bio-functional PDMS substrates. This is particularly of interest for extracellular matrix patterning within the microwells for on-chip culture systems. We showed that active capture of fibronectin by benzophenone onto PDMS can be modulated by UV dose. The binding of protein with benzophenone did not inhibit the subsequent binding of PAG.

Looking forward, we anticipate that the findings reported here can pave the way for PDMS-channel geometry interfaced with arrayed polyacrylamide features. The controlled delivery of reagents by PDMS microchannels to individually trapped cells in polyacrylamide microwells would enable multiplexed drug or stressor studies on a single microfluidic chip. It could also be used to extract and/or deliver reagents for bioassays, such as PCR or sequencing.

5.5: References

[1] C. W. Huck and G. K. Bonn, “Analysis of Proteins by Capillary Electrophoresis.”

[2] M. Fu, J.-C. Leong, C.-F. Lin, C.-H. Tai, and C.-H. Tsai, “High performance microfluidic capillary electrophoresis devices”, doi: 10.1007/s10544-007-9049-3.

[3] I. Ali, O. M. L. Alharbi, and M. Marsin Sanagi, “Nano-capillary electrophoresis for environmental analysis,” *Environmental Chemistry Letters*, vol. 14, no. 1. Springer Verlag, pp. 79–98, Mar. 01, 2016. doi: 10.1007/s10311-015-0547-x.

[4] R. Bharadwaj, J. G. Santiago, and B. Mohammadi, “Design and optimization of on-chip capillary electrophoresis,” *Electrophoresis*, vol. 23, no. 16, pp. 2729–2744, Aug. 2002,

[5] X. Ou, P. Chen, X. Huang, S. Li, and B. F. Liu, “Microfluidic chip electrophoresis for biochemical analysis,” *J Sep Sci*, vol. 43, no. 1, pp. 258–270, Jan. 2020, doi: 10.1002/JSSC.201900758.

[6] M. Dawod and D. S. Chung, “High-sensitivity capillary and microchip electrophoresis using electrokinetic supercharging,” *J Sep Sci*, vol. 34, no. 20, pp. 2790–2799, Oct. 2011, doi: 10.1002/JSSC.201100384.

[7] Y. Li, J. S. Buch, F. Rosenberger, D. L. DeVoe, and C. S. Lee, “Integration of Isoelectric Focusing with Parallel Sodium Dodecyl Sulfate Gel Electrophoresis for Multidimensional Protein Separations in a Plastic Microfludic Network,” *Anal Chem*, vol. 76, no. 3, pp. 742–748, Feb. 2004, doi: 10.1021/AC034765B.

[8] S. K. Sia and G. M. Whitesides, “Microfluidic devices fabricated in Poly(dimethylsiloxane) for biological studies,” *Electrophoresis*, vol. 24, no. 21, pp. 3563–3576, Nov. 2003, doi: 10.1002/ELPS.200305584.

[9] J. W. Hong, K. Hosokawa, T. Fujii, M. Seki, and I. Endo, “Capillary gel electrophoresis on a disposable PDMS (polydimethylsiloxane) microchip,” *Annual International Conference of the IEEE Engineering in Medicine and Biology - Proceedings*, vol. 2, p. 728, 1999, doi: 10.1109/IEMBS.1999.803883.

[10] C. S. Effenhauser, G. J. M. Bruin, A. Paulus, and M. Ehrat, “Integrated Capillary Electrophoresis on Flexible Silicone Microdevices: Analysis of DNA Restriction Fragments and Detection of Single DNA Molecules on Microchips,” *Anal Chem*, vol. 69, no. 17, pp. 3451–3457, Sep. 1997, doi: 10.1021/AC9703919.

[11] G. Chen, H. Bao, J. Li, and D. Chen, “Fabrication of Poly(dimethylsiloxane)-Based Capillary Electrophoresis Microchips Using Epoxy Templates,” *Microchimica Acta 2005 153:3*, vol. 153, no. 3, pp. 151–158, Nov. 2005, doi: 10.1007/S00604-005-0436-2.

[12] J. W. Hong, K. Hosokawa, T. Fujii, M. Seki, and I. Endo, “Microfabricated Polymer Chip for Capillary Gel Electrophoresis,” *Biotechnol Prog*, vol. 17, no. 5, pp. 958–962, Jan. 2001, doi: 10.1021/BP010075M.

[13] S. C. Ligon, B. Husár, H. Wutzel, R. Holman, and R. Liska, “Strategies to reduce oxygen inhibition in photoinduced polymerization,” *Chem Rev*, vol. 114, no. 1, pp. 577–589, Jan. 2014, doi: 10.1021/CR3005197.

[14] D. Dendukuri, P. Panda, R. Haghgooie, J. M. Kim, T. A. Hatton, and P. S. Doyle, “Modeling of oxygen-inhibited free radical photopolymerization in a PDMS microfluidic device,” *Macromolecules*, vol. 41, no. 22, pp. 8547–8556, Nov. 2008, doi: 10.1021/MA801219W/SUPPL_FILE/MA801219W_SI_001.PDF.

[15] A. K. O'Brien and C. N. Bowman, "Impact of oxygen on photopolymerization kinetics and polyme structure," *Macromolecules*, vol. 39, no. 7, pp. 2501–2506, Apr. 2006, doi: 10.1021/MA051863L.
[16] C. Decker and A. D. Jenkins, "Kinetic Approach of o2 Inhibition in Ultraviolet and Laser-Induced Polymerizations," *Macromolecules*, vol. 18, no. 6, pp. 1241–1244, 1985, doi: 10.1021/MA00148A034.
[17] C. S. Simmons, A. J. S. Ribeiro, and B. L. Pruitt, "Formation of composite polyacrylamide and silicone substrates for independent control of stiffness and strain," *Lab Chip*, vol. 13, no. 4, pp. 646–649, 2013, doi: 10.1039/c2lc41110e.
[18] D. Keskin, T. Mokabbar, Y. Pei, and P. van Rijn, "The relationship between bulk silicone and benzophenone-initiated hydrogel coating properties," *Polymers (Basel)*, vol. 10, no. 5, May 2018, doi: 10.3390/polym10050534.
[19] N. de Smet, M. Rymarczyk-Machal, and E. Schacht, "Modification of polydimethylsiloxane surfaces using benzophenone," *J Biomater Sci Polym Ed*, vol. 20, no. 14, pp. 2039–2053, Oct. 2009, doi: 10.1163/156856208X397901.
[20] G. Dormán, H. Nakamura, A. Pulsipher, and G. D. Prestwich, "The Life of Pi Star: Exploring the Exciting and Forbidden Worlds of the Benzophenone Photophore," *Chemical Reviews*, vol. 116, no. 24. American Chemical Society, pp. 15284–15398, Dec. 28, 2016. doi: 10.1021/acs.chemrev.6b00342.
[21] M. H. Schneider, Y. Tran, and P. Tabeling, "Benzophenone absorption and diffusion in poly(dimethylsiloxane) and its role in graft photo-polymerization for surface modification," *Langmuir*, vol. 27, no. 3, pp. 1232–1240, Feb. 2011, doi: 10.1021/la103345k.
[22] M. H. Schneider, Y. Tran, and P. Tabeling, "Benzophenone absorption and diffusion in poly(dimethylsiloxane) and its role in graft photo-polymerization for surface modification," *Langmuir*, vol. 27, no. 3, pp. 1232–1240, 2011, doi: 10.1021/la103345k.
[23] C. S. Simmons, A. J. S. Ribeiro, and B. L. Pruitt, "Formation of composite polyacrylamide and silicone substrates for independent control of stiffness and strain," *Lab Chip*, vol. 13, no. 4, pp. 646–649, Feb. 2013, doi: 10.1039/c2lc41110e.
[24] A. J. Hughes and A. E. Herr, "Microfluidic Western blotting," *Proc Natl Acad Sci U S A*, vol. 109, no. 52, pp. 21450–21455, Dec. 2012, doi: 10.1073/pnas.1207754110.
[25] A. J. Hughes, D. P. Spelke, Z. Xu, C. C. Kang, D. v. Schaffer, and A. E. Herr, "Single-cell western blotting," *Nat Methods*, vol. 11, no. 7, pp. 749–755, 2014, doi: 10.1038/nmeth.2992.
[26] C. C. Kang, K. A. Yamauchi, J. Vlassakis, E. Sinkala, T. A. Duncombe, and A. E. Herr, "Single cell-resolution western blotting," *Nat Protoc*, vol. 11, no. 8, pp. 1508–1530, Aug. 2016, doi: 10.1038/nprot.2016.089.
[27] C. S. Simmons, A. J. S. Ribeiro, and B. L. Pruitt, "Formation of composite polyacrylamide and silicone substrates for independent control of stiffness and strain," *Lab Chip*, vol. 13, no. 4, pp. 646–649, 2013, doi: 10.1039/c2lc41110e.
[28] M. E. Moustafa, V. S. Gadepalli, A. A. Elmak, W. Lee, R. R. Rao, and V. K. Yadavalli, "Large area micropatterning of cells on polydimethylsiloxane surfaces," *J Biol Eng*, vol. 8, no. 1, Oct. 2014, doi: 10.1186/1754-1611-8-24.
[29] M. H. Schneider, Y. Tran, and P. Tabeling, "Benzophenone absorption and diffusion in poly(dimethylsiloxane) and its role in graft photo-polymerization for surface

modification," *Langmuir*, vol. 27, no. 3, pp. 1232–1240, Feb. 2011, doi: 10.1021/LA103345K/ASSET/IMAGES/MEDIUM/LA-2010-03345K_0013.GIF.
[30] I. Sanzari, M. Callisti, A. de Grazia, D. J. Evans, T. Polcar, and T. Prodromakis, "Parylene C topographic micropattern as a template for patterning PDMS and Polyacrylamide hydrogel," *Scientific Reports 2017 7:1*, vol. 7, no. 1, pp. 1–11, Jul. 2017, doi: 10.1038/s41598-017-05434-6.
[31] P. Abdel-Sayed, K. A. Yamauchi, R. E. Gerver, and A. E. Herr, "Fabrication of an Open Microfluidic Device for Immunoblotting," *Anal Chem*, vol. 89, no. 18, pp. 9643–9648, Sep. 2017, doi: 10.1021/acs.analchem.7b02406.
[32] C. T. Lo, D. J. Throckmorton, A. K. Singh, and A. E. Herr, "Photopolymerized diffusion-defined polyacrylamide gradient gels for on-chip protein sizing," *Lab Chip*, vol. 8, no. 8, pp. 1273–1279, Jul. 2008, doi: 10.1039/B804485F.
[33] Y. Zhang, I. Naguro, and A. E. Herr, "In Situ Single-Cell Western Blot on Adherent Cell Culture," *Angewandte Chemie - International Edition*, vol. 58, no. 39, pp. 13929–13934, Sep. 2019, doi: 10.1002/anie.201906920.
[34] T. A. Duncombe *et al.*, "Hydrogel Pore-Size Modulation for Enhanced Single-Cell Western Blotting," *Advanced Materials*, vol. 28, no. 2, pp. 327–334, Jan. 2016, doi: 10.1002/adma.201503939.
[35] A. Gopal and A. E. Herr, "Multiplexed in-gel microfluidic immunoassays: characterizing protein target loss during reprobing of benzophenone-modified hydrogels," *Sci Rep*, vol. 9, no. 1, Dec. 2019, doi: 10.1038/S41598-019-51849-8.
[36] F. Bunge, S. van den Driesche, and M. J. Vellekoop, "Microfluidic Platform for the Long-Term On-Chip Cultivation of Mammalian Cells for Lab-On-A-Chip Applications," *Sensors (Basel)*, vol. 17, no. 7, Jul. 2017, doi: 10.3390/S17071603.
[37] B. Schurink and R. Luttge, "Hydrogel/poly-dimethylsiloxane hybrid bioreactor facilitating 3D cell culturing," *Journal of Vacuum Science & Technology B, Nanotechnology and Microelectronics: Materials, Processing, Measurement, and Phenomena*, vol. 31, no. 6, p. 06F903, Nov. 2013, doi: 10.1116/1.4831762.
[38] R. Booth and H. Kim, "Characterization of a microfluidic in vitro model of the blood-brain barrier (μBBB)," *Lab Chip*, vol. 12, no. 10, pp. 1784–1792, Apr. 2012, doi: 10.1039/C2LC40094D.
[39] D. Keskin, T. Mokabbar, Y. Pei, and P. van Rijn, "The relationship between bulk silicone and benzophenone-initiated hydrogel coating properties," *Polymers (Basel)*, vol. 10, no. 5, pp. 11–13, 2018, doi: 10.3390/polym10050534.
[40] M. E. Moustafa, V. S. Gadepalli, A. A. Elmak, W. Lee, R. R. Rao, and V. K. Yadavalli, "Large area micropatterning of cells on polydimethylsiloxane surfaces," *J Biol Eng*, vol. 8, no. 1, pp. 1–10, 2014, doi: 10.1186/1754-1611-8-24.
[41] A. Gokaltun, M. L. Yarmush, A. Asatekin, and O. B. Usta, "Recent advances in nonbiofouling PDMS surface modification strategies applicable to microfluidic technology," *Technology (Singap World Sci)*, vol. 05, no. 01, pp. 1–12, 2017, doi: 10.1142/s2339547817300013.
[42] O. Chaudhuri *et al.*, "Substrate stress relaxation regulates cell spreading," *Nat Commun*, vol. 6, 2015, doi: 10.1038/ncomms7365.
[43] A. K. Yip *et al.*, "Cellular response to substrate rigidity is governed by either stress or strain," *Biophys J*, vol. 104, no. 1, pp. 19–29, Jan. 2013, doi: 10.1016/j.bpj.2012.11.3805.

[44] A. J. S. Ribeiro, A. K. Denisin, R. E. Wilson, and B. L. Pruitt, “For whom the cells pull: hydrogel and micropost devices for measuring traction forces,” *Methods*, pp. 1–40, 2019.
[45] Z. Jahed, H. Shams, M. Mehrbod, and M. R. K. Mofrad, *Mechanotransduction pathways linking the extracellular matrix to the nucleus*, 1st ed., vol. 310. Elsevier Inc., 2014. doi: 10.1016/B978-0-12-800180-6.00005-0.
[46] C. T. Herman, G. K. Potts, M. C. Michael, N. V. Tolan, and R. C. Bailey, “Probing dynamic cell-substrate interactions using photochemically generated surface-immobilized gradients: Application to selectin-mediated leukocyte rolling,” *Integrative Biology*, vol. 3, no. 7, pp. 779–791, 2011, doi: 10.1039/c0ib00151a.
[47] D. N. Adams, E. Y. C. Kao, C. L. Hypolite, M. D. Distefano, W. S. Hu, and P. C. Letourneau, “Growth cones turn and migrate up an immobilized gradient of the laminin IKVAV peptide,” *J Neurobiol*, vol. 62, no. 1, pp. 134–147, 2005, doi: 10.1002/neu.20075.
[48] E. K. U. Larsen, M. B. L. Mikkelsen, and N. B. Larsen, “Protein and cell patterning in closed polymer channels by photoimmobilizing proteins on photografted poly(ethylene glycol) diacrylate,” *Biomicrofluidics*, vol. 8, no. 6, 2014, doi: 10.1063/1.4905093.
[49] H. Nakamura *et al.*, “The Life of Pi Star: Exploring the Exciting and Forbidden Worlds of the Benzophenone Photophore,” *Chem Rev*, vol. 116, no. 24, pp. 15284–15398, 2016, doi: 10.1021/acs.chemrev.6b00342.
[50] M. Sangermano and N. Razza, “Light induced grafting-from strategies as powerful tool for surface modification,” *Express Polym Lett*, vol. 13, no. 2, pp. 135–145, 2019, doi: 10.3144/expresspolymlett.2019.13.
[51] C. L. Hawkins and M. J. Davies, “Generation and propagation of radical reactions on proteins,” *Biochim Biophys Acta Bioenerg*, vol. 1504, no. 2–3, pp. 196–219, 2001, doi: 10.1016/S0005-2728(00)00252-8.
[52] C. Papuc, G. V. Goran, C. N. Predescu, and V. Nicorescu, “Mechanisms of Oxidative Processes in Meat and Toxicity Induced by Postprandial Degradation Products: A Review,” *Compr Rev Food Sci Food Saf*, 2017, doi: 10.1111/1541-4337.12241.
[53] C. López-Alarcón, A. Arenas, E. Lissi, and E. Silva, “The role of protein-derived free radicals as intermediaries of oxidative processes,” *Biomolecular Concepts*. 2014. doi: 10.1515/bmc-2014-0004.

Chapter 6: Conclusions and future directions

Advancements in electrophoretic cytometry methods advance our understanding of important biological processes. Many of these processes are coordinated by or stem from an aberrant cell subpopulation, such as drug resistance and cancer metastasis [1]–[4]. Here, we present novel platforms for the time-sensitive measurement of cytoskeletal reorganization and mechano-sensitive response from single cells. We combine the specificity of immunoassays with electrophoretic separations and increase the assay specificity by reporting on multiple characteristics of the cellular or proteomic profile of single cells.

We developed a first-in-kind method for the quantification of cytoskeletal protein complexes, with the molecular specificity and resolution to diminish monomeric and complexed protein subpopulations from single cells. We combined differential fractionation lysis within a polyacrylamide gel for size-based fractionation of three major cytoskeletal species. Size-exclusion principles enhance the specificity of the assay beyond what is possible with immunoreagents alone: Antibody-based detection reports on analyte species by specific binding, and spatial separation of proteins based on size reports on the quaternary structure of that specific species at the time of analysis. Thus, not only the abundance of monomeric protein is reported, but also the fraction participating in filamentous structure compared to the globular population. We evaluated the SIFTER platform by investigating the effects of drug treatments that had been previously evaluated in bulk systems. With single-cell resolution, we uncovered intrapopulation heterogeneity previously unreported. Our investigation revealed that perturbations to F-actin, intermediate filaments, or microtubule structure might be compensated for by one or more of the other species.

Looking ahead, the underlying functional principle of SIFTER could be expanded to other protein complexes. Of particular interest are the erbB (HER) family receptors that oligomerize to transmit signals associated with tumorigenesis [5]. Disruption in the dimerization and protein overexpression have been identified in cancerous and drug resistant subpopulations [6]. Thus, the absolute quantification of the erbB family in addition to evaluation of dimerization patterns, including abundance and identification of binding species, could elucidate new phenotypes and drug targets of value. Additionally, there is significant value in detection of protein chaperones and actin-binding proteins. Without additional modification of the SIFTER platform, we anticipate the co-segregation of these species with their conjugated partner due to the native electrophoresis step.

Our investigation of the cytoskeletal protein processes and abundances led to the development of the PDMS-PAG device for on-chip culture of single cells and highly multiplexed detection of cytoskeletal proteins. We established a two-layer assay that couples mechanical ECM stimulus with proteomic profiling *in situ*. Utilizing the PAG as a sieving and immobilization membrane, we achieved a high degree of multiplexing, permitting a more global assessment of cytoskeletal proteins and focal adhesions than existing methods. The expansion of electrophoretic cytometry tools to include on-chip culture by coupling the analytical polyacrylamide matrix with a cell culture extracellular material, permits the analysis of adherent cells without the perturbations of sample preparation techniques [7].

This platform enables the interrogation of mechanobiology questions previously not evaluated, evaluated with only a couple of protein targets, or evaluated with low throughput. We can utilize the interchangeable elements of the PDMS-PAG device for stiffness measurements by evaluating the effect of other mechanical and chemical cues (and combinations thereof) on the downstream effect on cellular state. The PDMS layer can be exchanged for alternative materials, permitting the testing of a larger range of stiffnesses and ECM protein cues [8], [9]. Furthermore, the patterned micro island that defines the cell culture areas on the device can be altered to different shapes and sizes [10]. Furthermore, due to the open device configuration, cultured cells can easily be exposed to other stimulants simultaneously. For example, drug and small molecule delivery to the cultured cells is trivial.

Development of new microanalytical tools for biological and biochemical inquiry requires innovative geometries, materials, and assay designs [11]. To achieve single-cell resolution in electrophoretic cytometry tools, analyte concentrations must be kept high, and injection dispersion limited. We identified means of remedying biological variation in these systems stemming from injection dispersion patterns. We also evaluated the feasibility of fused PDMS-PAG devices for more complicated geometries than those included in the on-chip culture work. Our investigation revealed that PAG can be functionalized onto a benzophenone-modified PDMS to generate a robust, bonded device.

In short, the work presented in this dissertation was aimed at developing multidimensional analysis tools to shine light on complex cytoskeletal processes.

References

[1] S. Nagasawa, Y. Kashima, A. Suzuki, and Y. Suzuki, "Single-cell and spatial analyses of cancer cells: toward elucidating the molecular mechanisms of clonal evolution and drug resistance acquisition," *Inflamm Regen*, vol. 41, no. 1, pp. 1–15, Dec. 2021, doi: 10.1186/S41232-021-00170-X/FIGURES/5.

[2] K. Liu, R. Gao, H. Wu, Z. Wang, and G. Han, "Single-cell analysis reveals metastatic cell heterogeneity in clear cell renal cell carcinoma," *J Cell Mol Med*, vol. 25, no. 9, pp. 4260–4274, May 2021, doi: 10.1111/JCMM.16479.

[3] T. Liu *et al.*, "Single cell profiling of primary and paired metastatic lymph node tumors in breast cancer patients," *Nature Communications 2022 13:1*, vol. 13, no. 1, pp. 1–17, Nov. 2022, doi: 10.1038/s41467-022-34581-2.

[4] C. Jackson, D. Browell, H. Gautrey, and A. Tyson-Capper, "Clinical significance of HER-2 splice variants in breast cancer progression and drug resistance," *International Journal of Cell Biology*. 2013. doi: 10.1155/2013/973584.

[5] P. J. Brennan, T. Kumogai, A. Berezov, R. Murali, and M. I. Greene, "HER2/Neu: mechanisms of dimerization/oligomerization," 2000. [Online]. Available: www.nature.com/onc

[6] C. D. Fichter *et al.*, "EGFR, HER2 and HER3 dimerization patterns guide targeted inhibition in two histotypes of esophageal cancer," *Int J Cancer*, vol. 135, no. 7, pp. 1517–1530, Oct. 2014, doi: 10.1002/ijc.28771.

[7] Y. Zhang, I. Naguro, and A. E. Herr, “In Situ Single-Cell Western Blot on Adherent Cell Culture,” *Angewandte Chemie - International Edition*, vol. 58, no. 39, pp. 13929–13934, Sep. 2019, doi: 10.1002/anie.201906920.

[8] A. K. Denisin and B. L. Pruitt, “Tuning the Range of Polyacrylamide Gel Stiffness for Mechanobiology Applications,” *ACS Applied Materials and Interfaces*, vol. 8, no. 34. American Chemical Society, pp. 21893–21902, Aug. 31, 2016. doi: 10.1021/acsami.5b09344.

[9] A. J. Ribeiro, A. K. Denisin, E. Wilson, and B. L. Pruitt, “For whom the cells pull: hydrogel and micropost devices for measuring traction forces,” 2019. [Online]. Available: https://www.elsevier.com/open-access/userlicense/1.0/

[10] M. Versaevel, J. B. Braquenier, M. Riaz, T. Grevesse, J. Lantoine, and S. Gabriele, “Super-resolution microscopy reveals LINC complex recruitment at nuclear indentation sites,” *Sci Rep*, vol. 4, 2014, doi: 10.1038/srep07362.

[11] T. A. Duncombe, A. M. Tentori, and A. E. Herr, “Microfluidics: Reframing biological enquiry,” *Nat Rev Mol Cell Biol*, vol. 16, no. 9, pp. 554–567, 2015.

Appendices

Appendix A: List of symbols and abbreviations

Table A1

Symbol	Definition	Units (if applicable)
σ_c	Buffer conductivity	S m^{-1}
E	Electric field strength	Volts m^{-1}
F_{EP}	Electric force	N
EP	Electrophoresis	
μ_{EP}	Electrophoretic mobility	µm cm V^{-1} s^{-1}
U_{EP}	Electrophoretic velocity	µm s^{-1}
K_D	Equilibrium dissociation constant	M
η	Fluid kinematic viscosity of the separation medium	Pa s
r	Hydrodynamic radius	m
ICC	Immunocytochemistry	
IF	Intermediate filaments	
Jpk	Jasplakinolide	
Q	Joule (resistive) heating	J s^{-1}
LatA	Latrunculin A	
MT	Microtubules	
q	Net charge of the particle	q
k_1	Off binding constant	s^{-1}
k_{-1}	On binding constant	M^{-1} s^{-1}
n_c	Peak capacity	#
PAGE	Polyacarylamide gel electrophoresis	
PAG	Polyacrylamide gel	
PLA	Proximity Ligation assays	
ROI	Region of interest	
K_R	Retardation coefficient	# between 1-0
Rs	Separation resolution	Non-dimensional
SNR	Signal-to-noise ratio	
scWB	Single-cell western blot	
SIFTER	Single-cell protein Interaction Fractionation Through Electrophoresis and immunoassay Readout	
SDS	Sodium Dodecyl Sulfate	
F_{drag}	Stokes drag force	N
K	Thermal conductivity	W m^{-1} K^{-1}
%T	Total acrylamide concentration (gel density, bis and acrylamide)	%W/V
µ	Viscosity	Pa s

Appendix B: Development and implementation of PID controller for open microfluidic systems

Introduction

Temperature control is required for many chemical and biological assays. Controlled heat delivery to a system can optimize and improve performance. Prior to this work, heating of the single-cell western blot (and similar) platforms was done by heating the lysis buffers. In the microscale filament assay (SIFTER), lid gels were heated to 75 °C to account for rapid heat loss during handling [1]. The hot gel lid was applied to the separation gel once cooled slightly, presumably at 37 °C.

For better engineering controls, a PID controller can provide the constant and controlled temperature that is necessary for optimized and consistent heat delivery across runs. We hypothesized that by improving the heat delivery system for assays like SIFTER, we can decrease run-to-run variation. Proper heating to the optimal operating temperature can ensure that cells are lysed properly while maintaining the protein filaments of interest.

The PID controller offers a closed-loop control (CLC) system. In a CLC, the difference between the actual output and the desired output is used by the controller to meet the desired system output. The signal error (difference between set value and system value) is amplified and fed into the controller. Here, we used a standard PID controller. To briefly summarize the theory of a PID controller: A PID controller has proportional, integral, and derivative terms that can be represented in the transfer function form as:

$$K(s) = K_p + \frac{K_i}{s} + K_d s$$

where K_p is the proportional gain, K_i is the integral gain, and K_d is the derivative gain. By tuning the PID controller gains, the system can provide control action designed for specific process requirements. In general, the proportional term drives a change to the output that is proportional to the current error. The integral term is proportional to both the magnitude of the error and the duration of the error. It (when added to the proportional term) accelerates the movement of the process towards the set point and often eliminates the residual stead-state error that might occur with a proportional only controller. Lastly, the derivative gain is the “anticipatory control” as it tries to reduce the error by controlling the rate of error change based on the best estimate of the future trend of the error.

For finding the correct PID values, multiple methods can be used. Manual tuning can be done with online systems, but constants derived from online models might not transfer to the system in question. Many newer PID controllers, such as the one used here, have an auto-tune PID setting. In this case, the system will oscillate around the set temperature a few times while adjusting the P, I and D values. The general effects of increasing a parameter during optimizaition are summarized in **Table B1**. Alternative to these approaches, the Cohen-Coon and Ziegler-Nichols methods are proven methods for PID term optimization [2]–[4].

Table B1: Effects of *INCREASING* a parameter independently in PID term optimization

Parameter	Rise time	Overshoot	Settling time	Steady-state error	Stability
K_p	Decrease	Increase	Small change	Decrease	Degrade
K_i	Decrease	Increase	Increase	Eliminate	Degrade
K_d	Minor change	Decrease	Decrease	No effect (in theory)	Improve if Kd is small

Next, we describe the setup and required material to build a PID heater for open microfluidics.

Required material:

- Inkbird ITC-106VH
- 40A Solid State Relay (SSR)
- Mounting bracket
- K-type thermocouple (0.13mm tiamter)
- 1x PZRT K-type thermocouple plug adapter mini (female)
- power cord (with positive, negative, and ground - *I reused one from an old laptop*)
- PCT Heating element
- Aluminum block (sized appropriately to the area for heating)
    - Note: The aluminum block adds thermal mass such that temperature swings are less apparent.
- Acrylic sheets (~1.5 ft^2)
- High temperature epoxy
- 16-gauge wire (a few feet of black and red)
- Liquid crystal temp stickers (in the temperature range of interest)
- GFCI plug adapter

Setup:

The Inkbird PID controller, SSR, heater, thermocouple and power line was connected according to the following wiring diagram (**Figure B1**). Note that the thermocouple plug adapter was used to connect the thermocouple to the PID.

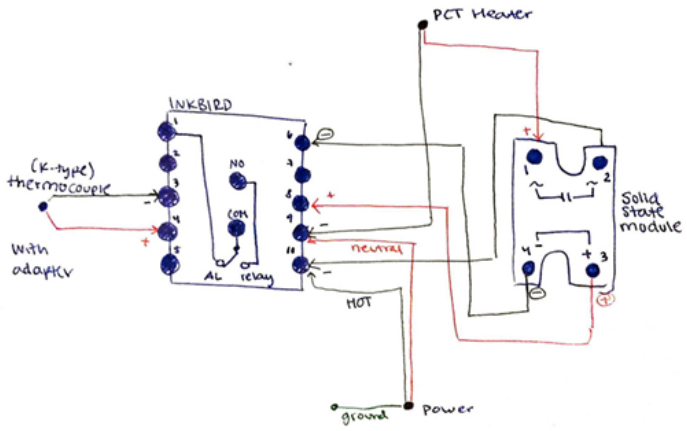

Figure B1: Basic wiring diagram for the Inkbird PID controller.

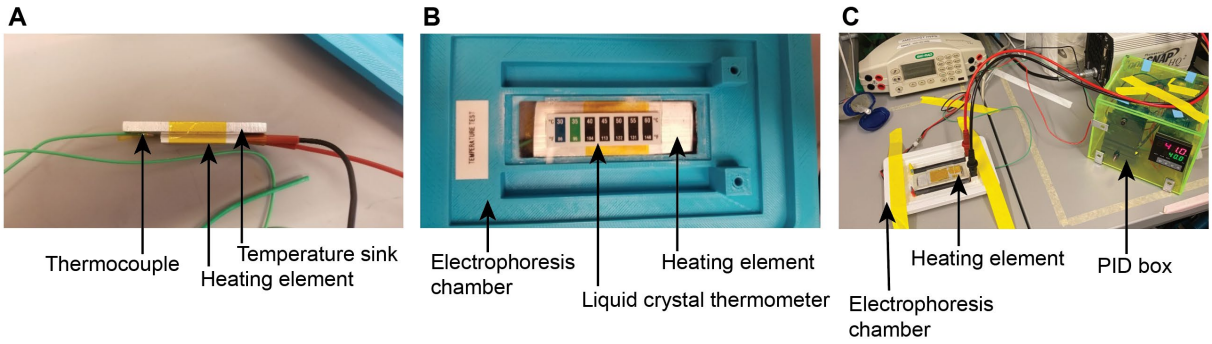

Figure B2: Images capturing the physical setup of the PID heater and the interface with the scWB electrophoresis chamber. (A) Side view of the small heating element. The heating element is secured to a larger aluminum heat sink to ensure uniform heating of the area of interest. For the scWB, a 1 x 1.5-inch region must be heated consistently. The aluminum was trimmed to fit the desired region and to fit securely inside the electrophoresis chamber **(B)** Top view of the electrophoresis chamber and heater interface. The heater sits below the open microfluidic platform and heats from the bottom. This ensures that the electrophoresis system is still accessible from the top, as necessary for proper assay handling. Liquid crystal thermometer was mounted to a glass slide to mimic the location of the polyacrylamide gel, and reports on the temperature at the place of interest for proper optimization of PID setpoint. **(C)** Overview image of SIFTER assay setup with the PID heater implemented. The PID heater is encased in a green/yellow acrylic case for safety and easy handling.

The heating element secured to the aluminum heat sink with Kapton tape (**Figure B2A**). The aluminum adds thermal mass to the system, which helps combat rapid increases and decreases in temperature. Added mass will retain the heat even when the power to the heater is off. The aluminum was cut to fit on the underside of the SIFTER scWB system with a circular saw.

To evaluate the heat transfer efficiency, we used reversible temperature labels made with temperature sensitive liquid crystals secured to a glass slide (**Figure B2B**). The heat flux must pass through the heater, aluminum block and two glass slides to heat the gel (area of interest). By placing the sticker on top of a second slide, we can mimic the location of the gel. We found that

we need to increase the temperature slightly (PID setpoint at ~45 °C) to achieve a surface temperature of 37 °C, as confirmed by the temperature sticker.

PID value optimization:

After trying the autotuning protocol on the PID controller with little success, I manually optimized the variables. While tedious, this method is the most robust for providing P, I and D terms that are optimized to your system [5]. The optimization of variables was done the following way:

1. Set I and D both to zero
2. Adjust P until it holds somewhat near setpoint
3. cut that P in half and begin increasing I to eliminate any persistent error
4. keep derivative at zero or 1

In this case, we did not need derivative action. Since overshot would be detrimental to the biological materials to be used with this heater, we accepted a slower ramp up rate as a tradeoff to eliminate overshot.

The finalized parameters (as of 7/23/2019):

Control period: 1 second
P: 4
I: 1 second
D: 0 second

We created an acrylic chamber for the controller so we could minimize hazards (**Figure B2C**). An acrylic box was cut with laser cutter and assembled with epoxy. The box has cutouts for the control panel, outgoing wires (heater, thermocouple, power), and slots for securing the SSR to the side. It included cutouts for ventilation as well to ensure that the SSR does not overheat.

Appendix C: Production of imaging chamber for liquid-submerged electrophoresis

To analyze lysis and electrophoresis of fluorescent cells and proteins in the open single-cell western blot system, a new electrophoresis (EP) chamber compatible with the microscope must be developed. Existing platforms either lack the transparent bottom for use with the inverted fluorescence microscope, was made for fluid-less systems (such as the IEF, SIFTER, and DDF systems), or have electrode holes that permit liquid to escape, making them incompatible with the microscope. Similarly, many of the in-house printed EP chambers are not watertight. Buffer leakage puts microscope objectives at risk in an inverted setup.

Here, I modified a 100mm petri dish for live monitoring of lysis and EP of fluorescent cells and proteins. By using the 100mm petri dish, it is easily compatible with the microscopes by the standard stage adapter (**Figure C1**). The petri dish has a clear bottom that is easily imaged through without interfering with fluorescence signal from modified proteins (**Figure C2**). To make the dish function for electrophoresis, a few modifications were made:

a. Acrylic, semicircle fillers were cut from 2.5mm acrylic on the laser cutter and stacked 4 high to create a 10 mm tall filler. By introducing the fillers, the inner volume of the dish is reduced, and the 'active' space made rectangular, like existing EP chambers.
b. Platinum wires were placed 3 cm apart. To avoid cutting or drilling into the dish, the wires were run up the side of the dish. At 40 V/cm, this device requires 120V to keep the E-field consistent with existing chambers. One platinum wire was acquired from Spectrum, and another was 'borrowed' from a damaged EP chamber in lab.
c. The inner volume (once acrylic fillers have been added) is max 15 mL.

When in use with 15 mL of 2X RIPA buffer at a set voltage of 120V, a basic power supply stalls out at ~85-90V. I hypothesize it to be the result of the additional buffer (15 mL compared to 12 mL), yielding a higher cross-sectional area of the conductive fluid perpendicular to the E-field direction. Additionally, a higher degree of electrolysis of water is apparent (**Figure C1, Right)**. To get comparable function to the standard setups, the liquid cross-section was reduced. Approximately 8-10 mL of bifunctional lysis and electrophoresis buffer generates a cross sectional area that matches, and successfully sustains the 120V for the duration of the experiment.

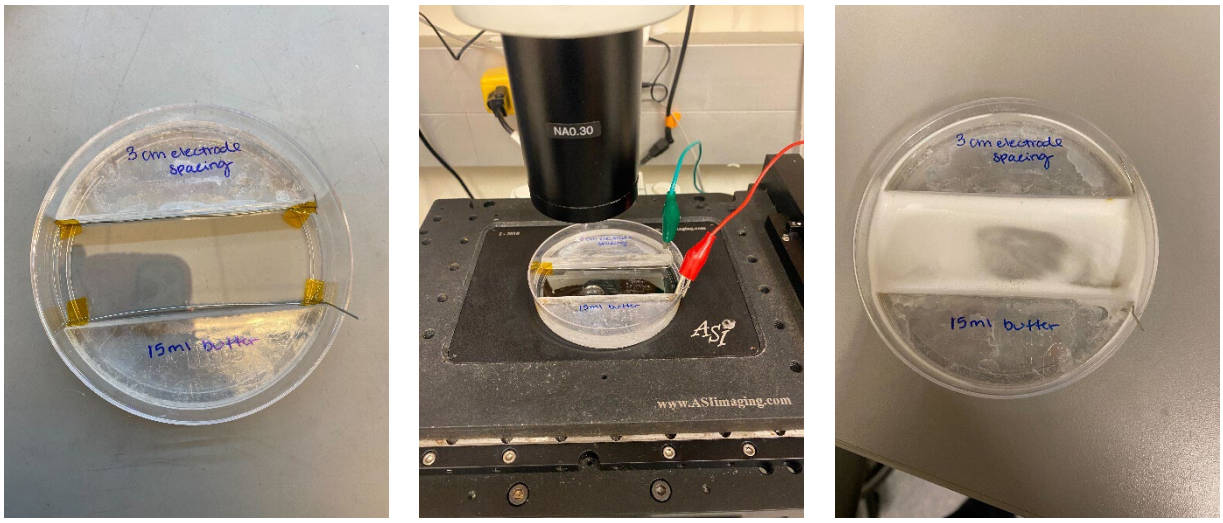

Figure C1: **EP chamber made from 100mm petri dish**. (Left) 10mm tall acrylic half-moons cut the decrease the inner volume of the dish and create the sidewalls for electrode placement. Electrodes are 3 cm apart. (middle) the dish fits into the I-3010 ASI stage adapter (accepts a single slide, small dishes, and the larger 100mm dish) and can be hooked up to the power supply via alligator chips, like the conventional scWB chamber. (right) high degree of hydrolysis apparent by the bubbles.

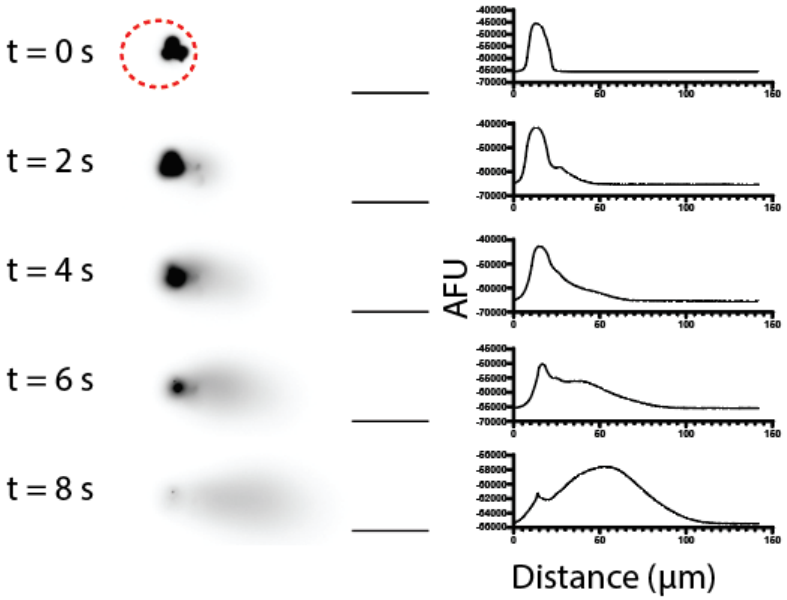

Figure C2: Example lysis and electrophoretic data collected using petri dish EP chamber. (Left) Inverted fluorescence micrograph timelapse of three MCF-7 GFP cells settled into a microwell (red dotted line, 50 µm diameter) and (right) corresponding intensity profile. During lysis, the cell membrane is disrupted, and cell material escapes the cellular compartments into the microwell. Upon electrophoresis (t = 2s,V = 40 v/cm = 120 V) fluorescent material is injected into the gel (8 %T, 3.3 %C). Images acquired with 600 ms exposure on fluorescent microscope with the appropriate filters for GFP detection. Scale bar = 50 µm.

Appendix D: Adhesive tape spheroid

During my time as a Ph.D. student, I have collected most non-hazardous lab tape used in the lab. The resultant spheroid has the following specs (**Figure D1**):

- Mass: 578.2 g
- Circumference: 46.5 cm
- Mass of one roll of 2 cm wide tape (minus cardboard core) = 34.9 g -3.5 g = 31.4 g
- Approximate number of tape rolls used (assuming only 2 cm wide tape of was used): 18.4 rolls of tape
- Approximate distance of tape: 2804.16 m = 2.8 km

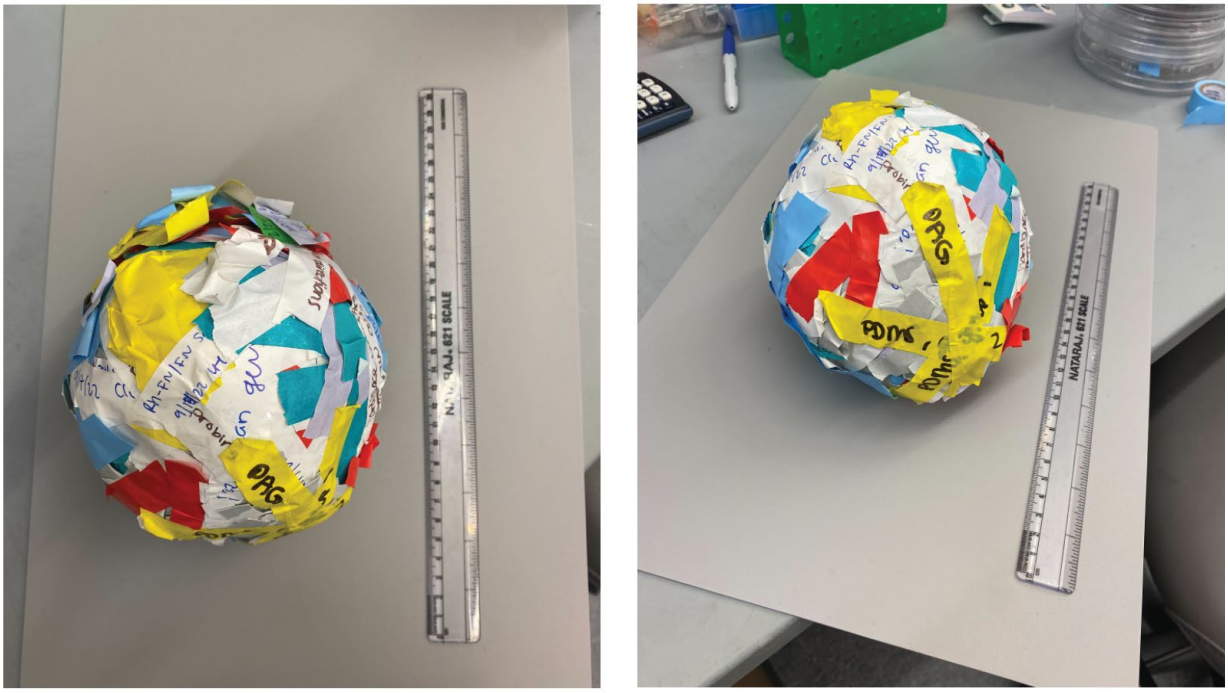

Figure D1: Adhesive tape spheroid composed of non-hazardous lab tape with 12-inch ruler for scale.

Appendix E: Native slab gel protocol for blue native electrophoresis of protein complexes

Introduction*:*

Blue native polyacrylamide gel electrophoresis (BN-PAGE) is a method for the isolation of intact protein complexes. Although it was initially used to study mitochondrial respiratory chain enzymes, it can be applied to other protein complex [6]. The use of BN-PAGE has increased exponentially over the past few years, and many new applications have been developed. For example, blue native two-dimensional electrophoresis allows analysis of both the concentration and the composition of mitochondrial protein complexes [7], [8]. In the first dimension, separation of the complexes under native condition occurs according to their molecular mass, and in the second dimension, where electrophoresis is performed under denaturing condition, the individual subunits of the complexes are resolved, again based on their molecular mass. However, BN-PAGE also has its limitations, notably it is mostly used for membrane proteins [9]–[11]. There are variations of it, such as CLEAR-PAGE, that might combat this limitation for certain applications.

In BN-PAGE, proteins are resolved by molecular weight while retaining their native structure and any potential protein complexes. Instead of the conventional use of SDS in SDS-PAGE, Coomassie Blue-G250 dye is used to coat proteins with the negative charge necessary for migration to the anode. By eliminating strong ionic detergents, protein complexes are maintained and migrate through the gel until they have reached their specific pore size limit. For BN-PAGE, special attention must be paid to the type of lysate and detergent used to maintain specific

complexes or protein-protein interactions. Common detergents used in BN-PAGE include digitonin, dodecylmaltoside, and Triton X-100.

Here, we summarize the developed protocol for use of BN-PAGE for separation of protein complexes. Specifically, this method was used for the separation of antibody-nanobody complexes, where the input sample is purified antibody and fluorescent nanobodies, and membrane-bound protein-protein complexes, where the input is whole cell lysate complexes. The protocol was based on refs: [12] and the Native PAGE Novex Bis-Tris Gel System User Guide from Life Technologies.

Materials:

- Experimental conditions: Material to be separated prepared in native conditions
    - For cellular material, generate lysate in Novex Sample Buffer + 1-2% Digitonin
        - Phosphatase and Protease inhibitor (product #: 89900)
    - For antibody-nanobody complexes, let the purified material conjugate for 2 hours prior to analysis
- Ladder
    - NativeMark Unstained Protein standard (~20-1200 kDa)
- NativePAGE Sample Buffer (4X)
- Native PAGE Noves 4-16% Bis-Tris gel (10-well format)
    - 4-16% Bis-Tris gels can resolve proteins in the molecular weight range of 15-1,000 kDa
    - The 10 well gel has a recommended maximum load volume of 25 uL.
- Running buffers:
    - Anode buffer (outer buffer chamber, ~600 mL): Novex Tris-Glycine Native Running buffer (10X) (ThermoFisher Scientific, LC2672) or NativePAGE Running Buffer (ThermoFisher Scientific, BN2001)
    - Cathode buffer (inner buffer chamber, ~200mL): NativePAGE Cathode Buffer Additive (20X) (VDF m)
- PDVF membrane (Invitrolon DVDF Filter Sandwich, LC2005)
    - Note: Nitrocellulose is not compatible with BN-PAGE as nitrocellulose membrane binds the Coomassie dye.
- 4 sheets of filter paper
- 1-step transfer buffer (ThermoScientific, 84731)
- Native PAGE 5% G-250 sample addition
    - Only use for sample preparation if using nonionic detergents in sample preparation methods for protein extraction
- 5% BSA in TBST solution
- Primary antibody solution (if using): 9 mL TBST, 1 mL 5% BSA in TBST, 10 µL primary antibody
- Secondary antibody solution (if using): 9 mL TBST, 1 mL 5% BSA in TBST, 1 µL primary antibody

- Note: secondary antibody should be conjugated appropriately for the detection method of choice

- Western lightning solution, Chemiluminescent substrate (Perkin Elmer, NEL105001EA)
- pH meter, weighing balance, and other standard lab equipment
- Vertical acrylamide electrophoresis unit. The XCell SureLock Mini-Cell is recommended.
- Semi-dry electroblotting system

Procedure:

- Prepare experimental samples, buffers, and gels
  1. Prepare the sample:
     a. To create 20 µL of sample
        i. 5 uL NativePAGE Sample Buffer (4X)
        ii. Sample of interest
        iii. Add deionized water to 20 uL volume
  2. Prepare the following buffers according to the manufacturer:
     a. For all samples: 1X NativePAGE Anode Buffer
        i. Add 50 mL of 20X NativePAGE Running Buffer to 950 mL of dionized water
     b. For detergent samples: 1X NativePAGE Dark Blue Cathode Buffer (contains 0.02% G-250)
        i. Add 30 mL 20X NativePage Running Buffer and 30 mL 20X Native Page Cathode Additive to 540 mL dionized water
     c. For non-detergent samples: 1X NativePAGE Light Blue Cathode Buffer (contains 0.002% G-250)
        i. Add 30 mL 20X NativePage Running Buffer and 3 mL 20X Native Page Cathode Additive to 567 mL dionized water
- Load samples and buffers
  1. Prepare the gels:
     a. Cut open the gel cassette pouch and drain away the gel pacing buffer
     b. Remove the gel from the pouch
     c. Rinse the gel cassette with dionized water
     d. Peel off the tape from the bottom cassette
     e. Gentle pull the comb out of the cassette
     f. Rinse the gel well three times with 1X NativePAGE Blue Cathode Buffer. Invert the gel and shake to remove the buffer. Repeat two more times.
     g. Place the gels in the running talk. The lower (comb) side faces inwards. If only running one gel, replace the second gel cassette with the plastic buffer dam
     h. Fill the gel wells with 1X NativePAGE Dark Blue Cathode Buffer
  2. To promote a uniform running of the stacking front, load sample buffer in all empty wells

3. Load samples into the sample wells filled with 1X NativePAGE Dark Blue Cathode Buffer prior to filing the cathode chamber to better visualize the sample wells
4. Fill the upper cathode buffer chamber with 200 mL of 1X NativePAGE Cathode Buffer
5. Fill the lower anode buffer chamber with 600 NativePAGE Anode buffer

- Perform electrophoresis
    - Orient the gels in the mini-cell such that the notched well side of the cassette faces inwards towards the buffer core. Secure the gels with the Gel Tension Wedge.
    - Load samples onto the gel (20 µL for 10-well gel)
        - Note: samples are loaded before filling the upper buffer camber to provide easy visualization of the sample wells
    - Load 10 µL of protein standard for 10-well gel
    - Fill the upper buffer chamber with a small amount of running buffer to check for tightness of seal
    - Once the seal is tight, fille the upper buffer chamber (inner) with 200 mL of the appropriate cathode buffer. The buffer level must exceed the level of the wells
    - Fill the lower (outer) buffer chamber with 600 mL of the anode buffer page
    - Place the lid on the assembled mini-cell
    - With the power off, connect the electrode cords to the power supply. Turn on the power
    - Running conditions:
        - Perform electrophoresis at room temperature with pre-chilled buffers
        - 150V
        - 105-120 minutes for 4-16% Bis-Tris Gels at 150 V (constant voltage)
        - Expected current (per gel):
            - Start: 12-16 mA
            - End: 2-4 mA
    - Removing the gel after electrophoresis
        - Separate each of the 3 bonded sides of the cassette with the Gel Knife
        - Remove and discard of the top plate, allowing the gel to remain on the bottom (slotted) plate
        - Hold the plate such that the gel is facing downwards over a container with transfer buffer and push the gel foot through the slot with the Gel Knife to allow the gel to peel from the plate and into the container
        - Remove the gel foot and sample wells with gel knife
- Transfer
    - Use PVDF membrane and 4 pieces of filter paper (2 pieces around the PVDF in package, and 2 extra)
    - Place 4 pc filter paper in lid of square container to equilibrate in transfer buffer (>5 min)

    - Place membrane in bottom of square container and cover in cold MeOH for 1 min. Pour methanol back in storage container and add transfer buffer to the membrane. Incubate >5 min
        - Note: Use tweezers to handle the membrane
    - Pry open gel holder and cut off comb region and the thicker gel region at the bottom. Rinse gel in transfer buffer
    - Place 2 pc wetted filter paper on bottom electrode
    - Place membrane over filter paper (place down slowly from one corner to avoid introducing bubbles)
    - Place gel directly on membrane.
    - Add more buffers, ensuring no bubbles.
    - Add 2 pc filter paper on top and use roller to ensure no bubbles
    - Start transfer
    - Prepare small plastic box for membrane
- Western Blotting
    - Block gel in 5% BSA solution for 30 minutes (2 g BSA in 40 mL TBST)
    1. Primary antibodies: prepare 10 mL of solution
        a. Leave in 4C overnight
    2. Wash: Remove membrane from 4C and rinse trice in TBST for 10 minutes (30 minutes total, switching buffer every 10 minutes)
    3. Secondary antibody
        a. Incubate on shaker at room temperature for 1 hour.
    4. Wash: Remove membrane from 4C and rinse trice in TBST for 10 minutes (30 minutes total, switching buffer every 10 minutes)
- Imaging
    1. Prepare detection reagents: For chemiluminescent detection with HRP antibodies, use the Western lightning solution
        a. Mix 2 components of western lightning 1:1 (for standard membrane, prepare 8 mL)
        b. Incubate membrane in western lightning solution for 90 seconds
        c. If signal degrades too much, membrane can be placed back into detection reagent and imaged again
        d. Detection reagents can be disposed of down the drain once imaging is complete.
    2. Follow standard instructions for imaging with either ChemiDoc or iBright equipment

Appendix F: Relevant GitHub repositories

The code used for analysis of SIFTER material (Chapter 2) can be accessed here: https://github.com/herrlabucb/SIFTER

The code used for analysis of on-chip culture material (Chapter 3) can be accessed here: https://github.com/herrlabucb/OCC-Project

Appendix G: Atomic force spectroscopy for substrate stiffness measurements

Atomic force microscopy (AFM) utilizes a surface probe method for local elasticity measurements. This type of mechanical measurement can be applied to cells, cell culture substrates, and tissues. The viscoelastic resistance of a substrate has been shown to affect a cell's in vitro response [13], including differentiation [14], [15] and development [16]. Changes in the biomechanics (especially stiffness or elasticity) of a cell has been linked to gain-of-function cancer transition [17]–[19].

Here, we report on the protocol developed to extract force curves from indentation measurements of flat PDMS-coated substrates and the associated mathematical theory. While AFM can be used to characterize surface morphology and topography by raster scanning of the material, we focus on the spectroscopy application of the technology in indentation mode [20].

Theory of the analysis of force curves

At its most simple implementation, AFM involves the laser tracking of the deflection of a cantilever probe as the top scans, indents, or otherwise interacts with the sample [21]. With AFM imaging, the material is scanned in the XY-direction. In force spectroscopy, the cantilever probe approaches the sample in the Z-direction. In both modes, the laser beam is deflected off the end of the cantilever and onto a four-quadrant photodetector to monitor vertical and lateral deflection due to material-cantilever contact forces [22].

Obtaining a force-distance curve is necessary to calculate the Young's modulus of the thin film material. Here, the physical and geometric properties of the cantilever determine its spring constant (k). The spring constant is used to convert the measured cantilever deflection (h) into a contact force using Hooke's law for linear elastic materials ($F = k * h$) [23]. For indentation-based experiments, the cantilever completes an extension-retraction cycle. The cantilever is brought into contact with the sample, and further extension is converted into a combination of probe deflection and sample indentation.

The force curve that is generated (z-position and deflection of the probe) contains indentation curve and retraction curve that can be used to extract mechanical properties of the material indented. The difference between the indentation and retraction curve are the result of viscoelastic hysteresis of the sample and can be used to derive the 'stickiness' of the material [23]. The Hertz model can be used to calculate the elastic modulus using the indentation curve for simple systems. The Hertz model states that the Young's modulus of a material is inversely proportional to the square of indentation depth at a given force.

The Hertz model assumes [24], [25]:

1. Homogeneous, isotropic, and linear elastic material
2. Contact between two elastic bodies
3. Axisymmetric and infinitesimal deformation
4. Infinite sample thickness and dimension of a smooth sample surface
5. infinitesimal sample deformation

The thin PDMS films tested in this dissertation satisfy key assumptions of the theory, and the simplified system was used for this analysis. More complex modeling is often necessary for analysis of cells and other complex materials.

From the indentation profile, the Young's modulus can be calculated [19], [23], [26], [27]:

First, the contact point must be identified. Many automatic methods exist for identifying the Z position of the probe when it first contacts the material (d_0). For a manual method, one can use the Domke and Radmacher method where the point is identified based on a two-point fit and extrapolation back to where the deflection is zero [28].

Next, the equation relating force and depth of indentation with a pyramidal tip:

$$F = \frac{3}{4}\frac{E * \tan(\alpha) D^2}{(1-\nu^2)} \quad \text{Eq. 1}$$

Here, α is the half-angle of the tip, and ν is the Poisson's ratio that determines the amount of lateral expansion that accompanies axial compression, E is the Young's modulus to be determined. D is the indentation dept calculated by subtracting the z-position of the probe and the vertical deflection. The poison's ratio is between 0.4 and 0.5 [29]. A Young's modulus can be calculated for each point in the indentation curve, where E will tend toward a constant value that Is dependent ton the chosen contact point [30].

The force of indentation is calculated by Hooke's law and the difference between the measured deflection and the point of contact:

$$F = K(d - d_0) \quad \text{Eq. 2}$$

Protocol for AFS on Nanosurf CoreAFM

This protocol is adapted, in part, from [31] *and describes the use of Nanosurf CoreAFM equipment for force spectroscopy operating mode.*

1. Preparing the sample: AFM samples should be small and thin. The standard CoreAFM sample holder can hold wafers, samples mounted to secure substrate, or glass slides. Samples must be fixed to the sample holder in such a way that they are not able to drift or move in the nanometer range. For the work included in this dissertation, samples were cast on standard glass slide.
    a. Secure the sample slide on the sample holder and secure it with the two sample holder clamps.
    b. The sample holder is placed on the sample platform in the CoreAFM measurement compartment, if not already installed.
2. Mounting the Cantilever in the cantilever holder: Cantilevers must be selected for each operating mode, sample type, and measurement application. Static force mode measurements often call for softer and longer cantilevers compared to dynamic force mode

a. In the operation software, in the Preparation group of the *Acquisition tab*, select the desired cantilever type from the *Cantilever selector* drop-down menu by clicking the currently selected cantilever. If the cantilever type you are using is not available in the list, select the option to create a new cantilever type in the software
    i. The spring constant is calculated based on the cantilever type using the Sader method [32].
b. Place the cantilever holder on top of the cantilever exchange tool and gently release the CantiClip. Take the new cantilever out if its box with the cantilever tweezers and place it on the alignment chip. The AFM cantilever is inserted into the removable AFM cantilever holder
    i. Use the appropriate AFM cantilever holder. For young's modulus measurements of PDMS, the 'Cantilever Holder Liquid/Air' was used.
c. Verify that the cantilever does not move with respect to the alignment chip by carefully tapping on it with the tweezers. If it moves, it is not inserted correctly.
d. Secure the CantiClip by snapping it into its closed position.
e. Attach the cantilever holder with the newly installed cantilever to the Nanosurf CoreAFM scan head. The cantilever is secured to the machine with magnetic snaps.

3. Laser alignment: Whenever a user changes between different cantilever holder types, changes between different copies of the same cantilever holder, or replaces the cantilever with a significantly different one, the laser beam used to measure cantilever deflection must be realigned with the tip of the cantilever.
    a. Check the laser position and quality
        i. In the CoreAFM control software, open the *Laser Alignment dialog* and switch the CoreAFM to the top view camera using the *Camera selector*
        ii. Open the scan head lid to an angle of ~30°
    b. Locate the base edge of the cantilever
        i. If there is a clear spot on your workbench, turn laser alignment screw 1 clockwise until the laser spot disappears.
        ii. Stop and turn the same screw in the other direction (counterclockwise) so that the laser spot just appears again. The laser is now near one of the edges of the cantilever chip.
    c. Center the laser on the cantilever
        i. Turn laser alignment screw 2 in both directions for some time until the laser spot appears to be blocked in the middle
        ii. When the laser is aligned at the spot where it should quickly turn to a bring spot on either side, the laser is on the cantilever base.
    d. Position the laser near the tip end
        i. Turn laser alignment screw 1 counterclockwise to find the point where the laser isn't blocked by the cantilever anymore
        ii. Turn the laser alignment screw 1 back in a clockwise direction slightly. The laser spot will be blocked in the middle. The laser is aligned to the end of the cantilever
    e. Center the laser on the detector

i. While adjusting detector alignment screw 3 and 4, observe the position of the laser on the detector in the *Laser Alignment dialog.* When the spot is centered, you've completed laser alignment

4. Configure measurement parameters: The steps summarized here were optimized for the stiffness measurement of PDMS. If making similar measurements, we recommend starting with these parameter choices and optimizing from there.
    a. In the CoreAFM control software, locate the *Preparation* section of the *Acquisition tab.* Update the measurement environment, operating mode, and cantilever type
        i. Measurement environment = air
        ii. Operating mode = static force (note, the machine must be in dynamic force mode for sensitivity calibration)
        iii. Cantilever = ACL-A
    b. Confirm laser alignment in the *Laser alignment dialog*
    c. Check the resonance frequency of the cantilever using the *Vibration frequency search dialog* (click on *Frequency Sweep* button)
    d. Parameters: Imaging Wizard
        i. Set the image size, time, points, and
5. Cantilever calibration
    a. Use the *thermal tuning dialog* to determine the spring constant of the cantilever. The software automatically uses the calculated results for spring constant to calculate force.
6. Spectroscopy measurement
    a. Ensure that the software is in the *Spectroscopy* tab (located in the lower left-hand corner). The spectroscopy window contains the commands necessary to control the spectroscopy process and parameters.
    b. Use the *Spectroscopy Wizard* to prepare spectroscopy parameters. Select the following parameters:
        i. Spectroscopy measurement: Force-distance Spectroscopy (in AFM static mode).
            1. In force-distance spectroscopy, the cantilever is moved while the deflection signal is measured.
            2. Force modulation mode is an extension of static force mode
        ii. Measurement subtype: Stop by value force-distance grid
            1. A 'Stop by value Force-distance' spectroscopy measurement will start with the cantilever in the fully retracted Z-position, the tip is moved towards the surface and a deflection measurement signal is made in the "forward modulation phase". Measurement will slop at the defined deflection value. The tip is moved away from the sample while deflection is measured in the "backward modulation phase".
            2. In grid measurements, the tip will automatically proceed to the next point's position and repeat the measurement cycle.
        iii. Force-distance curve parameters:
            1. Distance range: 5 μm

2. Time:2 s
3. Data points; 1024
4. Stop at maximal force: 100 nN

c. Define the measurement grid to graphically define the positions for measurement
d. Approach the sample sing the motorized coarse approach to bring the sample close enough to the tip for automated final approach. While observing the tip-sample distance, click and hold the *Advance* button in the *Approach* group of the *Acquisition* tab until the tip is close to the sample
e. Once the sample is in close position to the tip, the top view image can be used to find a good location for measurement. Turn the *Positioning* screws to move the sample in the X and Y, if necessary.
f. Use the automatic final approach to bring the cantilever into close contact with the substrate. In the *Approach group* of the *Acquisition tab,* click on the *Approach* button. The software will notify users when the approach is done.
g. Initiate measurement by clicking the Start button in the Spectroscopy group of the acquisition ribbon

7. Data analysis
    a. To save the completed measurement, use the *Gallery Panel.* The software automatically saves new measurements using the file name mask
    b. Measurements are saved into the folder specified by the gallery path. To change the gallery path, use the Quick Access Toolbar > Gallery settings. The *history files* path indicates where measurements will be stored automatically

References:

[1] J. Vlassakis *et al.*, "Measuring expression heterogeneity of single-cell cytoskeletal protein complexes," *Nature Communications 2021 12:1*, vol. 12, no. 1, pp. 1–14, Aug. 2021, doi: 10.1038/s41467-021-25212-3.

[2] N. Hambali, A. Masngut, A. A. Ishak, and Z. Janin, "Process controllability for flow control system using Ziegler-Nichols (ZN), Cohen-Coon (CC) and Chien-Hrones-Reswick (CHR) tuning methods," *2014 IEEE International Conference on Smart Instrumentation, Measurement and Applications, ICSIMA 2014*, Feb. 2015, doi: 10.1109/ICSIMA.2014.7047432.

[3] E. Joseph and O. OlaiyaO., "Cohen-Coon PID Tuning Method: A Better Option to Ziegler Nichols-Pid Tuning Method," 2018.

[4] A. A. Azman, M. H. F. Rahiman, N. N. Mohammad, M. H. Marzaki, M. N. Taib, and M. F. Ali, "Modeling and comparative study of PID Ziegler Nichols (ZN) and Cohen-Coon (CC) tuning method for Multi-tube aluminum sulphate water filter (MTAS)," *Proceedings - 2017 IEEE 2nd International Conference on Automatic Control and Intelligent Systems, I2CACIS 2017*, vol. 2017-December, pp. 25–30, Dec. 2017

[5] M. Gogoi, "Proportional-Integral-Derivative (PID) controller design for robust stability of arbitrary order plants with time-delay and additive uncertainty", 2010.

[6] L. G. J. Nijtmans, N. S. Henderson, and I. J. Holt, “Blue Native electrophoresis to study mitochondrial and other protein complexes,” *Methods*, vol. 26, no. 4, pp. 327–334, 2002, doi: 10.1016/S1046-2023(02)00038-5.
[7] B. KURIEN and R. SCOFIELD, “Western blotting,” *Methods*, vol. 38, no. 4, pp. 283–293, 2006, doi: 10.1016/j.ymeth.2005.11.007.
[8] B. T. Kurien and R. H. Scofield, *A brief review of other notable protein detection methods on blots.*, vol. 536. 2009. doi: 10.1007/978-1-59745-542-8_56.
[9] H. Schägger and G. von Jagow, “Blue native electrophoresis for isolation of membrane protein complexes in enzymatically active form,” *Anal Biochem*, vol. 199, no. 2, pp. 223–231, 1991, doi: 10.1016/0003-2697(91)90094-A.
[10] I. Wittig, H. P. Braun, and H. Schägger, “Blue native PAGE,” *Nat Protoc*, vol. 1, no. 1, pp. 418–428, 2006, doi: 10.1038/nprot.2006.62.
[11] H. Schaägger, W. A. Cramer, and G. von Jagow, “Analysis of molecular masses and oligomeric states of protein complexes by blue native electrophoresis and isolation of membrane protein complexes by two-dimensional native electrophoresis,” *Anal Biochem*, vol. 217, no. 2, pp. 220–230, 1994, doi: 10.1006/abio.1994.1112.
[12] I. Wittig, H. P. Braun, and H. Schägger, “Blue native PAGE,” *Nature Protocols 2006 1:1*, vol. 1, no. 1, pp. 418–428, Jun. 2006, doi: 10.1038/nprot.2006.62.
[13] A. J. Engler, L. Richert, J. Y. Wong, C. Picart, and D. E. Discher, “Surface probe measurements of the elasticity of sectioned tissue, thin gels and polyelectrolyte multilayer films: Correlations between substrate stiffness and cell adhesion,” *Surf Sci*, vol. 570, no. 1–2, pp. 142–154, Oct. 2004, doi: 10.1016/J.SUSC.2004.06.179.
[14] A. M. Collinsworth, S. Zhang, W. E. Kraus, and G. A. Truskey, “Apparent elastic modulus and hysteresis of skeletal muscle cells throughout differentiation,” *Am J Physiol Cell Physiol*, vol. 283, no. 4 52-4, 2002, doi: 10.1152/AJPCELL.00502.2001.
[15] C. Rianna and M. Radmacher, “Comparison of viscoelastic properties of cancer and normal thyroid cells on different stiffness substrates,” *European Biophysics Journal*, vol. 46, no. 4, pp. 309–324, May 2017, doi: 10.1007/S00249-016-1168-4/FIGURES/8.
[16] C. F. Deroanne, C. M. Lapiere, and B. v. Nusgens, “In vitro tubulogenesis of endothelial cells by relaxation of the coupling extracellular matrix-cytoskeleton,” *Cardiovasc Res*, vol. 49, no. 3, pp. 647–658, Feb. 2001, doi: 10.1016/S0008-6363(00)00233-9.
[17] S. E. Cross, Y.-S. Jin, J. Tondre, R. Wong, J. Rao, and J. K. Gimzewski, “AFM-based analysis of human metastatic cancer cells,” 2008, doi: 10.1088/0957-4484/19/38/384003.
[18] Z. Zhou *et al.*, “AFM nanoindentation detection of the elastic modulus of tongue squamous carcinoma cells with different metastatic potentials,” *Nanomedicine*, vol. 9, no. 7, pp. 864–874, Oct. 2013, doi: 10.1016/J.NANO.2013.04.001.
[19] Q. S. Li, G. Y. H. Lee, C. N. Ong, and C. T. Lim, “AFM indentation study of breast cancer cells,” *Biochem Biophys Res Commun*, vol. 374, no. 4, pp. 609–613, Oct. 2008, doi: 10.1016/J.BBRC.2008.07.078.
[20] B. Du, O. K. C. Tsui, Q. Zhang, and T. He, “Study of elastic modulus and yield strength of polymer thin films using atomic force microscopy,” *Langmuir*, vol. 17, no. 11, pp. 3286–3291, May 2001
[21] J. Roa, G. Oncins, J. Diaz, F. Sanz, and M. Segarra, “Calculation of Young’s Modulus Value by Means of AFM: Ingenta Connect,” *Recent Pat Nanotechnol*, vol. 5, no. 1, pp. 27–63, Jan. 2011

[22] Y. Seo and W. Jhe, “Atomic force microscopy and spectroscopy,” *Reports on Progress in Physics*, vol. 71, no. 1, p. 016101, Dec. 2007, doi: 10.1088/0034-4885/71/1/016101.
[23] K. D. Costa, “Single-cell elastography: Probing for disease with the atomic force microscope,” *Dis Markers*, vol. 19, no. 2–3, pp. 139–154, Jan. 2004.
[24] M. Heuberger, G. Dietler, and L. Schlapbach, “I Mapping the local Young’s modulus by analysis of the elastic deformations occurring in atomic force microscopy,” 1994.
[25] Hertz, “On the Contact of Elastic Solids,”*Crelle’s Journal, 92, 156-171.*
[26] A. Y. Jee and M. Lee, “Comparative analysis on the nanoindentation of polymers using atomic force microscopy,” *Polym Test*, vol. 29, no. 1, pp. 95–99, Feb. 2010, doi: 10.1016/J.POLYMERTESTING.2009.09.009.
[27] J. L. MacKay and S. Kumar, “Measuring the Elastic Properties of Living Cells with Atomic Force Microscopy Indentation,” *Methods in Molecular Biology*, vol. 931, pp. 313–329, 2012, doi: 10.1007/978-1-62703-056-4_15.
[28] J. Domke and M. Radmacher, “Measuring the Elastic Properties of Thin Polymer Films with the Atomic Force Microscope,” 1997.
[29] S. Dogru, B. Aksoy, H. Bayraktar, and B. E. Alaca, “Poisson’s ratio of PDMS thin films,” *Polym Test*, vol. 69, pp. 375–384, Aug. 2018, doi: 10.1016/J.POLYMERTESTING.2018.05.044.
[30] D. C. Lin, E. K. Dimitriadis, and F. Horkay, “Robust strategies for automated AFM force curve analysis--I. Non-adhesive indentation of soft, inhomogeneous materials,” *J Biomech Eng*, vol. 129, no. 3, pp. 430–440, Jun. 2007, doi: 10.1115/1.2720924.
[31] *Nanosurf CoreAFM: Operating Instructions for CoreAFM Control Software*, vol. Version 3.8. 2017.
[32] J. E. Sader, “Frequency response of cantilever beams immersed in viscous fluids with applications to the atomic force microscope,” *J Appl Phys*, vol. 84, no. 1, p. 64, Jun. 1998, doi: 10.1063/1.368002.